



Virginia Commonwealth University
VCU Scholars Compass

Theses and Dissertations

Graduate School

2012

Hemorrhage Detection and Analysis in Traumatic Pelvic Injuries

Pavani Davuluri
Virginia Commonwealth University

Follow this and additional works at: <https://scholarscompass.vcu.edu/etd>



Part of the [Engineering Commons](#)

© The Author

Downloaded from

<https://scholarscompass.vcu.edu/etd/456>

This Dissertation is brought to you for free and open access by the Graduate School at VCU Scholars Compass. It has been accepted for inclusion in Theses and Dissertations by an authorized administrator of VCU Scholars Compass. For more information, please contact libcompass@vcu.edu.

School of Engineering
Virginia Commonwealth University

This is to certify that the dissertation prepared by Pavani Davuluri entitled HEMORRHAGE DETECTION AND ANALYSIS IN TRAUMATIC PELVIC INJURIES has been approved by her committee as satisfactory completion of the dissertation requirement for the degree of Doctor of Philosophy

Rosalyn H. Hargraves, Ph.D., Committee Chair, Department of Electrical and Computer Engineering

Kayvan Najarian, Ph.D., Department of Computer Science, School of Engineering

Afroditi. V. Filippas, Ph.D., Department of Electrical and Computer Engineering, School of Engineering

Kevin R. Ward, M.D., Emergency Medicine, School of Medicine, University of Michigan, Ann Arbor

Alen Docef, Ph.D., Department of Electrical and Computer Engineering, School of Engineering

Robert H. Klenke, Ph.D., Chair of Electrical and Computer Engineering, School of Engineering

J. Charles Jennett, Ph.D., Dean, School of Engineering

F. Douglas Boudinot, Ph.D., Dean, Graduate School

Date

© Pavani Davuluri 2012

All Rights Reserved

HEMORRHAGE DETECTION AND ANALYSIS IN TRAUMATIC PELVIC INJURIES

A dissertation submitted in partial fulfillment of the requirements for the degree of Doctor of Philosophy at Virginia Commonwealth University.

by

PAVANI DAVULURI

M.S., Virginia Commonwealth University (Richmond, USA), 2008

Director: ROSALYN HOBSON HARGRAVES
ASSOCIATE PROFESSOR, DEPARTMENT OF ELECTRICAL AND COMPUTER
ENGINEERING

Virginia Commonwealth University
Richmond, Virginia
August, 2012

Acknowledgments

This dissertation could not have been completed without the help and guidance of a number of people. First of all, I would like to thank Dr. Rosalyn Hobson Hargraves, my dissertation advisor, for the help, support, encouragement and guidance she provided me during the research. I would like to express my deep gratitude to my co-advisor, Dr. Kayvan Najarian for his guidance and encouragement through my entire research and for his invaluable feedback. I would like to thank my committee members, Dr. Alen Docef, Dr. Afroditi. V. Filippas and Dr. Kevin R. Ward for their insights. I am grateful to Dr. Charles H. Cockrell and Dr. Yang Tang from VCU Dept. of Radiology for providing me with the data for my research and for their excellent guidance on understanding the medical images and suggestions for improving my research work.

I would like to thank all the members of my lab and all my friends. It is a pleasure to have studied together with such a great group of students who made my stay at the School of Engineering one of the most memorable and fruitful events of my life. I would also like to thank Simina Vasilache for clarifying all my doubts during the early stage of my research.

Finally, I would like to thank my spouse, Sudheer Yadlapati, who is always there for me, and all other family members for their support and understanding.

This material is based upon work supported by the National Science Foundation under Grant No. IIS0758410. I would like to thank Carolinas Health System and Virginia Commonwealth University Medical Center for providing data for the project.

Table of Contents

	Page
Acknowledgments	ii
List of Tables.....	ix
List of Figures	x
Abstract	xii
Novelty and Contributions	xv
CHAPTER 1 INTRODUCTION	1
1.1. Introduction	1
1.2. Motivation and Problem Statement	1
1.3. Image Segmentation Techniques.....	5
1.4. Proposed Method.....	8
CHAPTER 2 PREPROCESSING AND INITIAL BONE SEGMENTATION	11
2.1. Introduction.....	11
2.2. Anatomy of the Pelvis.....	12
2.3. Preprocessing	13
2.4. Initial Bone Mask Formation	14
2.5. Edge Detection and Seed Growing	15
2.5.1. Seed Growing.....	17
2.6. Best Template Matching and Object Recognition	17
CHAPTER 3 ARTERY DETECTION	19

3.1. Introduction	19
3.2. Catheter Masking	20
3.3. Final Bone Segmentation and Masking.....	23
3.3.1. Edge Merging.....	23
3.3.2. Bone Segmentation and Masking.....	23
3.4. Artery Detection	24
3.4.1. Template Classification.....	24
3.4.2. Initial Artery Position Detection in the First Image of the Scan.....	25
3.4.3. Aorta, Common Iliac and External Iliac Arteries Detection.....	27
3.4.4. Procedure to Determine Internal Iliac Arteries	28
CHAPTER 4 HEMORRHAGE DETECTION AND SEGMENTATION.....	30
4.1. Introduction.....	30
4.2. Unwanted Objects Filtration	31
4.3. Hemorrhage Detection	32
4.4. Hemorrhage Segmentation.....	33
4.4.1. Hemorrhage Matching through Mutual Information	33
4.4.2. Support Vector Machine (SVM) Based Rule Optimization for Hemorrhage Segmentation.....	35
4.4.2.1. Rule Generation	36
4.4.2.2. SVM Based Rule Optimization.....	39
4.4.3. Region Growing	42
4.5. Evaluation Measure for Segmentation.....	44

4.6. Quantitative Measurement	45
4.6.1. Hemorrhage Location Identification	45
4.6.2. Bleeding Foci	45
4.6.3. Hemorrhage Volume Measurement	46
CHAPTER 5 OUTCOME PREDICTION	47
5.1. Introduction	47
5.2. Dataset.....	48
5.3. Feature Extraction	49
5.4. Multi-stage Feature Selection	49
5.4.1 Fracture Feature Reduction	49
5.4.2 Predominant Feature Selection using Symmetrical Uncertainty based Correlation Filter	51
5.5. Classification for Prediction Outcome	53
CHAPTER 6 Abdominal Organ Segmentation	55
6.1. Introduction	55
6.2. Spleen Segmentation.....	56
6.2.1 Preprocessing	57
6.2.2 Histogram based Image Contrast Enhancement	57
6.2.3 Bright Objects Mask Formation and Edge Detection	58
6.2.4 Seed Growing and Bright Objects Segmentation.....	59
6.2.5. Knowledge based Spleen ROI Detection	60
6.2.6. Spleen Detection	60

6.2.6.1. Spleen Detection in the First Image	60
6.2.6.2. Spleen Detection in the Subsequent Images	62
6.2.7. Spleen Segmentation.....	62
6.3. Evaluation measure for spleen segmentation.....	63
CHAPTER 7 RESULTS AND DISCUSSION – PELVIC TRAUMA.....	65
7.1. Introduction.....	65
7.2. Dataset.....	65
7.3. Preprocessing and Initial Bone Segmentation Results.....	66
7.3.1. Artifact Removal.....	66
7.3.2. Initial Bone Mask Formation	67
7.3.3. Edge Detection and Seed Growing	68
7.4. Best Template Detection and Object Recognition.....	71
7.5. Final Bone Segmentation and Artery Detection Results	73
7.5.1. Catheter Masking	73
7.5.2. Edge Merging and Bone Segmentation.....	75
7.5.3. Artery Detection.....	78
7.6. Hemorrhage Detection, Segmentation and Quantitative Measurement.....	80
7.7. Outcome Prediction.....	88
7.8. Discussion	91
CHAPTER 8 RESULTS AND DISCUSSION – SPLEEN SEGMENTATION.....	94
8.1. Introduction.....	94
8.2. Dataset.....	94

8.3. Artifacts Removal and Contrast Enhancement	94
8.4. Bright Objects Mask Formation and Edge Detection	98
8.5. Bright Objects Segmentation and Masking	99
8.6. Spleen Segmentation.....	101
8.7. Discussion	105
CHAPTER 9 CONCLUSION AND FUTURE WORK	107
9.1. Introduction.....	107
9.2. Conclusions.....	108
9.3. Future Work	109
Bibliography.....	111

List of Tables

	Page
Table 7. 1. Performance of the proposed hemorrhage detection method.....	82
Table 7. 2. Performance of different classifiers with outcome being home or rehabilitation	90
Table 7. 3. Performance of different classifiers with outcome being ICU days	90
Table 8. 1. Performance of the proposed method in detecting spleen	104

List of Figures

	Page
Figure 1. 1. Block diagram of the proposed system.....	9
Figure 2.1. Setup for preprocessing and initial bone segmentation	12
Figure 2.2. Overview of bones and blood vessels in the pelvis [82]	13
Figure 2.3. Shape matching and object recognition.....	18
Figure 3.1. Overview of artery detection and masking process.....	20
Figure 3.2. Patient image with catheter inserted into body cavity (arrow points to the catheter).....	21
Figure 3.3. Approximate gray level ranges of various tissues in pelvic region.....	22
Figure 4. 1. Hemorrhage segmentation and quantitative measurement.....	31
Figure 4. 2. Region growing process	43
Figure 5. 1. Schematic diagram of the decision making system.....	48
Figure 5. 2. Flowchart of feature selection using SU based correlation filter	52
Figure 6. 1. Spleen (arrow points to the spleen) in Abdominal CT Image	56
Figure 6. 2. Overall process of spleen segmentation	56
Figure 7. 1. Sample results for artifacts removal	67
Figure 7. 2. Sample results for initial bone mask formation.....	68
Figure 7. 3. Sample results for edge detection and initial bone segmentation.....	71

Figure 7. 4. Sample results for best template matching and elimination of non bone objects	73
Figure 7. 5. Sample results for catheter and bright objects masking	74
Figure 7. 6. Sample results for edge merging, final bone segmentation and masking.....	77
Figure 7. 7. Sample result for common iliac arteries detection	78
Figure 7. 8. Sample result for external iliac arteries detection.....	79
Figure 7. 9. Sample result for internal iliac arteries detection	79
Figure 7. 10. Sample result for external/internal iliac arteries detection	79
Figure 7. 11. Sample hemorrhage detection results	82
Figure 7. 12. Sample hemorrhage detection results	83
Figure 7. 13. Performance of the proposed segmentation method.....	85
Figure 7. 14. Sample hemorrhage segmentation results	86
Figure 7. 15. Sample hemorrhage segmentation results	87
Figure 7. 16. Sample results of fracture and hemorrhage detection.....	89
Figure 8. 1. Sample preprocessing results.....	95
Figure 8. 2. Sample Gaussian filtering results	96
Figure 8. 3. Sample contrast enhancement results	97
Figure 8. 4. Sample bright objects mask results.....	99
Figure 8. 5. Sample bright objects segmentation and masking results	101
Figure 8. 6. Sample spleen segmentation results	103
Figure 8. 7. Performance of the proposed method in segmenting spleen	105

Abstract

HEMORRHAGE DETECTION AND ANALYSIS IN TRAUMATIC PELVIC INJURIES

By

Pavani Davuluri

A dissertation submitted in partial fulfillment of the requirements for the degree of Doctor of Philosophy in Engineering at Virginia Commonwealth University.

Virginia Commonwealth University, 2012

Major Director: Rosalyn Hobson Hargraves
Associate Professor, Department of Electrical and Computer Engineering

Traumatic pelvic injuries associated with high-energy pelvic fractures are life-threatening injuries. Extensive bleeding is relatively common with pelvic fractures. However, bleeding is especially prevalent with high-energy fractures. Hemorrhage remains the major cause of death that occur within the first 24 hours after a traumatic pelvic injury. Emergent-life saving treatment is required for high-energy pelvic fractures associated with hemorrhage. A thorough understanding of potential sources of bleeding within a short period is essential for diagnosis and treatment planning. Computed Tomography (CT)

images have been widely in use in identifying the potential sources of bleeding. A pelvic CT scan contains a large number of images. Analyzing each slice in a scan via simple visual inspection is very time consuming. Time is a crucial factor in emergency medicine. Therefore, a computer-assisted pelvic trauma decision-making system is advantageous for assisting physicians in fast and accurate decision making and treatment planning. The proposed project presents an automated system to detect and segment hemorrhage and combines it with the other extracted features from pelvic images and demographic data to provide recommendations to trauma caregivers for diagnosis and treatment.

The first part of the project is to develop automated methods to detect arteries by incorporating bone information. This part of the project merges bone edges and segments bone using a seed growing technique. Later the segmented bone information is utilized along with the best template matching to locate arteries and extract gray level information of the located arteries in the pelvic region.

The second part of the project focuses on locating the source of hemorrhage and its segmentation. The hemorrhage is segmented using a novel rule based hemorrhage segmentation approach. This approach segments hemorrhage through hemorrhage matching, rule optimization, and region growing. Later the position of hemorrhage in the image and the volume of the hemorrhage are determined to analyze hemorrhage severity.

The third part of the project is to automatically classify the outcome using features extracted from the medical images and patient medical records and demographics. A multi-

stage feature selection algorithm is used to select the predominant features among all the features. Finally, boosted logistic model tree is used to classify the outcome.

The methods are tested on CT images of traumatic pelvic injury patients. The hemorrhage segmentation and classification results seem promising and demonstrate that the proposed method is not only capable of automatically segmenting hemorrhage and classifying outcome, but also has the potential to be used for clinical applications.

Finally, the project is extended to abdominal trauma and a novel knowledge based heuristic technique is used to detect and segment spleen from the abdominal CT images. This technique is tested on a limited number of subjects and the results are promising.

Novelty and Contributions

Hemorrhage is the major cause of mortality within first 24 hours after a traumatic pelvic injury. Therefore, it is very crucial to trauma caregivers to identify the source of hemorrhage quickly in order to make diagnostic decisions and treatment planning. The most prevalent tool for identifying the source of bleeding in traumatic pelvic injuries is Computed Tomography Images. Depending on the slice thickness, the number of CT images to be analyzed by the physicians may be large. Hence, it is time consuming to analyze manually. Analyzing all the images within a short period may lead to human error. In addition, simple visual inspection or traditional computational methods may not be able to extract hidden information in the images due to the low resolution of images, complex pelvic structures, etc. Therefore, an automated computer-assisted traumatic pelvic injury system is needed in order to assist the physicians to make quick and accurate decisions and for treatment planning in a short period.

A number of existing systems for traumatic injuries rely on the patient demographic information and features extracted from the physiological data to generate treatment recommendations. However, these systems do not consider information hidden in the medical images. The focus of this research is to process CT images for hemorrhage extraction by incorporating the bone and major artery information and to automatically classify the outcome in order to provide recommendations to physicians for fast and accurate decision making and treatment planning.

Identifying hemorrhage is very challenging due to the variation in image gray levels that can occur because of differences in patients, injury severity, presence of several arteries in the pelvic region, and bone variation. Described below, the methods presented in this dissertation have several novel components that address the above-mentioned challenges. In addition to hemorrhage segmentation and decision making in traumatic pelvic injuries, the research also focuses on segmenting spleen in abdominal CT images.

1. A modified pelvic bone segmentation and masking algorithm is proposed that constitutes the merging of edges, bone segmentation and masking.

Hemorrhage detection incorporates the information of bone to detect the major arteries in the pelvic region. The proposed hemorrhage detection involves the segmentation and masking of pelvic bones, which is crucial to avoid false alarms. The specified segmentation algorithm with bone merging enables the proper masking of bone region including the weak edges. This way of segmentation by merging will ensure a very accurate masking which facilitates the process of hemorrhage detection in later stages.

2. A novel algorithm is proposed for major artery detection in the pelvic region.

The majority of hemorrhage in pelvic region is either due to the rupture of arteries or the fracture of pelvic bones. As arteries and pelvic bones are located in various regions in the image, it is important to search the entire image for hemorrhage. As hemorrhage and arteries are of similar gray levels, incorporating artery gray level is very useful. This proposed method focuses on identifying the major arteries such as the aorta and its branches using the position of the segmented bone, template

matching and initial position detection. This proposed algorithm extracts the major arteries and their gray level information from the image. This helps in the elimination of non-hemorrhage regions and the identification of hemorrhage regions in the image.

3. A new hemorrhage detection and segmentation algorithm is proposed that locates the hemorrhage and segments the hemorrhage from the image.

All the non-hemorrhage regions including the masked bone and artery regions are eliminated using morphologic operations and the remaining hemorrhage is segmented using a novel rule based approach. This approach utilizes hemorrhage matching, rule optimization and region growing techniques in order to accurately segment the hemorrhage.

4. A modified classification technique is proposed that classifies the outcome based on the features extracted from medical images and patient medical records and demographics.

The features extracted from the medical images are very crucial in assessing the injury severity. The proposed method utilizes the extracted features and selects only the predominant features through a multi-stage feature selection process in order to automatically classify the outcome. The feature selection process helps minimize the over fitting of data.

5. A novel knowledge based heuristic approach is proposed for segmenting the spleen from the abdominal CT images in order to detect lacerations and hemorrhage.

Automated spleen segmentation is a crucial step in detecting laceration and hemorrhage in abdominal trauma. Segmentation of spleen is very challenging due to

the difference in patients, poor image quality etc. The proposed approach is a fully automated segmentation technique that is adaptive to each and every image. This approach utilizes vertebrae and ribcage information to accurately locate the spleen and segments spleen using edge merging and threshold based techniques.

CHAPTER 1 INTRODUCTION

1.1. Introduction

This chapter describes the motivation and problem statement of the proposed research. Then, a brief review of existing methodologies in analysis of medical images is described. Finally, a brief description of the proposed approach is provided.

1.2. Motivation and Problem Statement

Trauma is a major health problem in the United States causing significant morbidity, mortality and increased health care costs [1]-[2]. It is the leading cause of death in Americans under the age of 44 and is the fifth leading cause of death in all ages [3]-[4]. Trauma survivors often suffer significant physical health problems which in some cases lead to lifelong disabilities and/or result in great emotional and financial toll not only on them but also on their families [2], [5]-[6]. Many fatal complications and long-term disabilities can be reduced by improving the quality of trauma care through accurate decision-making [7]-[10]. Trauma care involves considering a large amount of complex data. Since time is often limited, errors can occur and result in adverse outcome even in established trauma centers with experienced trauma care professionals [11]-[14]. The errors can also be due to unstable patients, incomplete histories, executing concurrent tasks, involvement of many disciplines, etc. [15]-[17]. However, majority of these mistakes result from human errors either due to delays in decision-making and treatment or

the caregiver giving insufficient attention to the details hidden in patient information. This is because decisions for critical injuries are made at a very quick pace, typically in stressful environments and must take into account several patient parameters such as blood pressure, CT images, trauma scores etc. Hence, there is a need for an automated computer-assisted decision making system that processes all available patient information and make recommendations to physicians [14].

Several decision-making systems have been developed in the last two decades to form recommendations in order to improve the care given to the patients. However, the majority of these systems rely mainly on the patient demographics to find similarities to cases in trauma databases and provide a recommendation based on these cases. As a result, the recommendations might be too specific and thus preclude practical implementation [18].

Focusing on the application addressed in this project, i.e. traumatic pelvic injuries, detecting the presence and extent of hemorrhage is an extremely important step in assessing the severity of pelvic injury. Hemorrhage is the leading cause of death in patients with traumatic pelvic fractures [19]-[21]. These fractures are majorly associated with motor vehicle accidents, falling from heights, and crush injuries [22]-[25]. The mortality rate for pelvic fractures range from 5% to 15% and the mortality rate for pelvic fracture patients with hemorrhagic shock ranges from 36% to 54% [19], [21], [26]-[29]. The majority of deaths caused due to hemorrhage occur within the first 24 hours after the injury [19], [26], [30]. Hence, it is very important to quickly and accurately identify the source of bleeding and control the hemorrhage in a very short period.

Contrast-enhanced CT has been widely used by the radiologists in recent years for the examination of hemorrhage and characterization of fractures in traumatic pelvic injuries [19], [27], [30]-[31].

The technology of CT image acquisition was developed during the seventies for applications in radiological diagnostics. CT imaging uses x-ray energy to create a series of 2D transversal images of the body. The radiation that passes through the body is measured by the detectors placed on the opposite side of the body across the transmitters. Every CT slice comprises of a large number of pixels that are associated with the attenuation values of the tissue located at the corresponding point. Attenuation values are calculated based on multiple intensity readings of the radiation that pass through the tissue during a CT scan.

The average of the attenuation values for pixels will constitute a numeric value that is associated with a pixel in the CT image. This average value is measured in Hounsfield unit (HU). The dynamic range of HU is 2000 units, 4000 or more in modern CT scanners, divided as follows: -1000 for air, lung tissue -400 to -600, fat tissue -60 to 100, water 0, soft tissue 40 to 80, and bone 400 to 1000.

As CT images consist of a wide range of gray levels between the tissues, it is difficult for human eyes to distinguish among such a large number of gray level values. In addition to this, depending on the slice thickness, it is rather time consuming for the radiologists to examine all the pelvic images. There is also variation in gray levels between the same organs from one slice to another. As time is a crucial factor in emergency medicine, a system that would minimize the time to accurate treatment planning could dramatically impact the field.

Automated detection of hemorrhage from CT images is very challenging. This is due to the injury severity, variation in bleeding gray levels from patient to patient, variation in size and shape of the bone, and the presence of several arteries in the region that may be injured. In addition to these, presence of image noise, partial volume effects and inhomogeneities, etc. make the task of hemorrhage detection very complicated. To overcome these challenges, anatomical information must be incorporated. Since hemorrhage in pelvic region is most often due to the fractured bone or, ruptured arteries/ veins etc., locating bones and major arteries may improve the hemorrhage detection process. **This research proposes an automated computer-assisted system that processes CT images for hemorrhage detection and combines the extracted features with all available patient information to provide recommendations to physicians.**

Few solutions have been proposed for hemorrhage segmentation in the pelvic region [32]. These studies utilized a threshold-based method to segment hemorrhage. Furthermore, the method is only able to segment hemorrhage located in one particular region in the image. Even though there are very few studies on hemorrhage segmentation in pelvic region, there are several studies on medical image segmentation for various applications such as vascular segmentation, bone segmentation, hemorrhage segmentation, etc. [33]-[35]. The majority of vascular segmentation is conducted on the coronary arteries and aorta tree on 3D angiogram images. These are briefly described in the following sections.

1.3. Image Segmentation Techniques

In recent years, several studies have been conducted on medical image segmentation. The current existing methodologies in image segmentation are classified into different categories: threshold based methods, region growing methods, clustering, Markov random field (MRF) models, artificial neural networks, deformable models, atlas based methods, level set methods etc. Brief description of these methods is given below:

- **Threshold-based methods:** Segmentation methods based on thresholding are one of the simplest methods used for segmentation. In these methods, the pixels in the image are classified into groups based on some predefined threshold value [33], [35]-[41]. Though these methods are simple, choosing a single threshold value will generate only two classes. Therefore, thresholding cannot be used for multi channel images. In addition to this, thresholding does not account for spatial characteristics of an image making it sensitive to noise and intensity inhomogeneities.
- **Region growing methods:** Region growing techniques are used to segment regions based on some similarity criteria. In these techniques, a seed is selected initially and all the pixels around it are added to the region based on some predefined criteria [33], [35], [42]-[47]. Each region of interest (ROI) requires seed initialization. This seed initialization can be achieved by manual, semi automatic or fully automatic selection. The drawbacks of these methods are they are sensitive to the seed selection and sometimes the similarity criterion is not exactly defined. In addition, these techniques are dominated by the growth of the current region. Overall, region growing methods are simple techniques that provide

good results especially with smaller region segmentation once the above-mentioned challenges are properly addressed.

- **Clustering methods:** Clustering techniques partition data into a certain number of clusters. These techniques are unsupervised techniques that iteratively alternate between segmenting the image and characterizing the properties of each cluster. Some commonly used clustering techniques for segmentation are fuzzy c-means algorithms, K-means clustering, Kernel based methods, etc. [33], [35], [48]-[50]. Though these techniques are computationally fast, these techniques do not incorporate spatial modeling. Therefore, they are either sensitive to noise or intensity inhomogeneities.
- **Markov Random Fields:** These models are statistical models used within the segmentation methods. These techniques model spatial interactions between neighboring pixels [33], [51]-[52]. The advantage of these models is their local dependency which provides a mechanism of modeling a variety of image properties. The drawback of these models is the difficulty in proper selection of parameters controlling the strength of spatial interactions. In addition to these, the energy function associated with most non-trivial MRF problems is extremely convex and the minimization problem is computationally very expensive and time consuming. In order to reduce the computational burden, some hybrid approaches using multi resolution are created that start processing images at a coarse resolution and then progressively refine them to a higher resolution [53]-[55].
- **Artificial neural networks:** Some researchers have used artificial neural networks for the segmentation [33], [35], [42], [56]-[57]. Artificial Neural networks are parallel networks of processing elements that simulate biological learning. These networks have

high parallel ability and high interaction among the processing units enabling it to model any kind of process. However, these networks need to be trained beforehand. In addition, the amount of time taken for training may be very long and the results of these networks are influenced by initialization.

- Deformable models: Deformable model techniques are other techniques that are used for segmentation [35], [58]-[64]. These techniques use closed parametric curves or surfaces that deform under the influence of internal and external forces. These techniques incorporate a smoothness constraint that provides robustness to noise and spurious edges. However, the disadvantages include poor convergence to concave boundaries and sensitivity to initialization.
- Level set methods: Level set methods were originally used as numerical technique for tracking shapes and interfaces, and have been increasingly applied for image segmentation. These methods are based on a moving contour as the zero-level set of a time evolving scalar function over a regular grid [65]-[67]. The curve is deformed according to a given set of partial differential equations. These calculations are often time consuming and may not converge to the best result [68].
- Atlas-based Methods: These methods are based on a standard template or atlas [35], [69]-[72]. The atlas is created based on the information on the anatomy that requires segmentation. The created atlas is then used as a reference for segmenting new images. The atlas-based methods are useful only for the segmentation of structures that do not exhibit great variation and are not extremely detailed.

Along with these segmentation techniques, there are other techniques such as watershed techniques that use concepts from edge detection and mathematical morphology to partition image into homogeneous regions [73]-[76]. These techniques suffer from over segmentation. However, recent studies have developed improved methods to overcome some of the drawbacks to segmentation [77]-[78].

1.4. Proposed Method

The methodology proposed here is a multi-stage hierarchical technique that applies some of the methods discussed above. In particular, the algorithm provides a novel approach for artery detection based on the anatomical knowledge of bone and detecting hemorrhage in the entire image from the artery gray level information. The technique also introduces a multi-stage bone segmentation technique that deals with the variations typically observed in biomedical images.

The ultimate goal of the project is to segment the pelvic CT images and extract features from these images and provide recommendations that can be directly used for diagnosis and treatment planning. The block diagram of the system components is presented in figure 1.1.

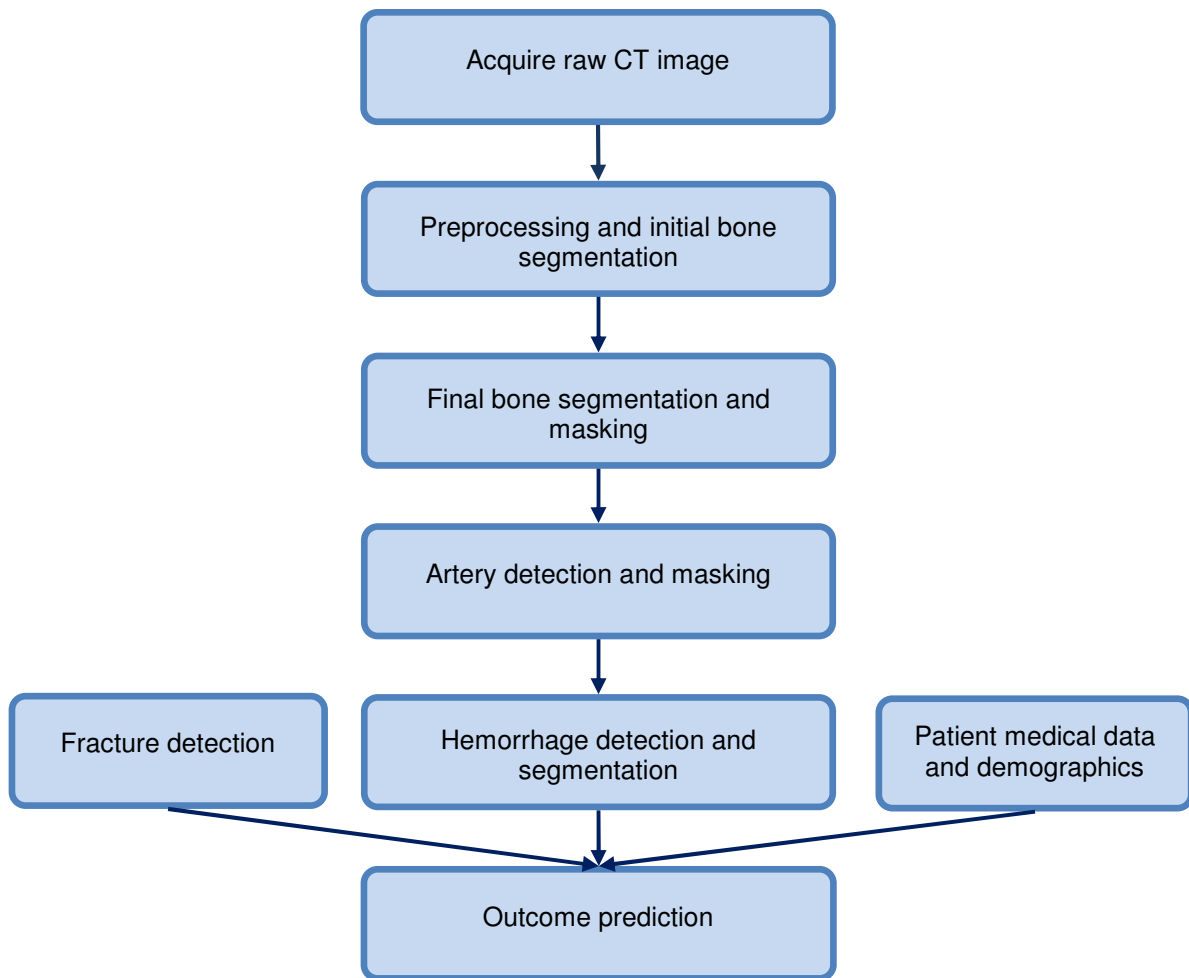


Figure 1. 1. Block diagram of the proposed system

In addition to traumatic pelvic injuries, the project has been expanded to the abdomen region to segment solid organ, spleen from the CT images of abdominal trauma patients.

The rest of the dissertation is organized as follows: Chapter 2 describes the pelvis anatomy, preprocessing, and initial bone segmentation. Chapter 3 describes the final bone segmentation through edge merging. This chapter also provides the methods to detect major arteries in the pelvic region. Chapter 4 describes the final steps in hemorrhage detection. This chapter presents a rule based approach to segment hemorrhage from the

images. Chapter 5 presents the methods to classify the outcome using the extracted features and patient medical records and demographics. Chapter 6 describes the multi-stage spleen segmentation process. Chapters 7 and 8 present the results obtained from the described methods to detect and segment pelvic hemorrhage and spleen. Finally, the conclusions and a plan for future work are given in chapter 9.

CHAPTER 2 PREPROCESSING AND INITIAL BONE SEGMENTATION

2.1. Introduction

Accurate hemorrhage detection requires the incorporation of anatomical information from the pelvic region. Since a hemorrhage can be due to a fractured bone or ruptured arteries/veins, it is vital to identify and locate these objects in the pelvic region. This chapter describes the anatomy of the pelvis, preprocessing of the raw pelvic CT images and initial bone segmentation. As a CT scan may include large number of images, manual or semi-automated methods may consume a large amount of time which is unfeasible when treating a critically ill patient. The proposed methods in this chapter are fully automated. Figure 2.1 gives the overall setup for preprocessing and initial bone segmentation.

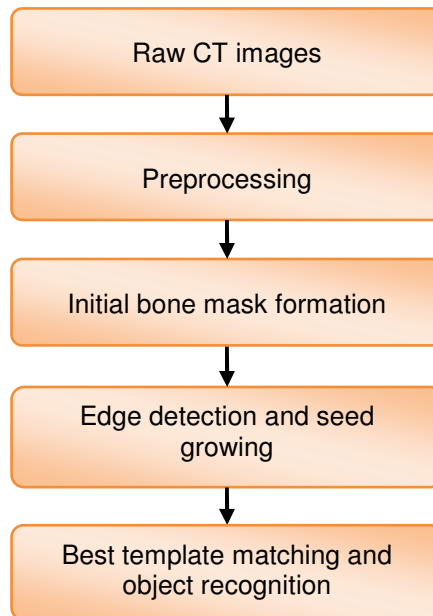


Figure 2.1. Setup for preprocessing and initial bone segmentation

The work proposed here is a continuation of the work done by Vasilache et. al. on segmentation of bone in pelvic CT images [79], [80]. In this chapter provides background on the work already completed by Vasilache [79], [80] with a few modifications required for improved edge detection and bone template selection.

2.2. Anatomy of the Pelvis

The pelvis is a bony ring, placed between the movable vertebrae of the vertebral column, which it supports, and the lower limbs upon which it rests. The pelvis serves three functions in the human body. First, it transmits weight from the axial skeleton to the lower limbs in the standing position or to the ischial tuberosities when sitting. Second, it provides attachments for numerous muscles, which control the lower limbs. Third, it houses the terminal parts of the digestive and urinary tracts and the reproductive systems of males and females [81]. In general, the female pelvic bones are more delicate and shallower than the male pelvic bones. The pelvis is composed of four bones: the two hip bones laterally in front and the sacrum and coccyx behind. The hipbone is a large flattened, irregularly shaped bone, restricted in the center and expanded above and below. It consists of three parts, the ilium, ischium, and the pubis. These are distinct from each other in the young subjects, but are combined in the adult. The sacrum is a large triangular bone situated in the lower part of the vertebral column and at the upper and back part of the pelvic cavity. Its upper part articulates with the last lumbar vertebra and its apex with the coccyx. Coccyx is the last bone in the vertebral column. Many large nerves and blood vessels pass through

the pelvis and go to the legs. The largest blood vessel in the human body is the aorta. It carries blood from the heart and descends through the chest and the abdomen. The aorta divides on the left side of the body of the fourth lumbar vertebra (L4), into the two common iliac arteries. These arteries again divide as they descend from the end of the aorta and each divides between the last lumbar vertebra and the sacrum into the external iliac artery, which supplies blood to much of the lower limbs and the internal iliac artery, which supplies blood to the viscera and the walls of the pelvis. There are also many other small arteries branched out from these major arteries in the pelvic region. Figure 2.2 shows the bones and blood vessels in the pelvis.

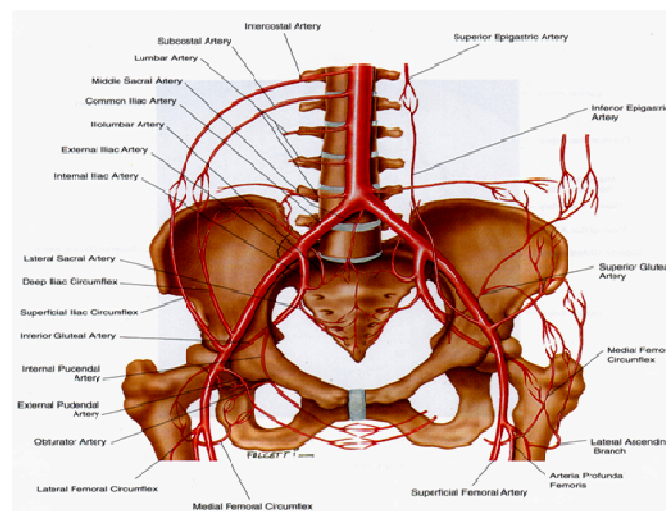


Figure 2.2. Overview of bones and blood vessels in the pelvis [82]

2.3. Preprocessing

Raw CT images contain artifacts such as cables, hands, CT table, etc. and in some cases include lower extremities. The goal of preprocessing is to remove artifacts present in

the image and extract the pelvic region. This is achieved using morphologic operations and blob analysis. Firstly, a binary version of the raw image is created. All the pixels with gray level greater than an adaptive threshold become one while all the pixels with gray level less than that threshold become zero. Secondly, morphological operations are applied to the binary image. Morphological operations help disconnect components in the image. This allows the selection of pelvic region in the image later. Thirdly, blob analysis is used to select the object with the largest area. This selection is based on the assumption that the pelvic region is larger in area than the area of the artifacts present in the image. This blob analysis includes computation of general statistics like the area and, centroid of the regions present in the image. Finally, a mask is created for the object identified with the largest area. This mask enables the selection of the pelvic region and eliminates the background artifacts from the original image.

2.4. Initial Bone Mask Formation

Once the pelvic region is extracted, the next stage is to segment bones in the image. Bone segmentation will make the task of determining the artery location easier. This is explained in detail in chapter 3. From now on, the extracted pelvic region image will be referred as the original image.

The first step for initial bone mask formation is to apply wavelet analysis on the original image from the previous step in order to reconstruct the image using only the approximation matrix. The CT image exhibits sudden changes in gray level at the boundaries between different types of tissue. In order to eliminate these discontinuities and

facilitate the processing, a mother wavelet is used in the analysis. Haar wavelet is selected as the mother wavelet because of its discontinuity and intrinsic ability to accentuate transitions between gray levels. This step helps in enhancing the gray level transition at the borders.

The second step is to calculate the mean and standard deviation of the gray level values of the non-background pixels. These calculated values are later used for automatic threshold selection. The background pixels are not used in the calculation because including background pixels can greatly distort the gray level statistical properties of the pelvic region.

The final step is to determine a threshold value t_1 and create an initial binary mask for bone by thresholding the filtered image. This is achieved using equation 2.1.

$$t_1 = m_1 + s_1 \quad (2.1)$$

where m_1 and s_1 are the mean and standard deviation of the gray level values of non background pixels. The binary mask is created by selecting the pixels that have gray levels greater than the threshold t_1 . This is considered as initial binary bone mask. Choosing this threshold facilitates the selection of pixels situated on the brighter end of the gray scale spectrum. This increases the chance of selection of pixels that lie within the same gray scale range of bone gray level values.

2.5. Edge Detection and Seed Growing

The obtained initial binary bone mask is refined and an intermediary binary mask is created. As part of this process, the first step in this stage is noise reduction in the images.

CT images may contain noise that can affect local aspect and features of the objects of interest as well as reduce the overall quality of the image. Therefore, a low pass filter is used to reduce the speckle noise present in the images. A 2D Gaussian low pass filter is used. This filter is constructed based on the equation given in 2.2.

$$G(x, y) = \frac{1}{2\pi\sigma^2} e^{-\frac{x^2 + y^2}{2\sigma^2}} \quad (2.2)$$

where x and y are the distances from the origin on the horizontal and vertical axis respectively, and σ is the standard deviation of the Gaussian.

The resulting filtered image will appear smoother as the texture is eliminated. Eliminating texture creates regions with more uniform gray levels. Later, a Laplacian filter is applied to the resulting image and the result is multiplied with the initial binary mask to obtain an intermediary, refined bone mask. A Laplacian filter is selected for processing due to its ability to enhance horizontal, vertical and diagonal positioned edges. An intermediary, refined bone mask is then obtained through binary multiplication of the initial binary mask and the filtered image.

The seeds are grown by detecting the edges of the refined mask. This is achieved using Canny edge detection. This detection technique is used because of its ability to detect true strong and weak edges and it is less susceptible to noise. Later, morphological operations are applied to remove the spurious edges and objects with area smaller than 30 pixels. Experimental testing revealed that a value of 30 is a suitable choice for this application. The obtained edges of the bones are used as seeds in the seed growing technique for bone segmentation.

2.5.1. Seed Growing

Once the seeds are determined, then the region is grown in the neighborhood of the pixels from the seeded bone mask. This enables the selection of pixels closer to the true edge of the bone region. Region growing is accomplished in three steps. The first step is to identify the neighborhood of each seed and to determine the gradient for each seed and the average gradient in the neighborhood. The second step is to identify neighbors of neighbors and determine the average gradient within that neighborhood. The third step is to decide on inclusion of a new pixel to the region. A new pixel is included in the region based on three conditions: 1. the neighbor is located on the inside of the edge, 2. the neighbor's gray value is greater than the average gray value of the neighbors in the neighborhood, 3. the gradient value corresponding to the neighbor is higher than the average gradient value. These steps are repeated until the maximum number of iterations is reached or the number of pixels added in that specific iteration is less than one tenth of the region. The obtained image is the initial segmented bone image.

2.6. Best Template Matching and Object Recognition

The segmented images may include objects that have gray values similar to bone. Therefore, it is important to eliminate these non-bone objects. These objects can be contrast-enhanced regions, arteries etc. In order to eliminate these objects, best template matching technique is used. In this technique, each image is compared to a set of 73 bone templates and the template with low matching cost is chosen as the best template. These

bone templates are created through an offline process, by manual selection of bone tissue regions. The CT images used to create these bone templates are part of the Visible Human Project dataset. This shape matching technique is explained in detail in [77]. Once the best matched template is determined, then the objects in the segmented image are sequentially eliminated and the matching cost is determined. If the object eliminated in the image is a non-bone object then the matching cost decreases. If the eliminated object is a bone, then the matching cost increases. Depending on the matching cost, the objects in the segmented image are eliminated. Hence, the obtained image after the elimination of non-bone objects is considered as the desired initial segmented bone image. The overall process of best template matching and object recognition is shown in figure 2.3.

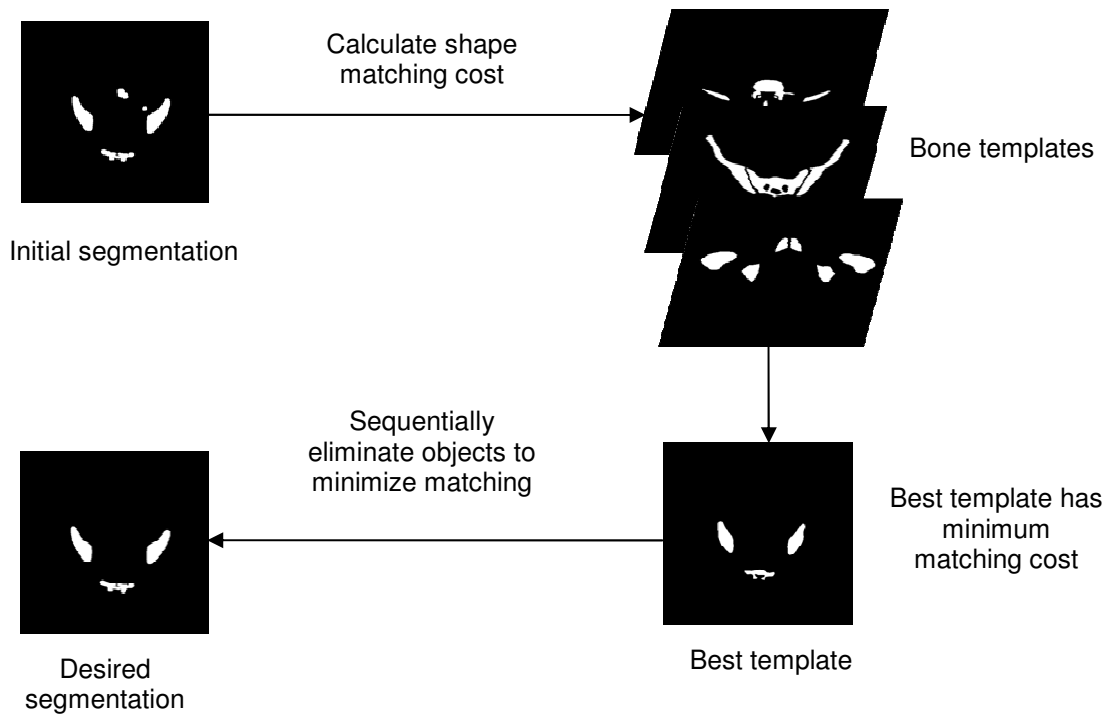


Figure 2.3. Shape matching and object recognition

CHAPTER 3 ARTERY DETECTION

3.1. Introduction

Bone segmentation and artery detection facilitate the process of hemorrhage detection. Chapter 2 described the preprocessing and initial bone segmentation. For hemorrhage located close to the bone, it is very important to distinguish between hemorrhage and bone pixels. The bone segmentation method described in chapter 2 may not be able to segment bone pixels in an image if the bone edge gray levels are similar to the gray levels of soft tissues. Therefore, in that scenario, it may become difficult to distinguish hemorrhage and bone pixels. As mentioned earlier, hemorrhage is due to fractured bone, arteries, etc. Therefore, hemorrhage, if present, will be located close to the fractured bone or arteries. The incorporation of major artery location and gray level information will help detect hemorrhage and will provide the basic information of gray level range of hemorrhage pixels.

This chapter presents an automated method for segmenting bone and for detecting major arteries in the pelvic region with the knowledge of segmented bone. Figure 3.1 shows the overall process of artery detection. The initial bone segmentation step in the artery detection process is the work done by Vasilache et. al. on segmentation of bone in pelvic CT images [79], [80]. However, few modifications are made to edge detection and template selection stages.

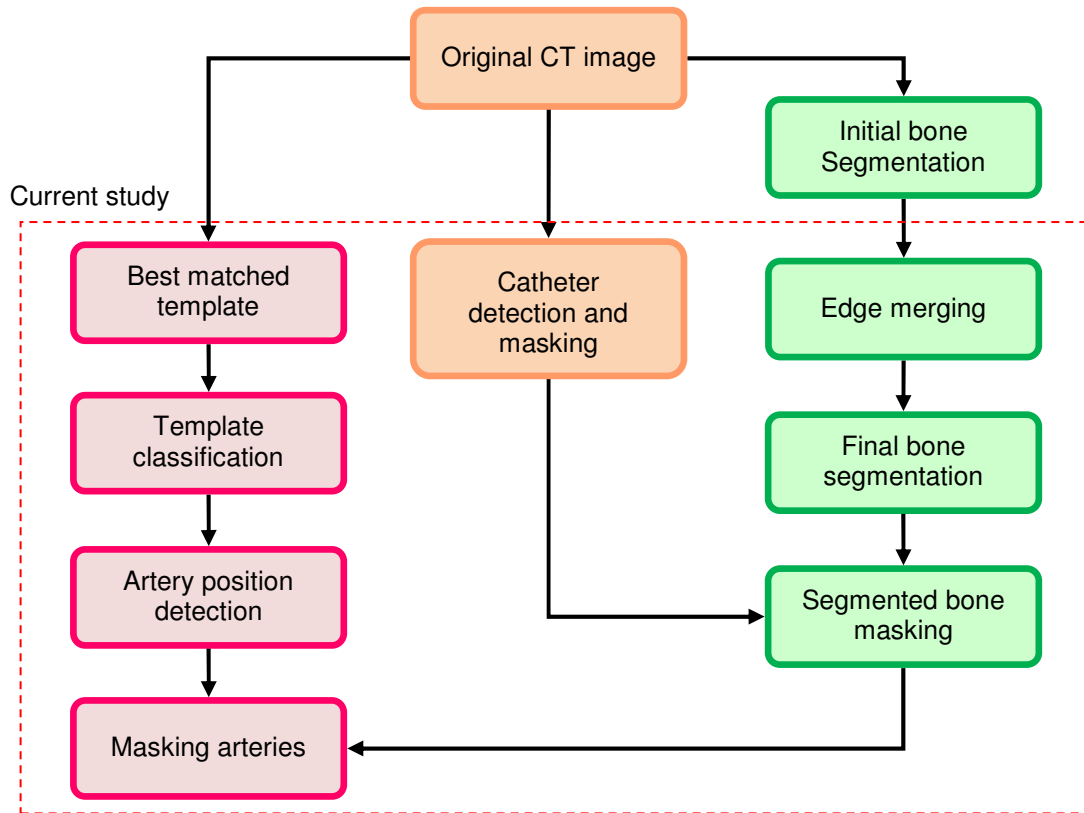


Figure 3.1. Overview of artery detection and masking process

3.2. Catheter Masking

Hemorrhage in pelvic region can be due to rupture of arteries, veins, and fractured bones etc. Pelvic region consists of several arteries such as aorta and its branches, obturator artery, common iliac veins etc. These arteries and veins are positioned at different parts of the pelvic region. Therefore, entire image must be searched for hemorrhage. Since the entire image is searched for hemorrhage, it is important to mask catheters or any contrast enhanced tissues like bowel, calcified arteries, etc. to minimize false hemorrhage detection.

A catheter (urinary bladder or intravenous) is inserted into a body cavity for instillation of contrast during CT to assess urinary bladder injury or for fluid infusions. This catheter may not be visible on all CT images. If placed in the femoral vein, it is visible on all CT images. Figure 3.2 shows the image of a patient with catheter inserted into the body.

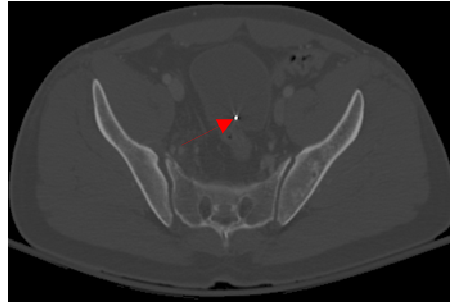


Figure 3.2. Patient image with catheter inserted into body cavity (arrow points to the catheter)

Based on discussion with expert radiologists and experimentation, it is observed that the pixels associated with these foreign objects have gray level values higher than the gray level values of other objects like arteries, veins and other soft tissues. Figure 3.3 shows the general gray level ranges for various objects in an image on a scale of 0 to 255. These ranges are provided based on the gray level values of the objects in 300 images. These images include the images taken during both arterial (phase in which the pelvic region is scanned soon after the injection of contrast enhancer) and veinal (phase in which the pelvic region is scanned with some delay after the injection of contrast enhancer) phase. A threshold based method is used to mask the catheter. The initial segmented bone pixels gray level values are determined for each image. The average gray level of the bone objects in the image is chosen as threshold for masking the catheter. If any pixels in the

original image have gray level values greater than the determined threshold value, then that pixel is considered as a catheter pixel and its gray level is set to zero. This is termed as catheter masking. Any objects with gray levels greater than the bone average gray levels are of no interest in this study and hence are masked in the image. During this process, if there are any other objects such as calcified arteries with gray levels greater than bone, then those objects are also masked. This masking is required in order to minimize the effect of gray level values of these objects on the overall gray levels of the image. In addition, masking helps reduce the false hemorrhage detection.

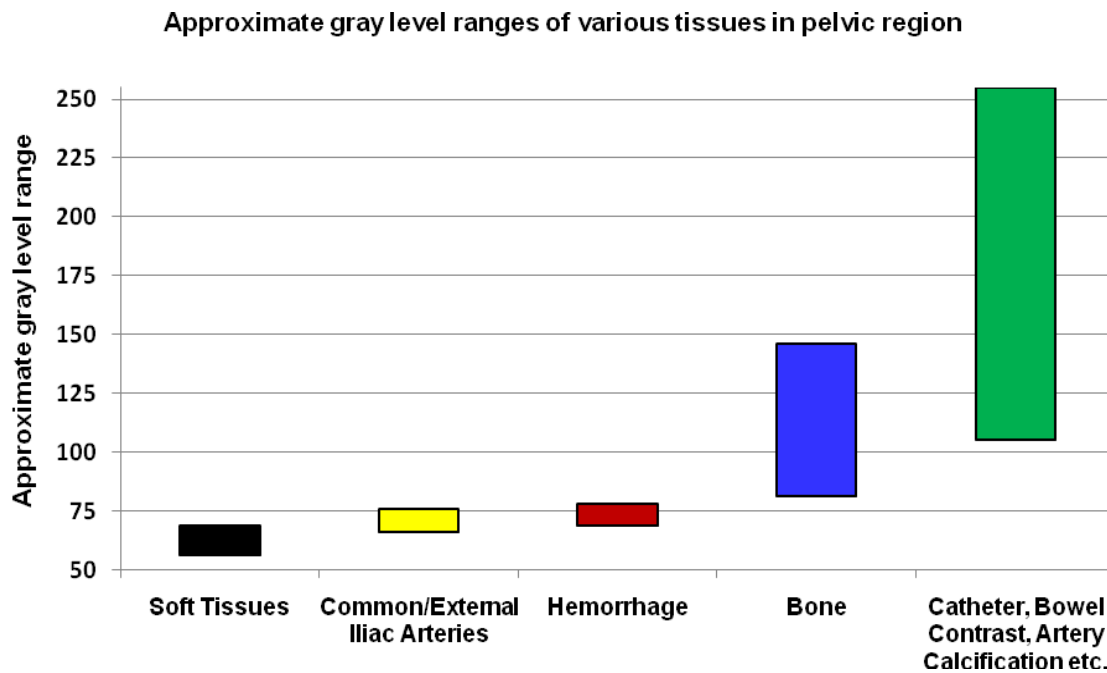


Figure 3.3. Approximate gray level ranges of various tissues in pelvic region

3.3. Final Bone Segmentation and Masking

The final bone segmentation consists of several steps: edge merging, bone segmentation, and masking. Each of these steps are described in detail below.

3.3.1. Edge Merging

The first step of bone segmentation is edge merging. For the initial segmented bone from chapter 2, the edges are determined using Canny edge detection. Since CT scan consists of several number of images, the gray level of the edges of the bone pixels in an image may be similar to that of soft tissue pixel gray levels and hence may not be segmented using the method discussed in chapter 2. Since each slice is of a few millimeters thickness, incorporation of bone information from previous and subsequent slices will help connect the disconnected edges or missing edges of the bone in the current image. Therefore, to ensure better masking of the bone, the edges of each bone in the current image are merged with the respective bone in the previous and the subsequent image. Since the study is not focused on fracture detection, slight variation in bone edges will have minimal effect on hemorrhage detection.

3.3.2. Bone Segmentation and Masking

After edge merging, the edges of the bones in the merged images are chosen as seeds and the seeds are grown around these edges using the seed growing technique described in chapter 2. Due to the conservative nature of the region growing technique, the pixels closer to the true edge of the bone are only selected even with the edge merging. Once the seeds

are grown, morphologic operations are performed to fill any holes in the bone region. The resulting binary image is the final segmented bone image.

After final bone segmentation, the segmented bone region pixels' gray level values are set to zero in the original image. This is bone masking. Masking bone region makes the task of hemorrhage detection easier.

3.4. Artery Detection

The major arteries in the pelvic region are the aorta and its branches. This study focuses on detecting aorta, common iliac arteries and their external and internal branches. Since artery and hemorrhage gray level ranges are similar, inclusion of artery gray level information will make the task of hemorrhage detection easy. The process of artery detection includes several phases including: template classification, initial artery position detection in the first image of the scan, aorta, common iliac and external iliac artery detection, and internal iliac artery detection.

3.4.1. Template Classification

The 73 bone templates used for determining the best matched template are used for template classification too. These bone templates are classified into four groups based on their CT images. This is done manually offline. These templates are classified into 4 groups based on the location of the arteries from the first image to the last image. Classification of templates will help identify the group to which the image in a scan

belongs. In the previous chapter, best template is determined for each image in a scan. The group to which the selected template belongs will be the group of the image.

3.4.2. Initial Artery Position Detection in the First Image of the Scan

After classification of templates, the templates in the first group are used to determine the initial arteries position in the first image of the patient scan. In this subsection, aorta or its external branches are referred to as arteries. Since pelvic CT scans taken in the hospital contain all images of pelvic region, the first pelvic image of a patient will be used to perform the template matching. The process of initial artery position detection involves a series of steps as follows:

Step 1: Determine the number of bone objects in the final segmented binary image. These bones can be lumbar vertebrae, sacrum, ilium etc. From anatomical aspect, if the number of bones in the image is less than or equal to 2 in the first template group, then it indicates that the aorta has not branched; otherwise it indicates that aorta has branched to common iliac arteries. In general, aorta branches to common iliac arteries at the fourth lumbar vertebrae (L4).

Step 2: Calculate the general statistical properties of all bones in the image. These statistics include centroid, bounding box, and area.

Step 3: If the number of objects in the image is ≤ 2 , then apply blob analysis to determine the object with largest area. Then,

- For the largest object, calculate the centroid (x_o, y_o) , and the bounding box coordinates $\mathbf{b}_o = (b_{o1}, b_{o2}, b_{o3}, b_{o4})$, where, b_{o1} , b_{o3} are minimum and maximum

horizontal position, and b_{o2}, b_{o4} are minimum and maximum vertical position of the largest object.

- Equation 3.1 gives the artery position. This position is the approximate position of the aorta, as it has not branched out to common iliac arteries.

$$\text{Artery Position} = (x_o, b_{o2} - 2 \times \text{slice thickness}) \quad (3.1)$$

Step 4: If the number of objects in the image is greater than 2, then it indicates that aorta has branched out to common iliac arteries. Then,

- Determine the object whose centroid horizontal coordinate x lies between minimum and maximum centroid horizontal coordinates of all the objects. Then among those objects, determine the object whose b_{i2} ($i=1, 2, \dots, m$) is minimum. m is the number of objects in the image.
- That object is considered as the desired object with centroid (x_o, y_o) and its bounding box coordinates as desired bounding box coordinates \mathbf{b}_o . The distance d moved by the artery from one image to another image is given by 3.2, and the arteries position is given in 3.3.

$$d = (b_{o3} - x_o) - \left\{ \left(\frac{b_{o3} - x_o}{s} \right) \times (s - j) \right\} \quad (3.2)$$

$$\text{Arteries Position} = (x_o \pm d, b_{o2} - k) \quad (3.3)$$

where s denotes the number of templates in the group.

The best matched template number is given by j , and k is the approximate distance between the object top most tip and the artery and is given as $k=5 \times \text{slice thickness}$. ‘ \pm ’ indicates left/right iliac artery.

Step 5: Conclude the above determined positions as the initial positions of arteries.

3.4.3. Aorta, Common Iliac and External Iliac Arteries Detection

After determining the initial positions of the artery, a window of size $N \times N$ is chosen around the determined artery position as ROI to detect artery. $N=50$ is chosen as the size of the neighborhood. This value is chosen because a larger window size may sometimes include tissues like bladder etc., and a smaller window may not cover the entire artery region. A histogram is determined for the non background pixels in the window in order to determine the two gray levels g_{min} and g_{max} that occur maximum number of times when compared to the other gray levels. A threshold t is determined from these gray levels in order to determine the arteries using equation 3.4.

$$t = \frac{g_{min} + g_{max}}{2} \quad (3.4)$$

All the objects in the selected window with gray level greater than the threshold are considered as objects of interest, and blob analysis is applied to determine the object with largest area. That object is considered as artery and its centroid its actual position. For all the consecutive images, the centroid of the artery from previous image is used as initial artery position to determine the current image's artery position by applying the same procedure used to determine the actual artery position of the first image.

Finally, after detecting the arteries, the average and maximum gray levels of the aorta/common/external iliac arteries pixels are determined for each image and later, all the arteries are masked i.e. the arteries pixels gray level values are set to 0. Therefore, arteries

are detected and masked. As hemorrhage pixel gray levels are similar to that of arteries, masking of these pixels reduce the false detection of arteries as hemorrhage.

3.4.4. Procedure to Determine Internal Iliac Arteries

The common iliac arteries do not branch out in the first image of the scan itself. So when the common iliac branches out to external iliac arteries and internal iliac arteries, internal iliac arteries must also be detected. Internal iliac arteries are smaller branches of common iliac arteries and they do taper off after few images. They are only present in few images.

Let the template of reference image (CT image of the template) at which common iliac artery branches out be T_d and let T_h ($d < h$) be the template of reference image at which they taper off completely. Let I_f be the first image of a patient whose best matched template is T_c ($d \leq c \leq h$). Let (a_1, b_1) , and (a_2, b_2) be the left and right external iliac artery positions for image I_f . Then the left (l_0, l_1) and right (r_0, r_1) internal iliac branch initial position is given by 3.5 and 3.6.

$$(l_0, l_1) = (a_1 + 2 \times p, b_1 + 2 \times p) \quad (3.5)$$

$$(r_0, r_1) = (a_2 - 2 \times p, b_2 + 2 \times p) \quad (3.6)$$

where, $p = c - d + 1$

Once the initial position of internal iliac branches of the image I_f are determined, the following image internal iliac arteries initial position is determined from the first image internal iliac arteries position and is given by equations 3.7 and 3.8.

$$Left\ iliac\ branch = \left(l_0 + 1, l_1 + \frac{slice\ thickness}{2} \right) \quad (3.7)$$

$$Right\ iliac\ branch = \left(r_0 - 1, r_1 + \frac{slice\ thickness}{2} \right) \quad (3.8)$$

These positions (l_0, l_1) , and (r_0, r_1) , of internal iliac arteries are used as initial positions for the subsequent image. This process is repeated iteratively for all the images whose best matched template number is less than or equal to h .

A window of size $N \times N$ around this initial position is generated and used as ROI to locate internal iliac arteries. Since internal iliac arteries further branch out and taper off after few images, it is important to locate all of the internal iliac arteries. For the selected window, the average gray level of the determined external iliac arteries is chosen as the minimum threshold and the maximum gray level as the maximum threshold. All the pixels whose gray levels lie between these thresholds are considered internal iliac arteries, and are masked in the same manner as external iliac arteries.

CHAPTER 4 HEMORRHAGE DETECTION AND SEGMENTATION

4.1. Introduction

Chapter 3 described methods for bone segmentation and artery detection. Bone segmentation is important; however the detection of the presence of active bleeding, localization of such a bleeding and quantitative measurement is of extreme importance. It is very challenging to detect hemorrhage accurately due to the presence of several arteries and bones in the pelvic region. In addition, bone variations from patient to patient and poor quality images make hemorrhage detection even more challenging. Incorporation of anatomical information such as artery gray level information is very helpful. Even then, arteries and bones are not the only landmark regions in the pelvic image. There are other organs (e.g. bladder), veins etc. that are found in the region. Masking of bone and contrast enhanced objects remove the brighter unwanted regions (objects) from the image. Masking arteries remove the regions with gray levels similar to bleeding. However, there are regions in the image with gray level less than the artery gray levels, and also regions that fall within the same gray level of arteries. If these are present in the image, there is a chance for false detection of these regions as hemorrhage.

This chapter presents the methods to mask these unwanted regions and detect the hemorrhage. Later, a multi-stage rule based segmentation technique is described. The volume measurement of hemorrhage is also described in this chapter. The overall process of hemorrhage detection and segmentation is shown in figure 4.1.

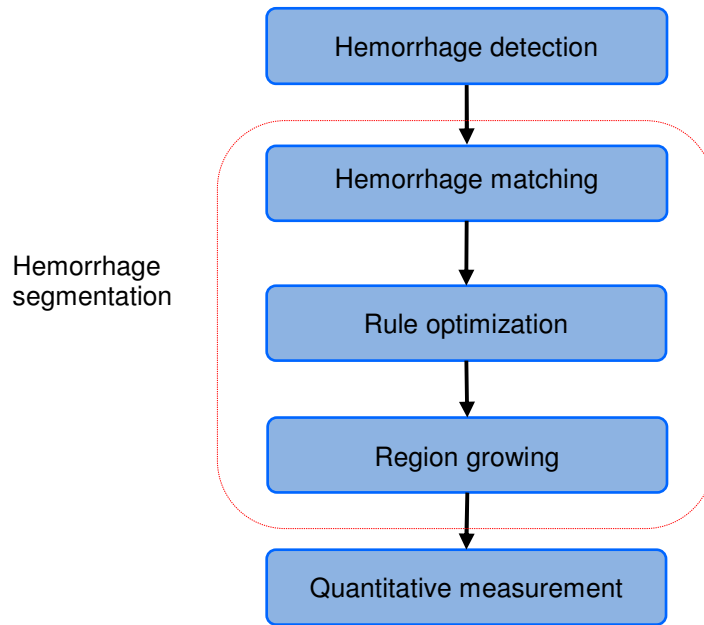


Figure 4. 1. Hemorrhage segmentation and quantitative measurement

4.2. Unwanted Objects Filtration

Even though bones and arteries are masked, there is a chance that some residual pixels are left behind due to lower gray levels of the artery or may be due to the fractured bone pixels. Along with these regions, the regions with gray level values less than arteries are present in the image. These regions are other soft tissues present in the image and must be filtered. This filtration process is described in the following steps.

Step 1: All objects whose pixels gray levels are less than the average gray level of previously detected arteries are eliminated. Hence, the image will be left with hemorrhage and/or some residual bone and isolated artery pixels that are not masked in the earlier stages and fall within these gray levels. These are eliminated in the following steps.

Step 2: Morphological operations are applied to remove any isolated pixels present in the image.

Step 3: This step is to eliminate any residue bone pixels present in the image. This is done by comparing the detected unwanted object pixels to all previous images in the scan to see if any of those regions are masked in those images. If masked, then those pixels gray levels are set to zero.

Step 4: Finally, image sliding method is applied to eliminate the objects that are present in current image and not present in either previous or subsequent image. This eliminates any regions whose gray levels are similar to that of arteries. Therefore, all the unwanted pixels are eliminated.

4.3. Hemorrhage Detection

After the removal of the above mentioned unwanted regions, if the image has any objects present, then those objects are considered as hemorrhage otherwise there is no hemorrhage in the image. Blob analysis is then used to determine the centroid of the detected hemorrhage. This centroid is used to select a window during the hemorrhage segmentation process described in the following subsections.

The hemorrhage detected may not be the complete region of hemorrhage especially during the veinal phase. If some of the hemorrhage pixels gray levels are similar to that of soft tissues, especially during the veinal phase, then those pixels would have been eliminated during the filtration of unwanted objects. In addition, the gray levels of hemorrhage that lie within artery gray levels and higher are considered as hemorrhage.

However to identify the hemorrhage severity, the entire hemorrhage region must be known.

4.4. Hemorrhage Segmentation

Another important challenge is the identification of bleeding next to the bone, as the hemorrhage can occur due to the fractured bones. Hence, it is important to segment the hemorrhage region accurately when present next to the bone. The proposed segmentation process consists of hemorrhage matching, rule optimization and region growing which are described in detail in the following subsections [83].

4.4.1. Hemorrhage Matching through Mutual Information

The first step of hemorrhage segmentation is hemorrhage matching. The hemorrhage region detected using the previously mentioned method does not contain all the hemorrhage pixels especially the boundaries of the hemorrhage. Hemorrhage matching helps identify the threshold, i.e., the optimum minimum gray level G_{opt} for segmenting the hemorrhage region. This is accomplished using the mutual information (MI). First, a window of size $q \times q$ in the preprocessed CT image is selected as a region of interest (ROI) around the centroid of the detected hemorrhage. The range $[G_{min}, G_{max}]$ of the hemorrhage gray levels are then determined from the detected hemorrhage. Then a gray level G_{mi} , where $G_{min} \leq G_{mi} \leq G_{max}$ is chosen as the minimum gray level and all the pixels in ROI that lies within $[G_{mi}, G_{max}]$ are chosen as hemorrhage pixels. Morphologic operations are performed to eliminate any non hemorrhage regions in each of these determined

hemorrhage images. This obtained hemorrhage image is individually compared to the initial detected hemorrhage image using mutual information technique in order to find the amount of information each image contains about the detected hemorrhage [84]. This MI is calculated between the previously detected hemorrhage image and the hemorrhage images obtained for different gray level ranges. The cut-off gray level that contains the maximum information about the detected hemorrhage is considered as the optimum minimum gray level G_{opt} at this stage. The mutual information in this process is determined in the following manner. Let C_d be the detected hemorrhage image from the previous section, and let $\{B_1, \dots, B_i, \dots, B_m\}$, where $i=1, 2, \dots, m$ be the hemorrhage regions obtained with the initial cutoff that ranges within $[G_{min}, G_{max}]$. The mutual information between images C_d and B_i is determined using equation 4.1.

$$MI(C_d, B_i) = H(C_d) + H(B_i) - H(C_d, B_i) \quad (4.1)$$

Where, $H(C_d)$, and $H(B_i)$ are the entropies of images C_d and B_i and $H(C_d, B_i)$ is their joint entropy, and are computed as follows:

$$H(C_d) = - \sum_c P_{C_d}(c) \log P_{C_d}(c) \quad (4.2)$$

$$H(B_i) = - \sum_b P_{B_i}(b) \log P_{B_i}(b) \quad (4.3)$$

$$H(C_d, B_i) = - \sum_{c,b} P_{C_d, B_i}(c, b) \log P_{C_d, B_i}(c, b) \quad (4.4)$$

Where, $P_{C_d}(c)$, $P_{B_i}(b)$ denote individual probability distributions. $P_{C_d, B_i}(c, b)$ denotes the joint probability distribution of the images.

The cut-off gray level for which the mutual information between C_d and B_i is maximum is the optimum gray level G_{opt} and the image is the optimum image at this stage

of segmentation. The pixels within the image that lie within $[G_{opt}, G_{max}]$ are considered as hemorrhage pixels and G_{opt} is considered as the minimum hemorrhage gray level from now on. However, G_{opt} may not be the actual minimum gray level of hemorrhage as these cut off gray levels are from the detected hemorrhage and may not include all the hemorrhage pixels such as boundary pixels which might have gray levels less than G_{opt} . These undetermined hemorrhage pixels are segmented using the method explained in the following subsection.

4.4.2. Support Vector Machine (SVM) Based Rule Optimization for Hemorrhage Segmentation

The utilization of pixel gray levels alone is not enough to determine whether a pixel is hemorrhage or not. Hence, there is a need for incorporation of other pixel information such as location, gradient etc. around the detected hemorrhage region to properly classify hemorrhage pixels from the non hemorrhage pixels. This incorporation must be adaptable depending on whether the hemorrhage pixel is in the neighborhood of all hemorrhage pixels or soft tissue pixels. This study incorporates pixel gray levels, distance of the pixel from the hemorrhage foci (the pixel with maximum gray level), the gray level variation within the selected window, and the magnitude of the gradient of each pixel within the selected window in order to achieve better segmentation.

4.4.2.1. Rule Generation

Let B_{opt} be the hemorrhage region image obtained using MI technique. Let T_{opt} be the boundary of the hemorrhage region in image B_{opt} and $p(x_i, y_j)$ be the hemorrhage pixel of T_{opt} . A window W of size $m \times m$ ($m < q$) is selected around pixel $p(x_i, y_j)$. There are three cases that need to be considered for an optimum segmentation: 1) the selected window W contains all hemorrhage pixels with gray levels within $[G_{opt}, G_{max}]$ 2) the majority of the pixels in W being hemorrhage pixels and with gray levels $\geq G_{opt}$, and 3) the majority of the pixels in W (being hemorrhage or soft tissue pixels) with gray levels $< G_{opt}$. Therefore, heuristic rules need to be generated for each case in order to optimally segment hemorrhage from non hemorrhage pixels. The rule for each case is given as follows.

Case 1: W containing all hemorrhage pixels with gray levels within $[G_{opt}, G_{max}]$.

If the window contains all pixels with gray levels within $[G_{opt}, G_{max}]$, then all these pixels are hemorrhage pixels and can be added to the hemorrhage region R . So the rule in this case is the pixel must satisfy the below condition in order to be added to region R .

$$R = \left\{ pixel : p(x_r, y_s) \mid G_{opt} \leq p(x_r, y_s) \leq G_{max} \right\} \quad (4.5)$$

Case 2: W containing a majority of hemorrhage pixels, i.e. more pixels with gray levels $\geq G_{opt}$.

If the window contains a majority of (i.e. $> 50\%$) hemorrhage pixels with gray levels $\geq G_{opt}$, then the probability of the rest of the pixels within the neighborhood being hemorrhage is high. As a result, the neighborhood will be dominant with hemorrhage pixels. As the

neighborhood is dominant with hemorrhage pixels, pixel gray level and the distance of the pixel from the foci are only incorporated into the rule in this case. These parameters are only considered because the variation in magnitude of the gradient and the variation between the pixel gray levels will not add any advantage in differentiating hemorrhage pixels from soft tissue pixels. Each of the parameters used will have a certain weightage which needs to be incorporated for determining hemorrhage pixels. Therefore the rule is if a pixel satisfies the condition given in 4.6, then it is considered as hemorrhage pixel and is added to region R .

$$R = \{pixel : p(x_r, y_s) | w_1 \times p(x_r, y_s) + w_2 \times D(x_r, y_s) + b > 0\} \quad (4.6)$$

where $D(x_r, y_s)$ is the distance between the pixel in the window and the foci (x_f, y_g) , and is given by:

$$D(x_r, y_s) = \sqrt{(x_f - x_r)^2 + (y_g - y_s)^2} \quad (4.7)$$

w_1 and w_2 are the weights and, b is the bias.

In order to achieve proper segmentation, these weights need to be optimized. A SVM based dual Lagrangian technique is used to determine the optimized weights and bias. This optimization technique is explained in the later subsections.

Case 3: W containing a majority of pixels (soft tissue or hemorrhage) with gray levels $< G_{opt}$.

If the window contains more (i.e. $>50\%$) pixels (soft tissue or hemorrhage) with gray levels $< G_{opt}$, then the probability of the rest of the pixels within the neighborhood being

hemorrhage is lower. Hence, it is required for the algorithm to be more restrictive in this case when compared to the other two cases. Hence, inclusion of magnitude of gradient and the gray level variation within the window along with the pixel gray level and its distance from the foci will help avoid over segmentation which is crucial. Therefore the rule associated with this case is:

$$R = \left\{ pixel : p(x_r, y_s) \left| w_3 \times p(x_r, y_s) + w_4 \times D(x_r, y_s) + w_5 \times V(x_r, y_s) + w_6 \times \left| \nabla f_{(x_r, y_s)} \right| + b_1 > 0 \right. \right\} \quad (4.8)$$

where,

$$V(x_r, y_s) = p(x_b, y_b) - p(x_r, y_s) \quad (4.9)$$

where $p(x_b, y_b)$ is the gray level of the center coordinate of window W , $V(x_r, y_s)$ is the difference in gray level of the center coordinate and the gray level of the pixel in the window. The magnitude of the gradient of each pixel is given in equation 4.10.

$$\left| \nabla f_{(x_r, y_s)} \right| = \sqrt{\left(\frac{\partial f}{\partial x_r} \right)^2 + \left(\frac{\partial f}{\partial y_s} \right)^2} \quad (4.10)$$

If a pixel in the selected window satisfies the above condition, then it is considered as hemorrhage and is added to the existing hemorrhage region R .

The weightage of the parameters given in equation 4.8 must be determined for each image as these can vary among different images. The weights w_3 through w_6 and the bias b_1 are later optimized using SVM based dual Lagrangian optimization technique.

4.4.2.2. SVM Based Rule Optimization

The weights used in the previously described rules must be optimized to ensure proper segmentation. These weights must be optimized for each image as these can vary from image to image within the same patient. A SVM based Lagrangian function in the dual space is used to optimize the weights and the bias. The optimization is solved by the saddle point of Lagrange function in the dual space. For optimization, the data for soft tissue pixels is selected outside the boundary T_{opt} , and the data for hemorrhage pixels is selected from the pixels within the boundary. The selection of these pixels outside the boundary and within the boundary will facilitate the process of identifying the gray level of the boundary pixels. A ten-fold cross validation is used for training and testing the data in order to determine the optimum weights and bias for each of the parameters used in the study. The size of the data set for training and testing depends on the size of the boundary of the hemorrhage in each image. The weights and the bias are optimized separately for each case. For solving with the Lagrangian in dual space, Karush-Kuhn Tucker conditions for the optimum of a constraint function are considered in the study [85].

With those conditions, the dual Lagrangian is given as follows in equation 4.11.

$$L_d(a) = \sum_{i=1}^n a_i - \frac{1}{2} \sum_{i,j=1}^n y_i y_j a_i a_j x_i x_j \quad (4.11)$$

where, a_i are the Lagrange multipliers, and x and y are the inputs and the labels and n is the dimensionality of the input.

The inputs in this study are pixel gray level, distance of pixel from the foci, magnitude of the gradient, and the gray level variation. If it is case 2, there are only 2 input variables. The labels are the classes: hemorrhage and non hemorrhage. This standard quadratic optimization problem is expressed in matrix notation and formulated as follows:

$$\begin{array}{ll} \text{Maximize} & L_d(a) = -0.5a^T H a - 1^T a, \\ \text{subject to} & y^T a = 0 \\ & 0 \leq a \leq C \end{array}$$

where, H is the Hessian matrix ($H_{ij}=y_i y_j x_i x_j$), C is the penalty parameter, and 1 is a unit vector $1 = [1 \ 1 \ \dots \ 1]^T$. C is chosen as the upper bound of α because with C the influence of training data points that remain on the ‘wrong’ side of a separating nonlinear hypersurface is limited. Also, the width of the soft margin is controlled by a corresponding C . Large C leads to small number of misclassification, smaller margin and vice versa. In our study, C is considered to be greater than zero and less than infinity for feasibility. The penalty parameter is optimized using 10 fold cross validation technique. Solution α_0 from the above equation determines the parameters of the optimal hyperplane w_0 and b_0 as given in equations 4.12 and 4.13.

$$w_0 = \sum_{i=1}^{N_{sv}} a_{0i} y_i x_i \quad (4.12)$$

$$b_0 = \frac{1}{N_{fsv}} \left(\sum_{s=1}^{N_{fsv}} \left(\frac{1}{y_s} - x_s^T w_0 \right) \right) \quad (4.13)$$

where,

w_0 and b_0 are the optimized weights and bias.

N_{sv} denotes the number of support vectors,

N_{fsv} denotes the number of free support vectors

In the equations 4.12 and 4.13, the support vectors are only used because the Lagrange multipliers are zero for non support vectors. Finally, with the optimal weights and bias, the decision hyperplane $d(x)$ is determined using equation 4.14.

$$d(x) = \sum_{i=1}^n w_{oi}x + b_0 \quad (4.14)$$

where,

x is the test data

The output of the test data is determined by using an indicator function given in equation 4.15.

$$i_F = \text{sign}(d(x)) \quad (4.15)$$

The number of wrongly classified pixels are determined by comparing the test output with the desired output. The obtained optimized weights and bias are used to determine if a pixel is a hemorrhage pixel or not. The optimized weights are used in the rules and the pixels in each window W are considered as hemorrhage if they satisfy the optimized rules. However, there is a slight chance of missing the hemorrhage pixels which are outside the boundary and are not located in the selected window. Hence, it is required to include these pixels in the hemorrhage region. Region growing process is used to grow the region around the already determined hemorrhage region R to determine any hemorrhage pixels that are missed during the optimization process. This is described in the following subsection.

4.4.3. Region Growing

The region growing process is the final phase of hemorrhage segmentation. This process is used to determine any missed hemorrhage pixels that are located outside the boundary of R . Figure 4.2 shows the region growing process used in this study. The region growing process consists of several steps. First, the boundary of the segmented hemorrhage R from the previous phase is used to select a window of size $m \times m$ around each boundary pixel. If the percent of total number of pixels within that window that satisfy the conditions described earlier are $\geq \eta$, the pixel factor, then the threshold t_1 for the window is determined using equation 4.16.

$$t_1 = me_1 + std_1 \quad (4.16)$$

where me_1 and std_1 are the mean and standard deviation of the gray levels of all the non background pixels in the window and are given by equations 4.17 and 4.18.

$$me_1 = \frac{\sum_{x=1}^m \sum_{y=1}^m f(x, y)}{m \times m - Card(S)} \quad (4.17)$$

$$std_1 = \sqrt{\frac{\sum_{x=1}^m \sum_{y=1}^m (f(x, y) - m_1)^2}{m \times m - Card(S)}} \quad (4.18)$$

where, $S = \{(x, y) | f(x, y) = 0\}$ is the set of pixels located in the background having zero gray level. $Card(S)$ denotes the cardinality of set S .

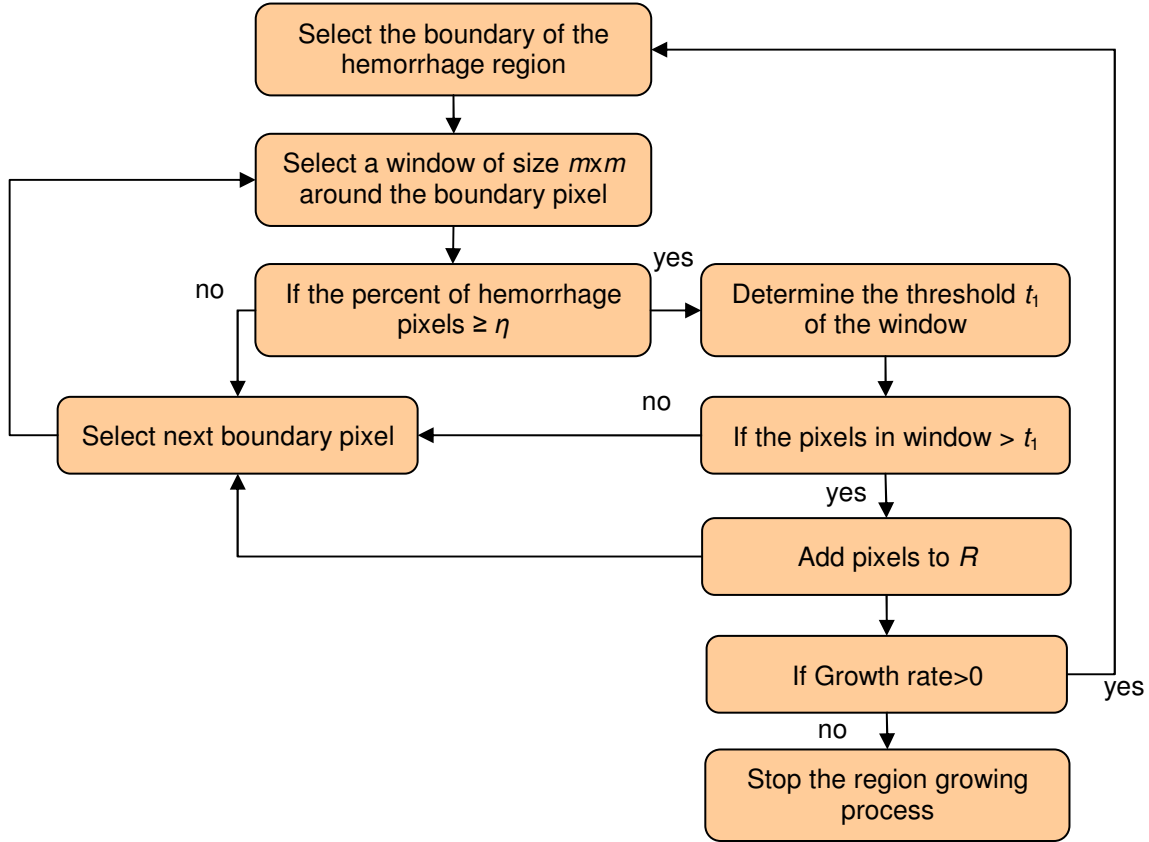


Figure 4. 2. Region growing process

If any of the pixels that lie outside the boundary and within the window satisfy t_1 , then they are considered as hemorrhage pixels and are added to the existing hemorrhage region R . This entire region growing process is repeated for all the boundary pixels. This complete process constitutes one epoch. If the growth rate of hemorrhage region is >0 in the current epoch, then the entire process is repeated starting from selecting the boundary of the hemorrhage region. If the growth rate is zero, the region growing process is stopped. The growth rate in each epoch is calculated using equation 4.19.

$$Growth\ rate = \frac{E_c - E_p}{E_c} \times 100 \quad (4.19)$$

where, E_c is the total area of the hemorrhage by the end of current epoch, and E_p is the total area of the hemorrhage by the end of previous epoch. The total region grown by the end of the region growing process is considered as the final segmented hemorrhage.

4.5. Evaluation Measure for Segmentation

Once the hemorrhage is segmented, a suitable measure is required to quantify the accuracy of segmentation. This study utilizes a measure called mis-segmented area. The mis-segmented area measure represents the uncommon area of segmented region (i.e. the pixels of segmented region that are not a true hemorrhage) compared to the gold standard area of segmented hemorrhage. If A_1 and A_2 are the areas of actual and the segmented region, respectively, the mis-segmented area of the two regions is defined as

$$\frac{\text{Cardinality}\{K\}}{\text{Cardinality}\{A_1\}} \times 100 \quad (4.20)$$

where:

$$K = \{pixels : p | p \in A_1 \cup A_2, p \notin A_1 \cap A_2\}$$

Based on this measure, the segmented hemorrhage will be classified into three categories: good, acceptable and unacceptable through consultation with a trauma physician and a radiologist, who identified actual hemorrhage contour as the ground truth.

The segmented regions with mis-segmented area $<10\%$ will be classified as good, and regions with mis-segmented area between 10% and 20% will be considered as acceptable, and finally any region with mis-segmented area greater than 20% will be considered as unacceptable. These ranges for good, acceptable and unacceptable are used in the study

based on the discussion with expert radiologists who utilize these ranges to determine if a region is properly segmented or not and to measure the severity of the bleeding.

4.6. Quantitative Measurement

In order to assess the bleeding severity and the risk of death, it is important to quantify hemorrhage location, number of bleeding foci, and hemorrhage volume from the segmented hemorrhage region.

4.6.1. Hemorrhage Location Identification

Once the hemorrhage is detected, depending on the location of bone and arteries, the location of hemorrhage is determined. This location measurement is registered using a set of identifiers which include: left side of the body, right side of the body, in/not in the surrounding area of the bone.

4.6.2. Bleeding Foci

Along with the hemorrhage location, the bleeding severity is also estimated based on the number of bleeding foci in the image. In general, if the injury is severe, there is a higher chance of multiple bone fractures which leads to multiple bleeding sites. The number of detected regions with hemorrhage in a single image is the number of bleeding foci in that image.

4.6.3. Hemorrhage Volume Measurement

The volume of segmented hemorrhage from each patient is determined by viewing the images as a pyramid and considering the slices and their thickness (where hemorrhage is present) to approximate the height of the pyramid. The total area of the hemorrhage is the area of hemorrhage present in all the regions of the segmented slices.

CHAPTER 5 OUTCOME PREDICTION

5.1. Introduction

In the trauma care environment, the physicians have to process lot of information in a short period for accurate decision making and treatment planning. Therefore, there is an increased need in automated computer-aided decision making system. Such systems have to provide reliable recommendations that allow the caregiver to understand and monitor the reasoning behind the recommendations. The existing decision making systems are focused on having high false positives which might lead to loss of attention of medical staff attending the trauma patients. This can result in errors. Therefore, there is a need for not only an automated decision support system that can process all the patient information but also has the capability of generating relatively high specificity.

Machine learning methods such as neural networks and kernel based techniques etc. are known to suffer from the issue of over fitting when trained for applications with smaller number of examples. This chapter presents the outcome prediction using Boosted Logistic Model Tree (BLMT) in order to better classify the data and improve the specificity as well. Figure 5.1 shows the schematic diagram of the decision making process that is used to select features and predict the outcome.

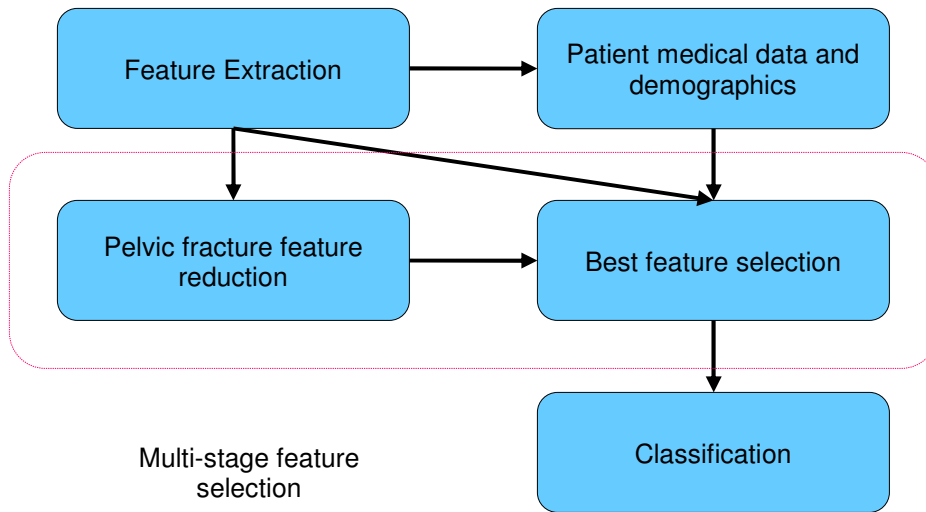


Figure 5. 1. Schematic diagram of the decision making system

5.2. Dataset

The dataset used in this study is provided by Carolinas Health System and Virginia Commonwealth University Medical Center. This data comprises of 49 pelvic trauma cases which is a relatively small number. Some of these cases were sent to Intensive Care Unit (ICU) and others with relatively less injuries were sent home or to a hospital ward. In all these cases, patients survived the injuries. Demographics and injury scores extracted from patient medical records include patient age, gender, Glasgow Coma Score (GCS), Injury Severity Score (ISS), etc.

5.3. Feature Extraction

Along with the patient medical records and demographics information, the hemorrhage features extracted from the pelvic CT images are also included in the decision making process. These hemorrhage features include presence of hemorrhage and volume of hemorrhage. The fracture features extracted from the companion project are also included in the decision making process. These features include the presence of fracture in ilium, ischium, sacrum, pubis, acetabulum, pubic symphysis width, vertical displacement of pubis, and pelvic ring symmetry displacement, total bone displacement and total number of fractures.

5.4. Multi-stage Feature Selection

The feature selection process in this study employs a multi-stage feature selection technique: first stage to reduce fracture features, and the second stage to select the final features for decision making.

5.4.1 Fracture Feature Reduction

There are several features associated with fracture alone as mentioned in previous subsection. All of these features may not be required to individually assess injury severity. The features, total bone displacement and total number of fractures might be good enough for the overall representation of fracture features during feature selection. In order to determine whether these features are good enough to represent the entire bone fracture information, Davies-Bouldin (DB) index is used to determine the best features among all

the fracture features including the total bone displacement and number of fractures. If these two features are better than majority of the fracture features, these will be included in the overall feature selection. DB index is a function based on the scatter within the cluster and the separability between the clusters. This measure has proved to be effective for many biomedical applications [86]. The DB index requires the computation of cluster to cluster similarity.

$$D_{ij} = \frac{(C_{ii} + C_{jj})}{C_{ij}} \quad (5.1)$$

where C_{ii} and C_{jj} are the dispersions of i^{th} and j^{th} clusters, and D_{ij} is the distance between their mean values and are given by:

$$\begin{aligned} C_{ii} &= \left[\frac{1}{K_i} \sum_{k=1}^{K_i} \|y_k - m_i\|^2 \right]^{1/2} \quad y_k \in \text{cluster } i \\ C_{ij} &= \|m_i - m_j\| \end{aligned} \quad (5.2)$$

where K_i is the number of members in cluster i ,

y_k is the k^{th} sample vector of cluster i , and m_i is the mean vector of the cluster i .

DB index is calculated by determining the worst case of separation for each cluster and averaging these values [86]. This is given in equation 5.3.

$$DB = \frac{1}{N} \sum_{i=1}^N \max_{i \neq j} D_{ij} \quad (5.3)$$

where, N is the total number of clusters. Two clusters are used in the study. The selected features are combined with the rest of the features such as hemorrhage and medical records in the following subsection to determine the predominant features required to generate a robust model.

5.4.2 Predominant Feature Selection using Symmetrical Uncertainty based Correlation Filter

In order to generate a robust model, it is important to select useful features. This study uses a Symmetrical Uncertainty (SU) based correlation filter to select the predominant features [87]. Figure 5.2 shows the algorithm used for predominant feature selection. If two features are redundant, the algorithm removes one feature that is less relevant to the class keeping more information to predict the class while reducing redundancy in the data. SU is measured using equation 5.4.

$$SU_{X,Y} = 2 \left[\frac{H(X) - H(X|Y)}{H(X) + H(Y)} \right] \quad (5.4)$$

where $H(X)$ is the entropy of variable X , and $H(X|Y)$ is the conditional entropy.

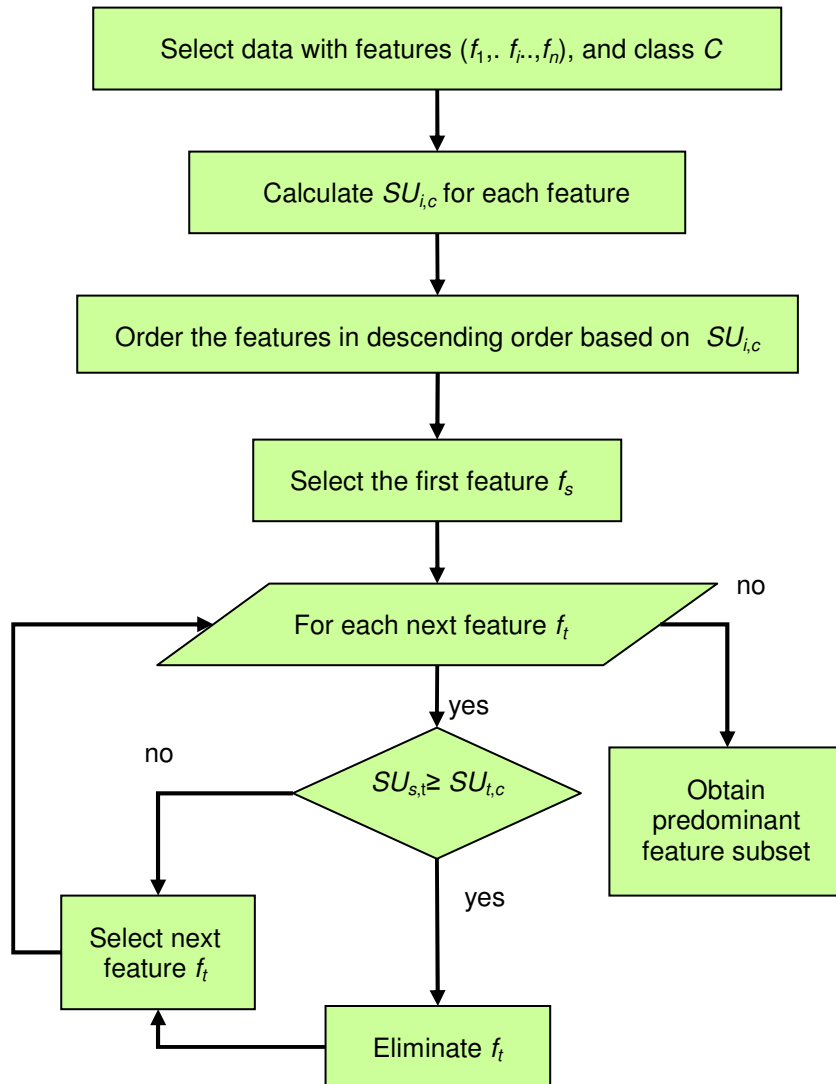


Figure 5. 2. Flowchart of feature selection using SU based correlation filter

The SU measure is used in the study because of its ability to not bias towards features with more values and its normalization capability. In addition, this measure still treats the pair of features symmetrically. This entropy based measure requires nominal features. However, they can be applied to measure correlations between continuous features as well.

Once the predominant features are selected, it is important to predict the outcome using the selected features.

5.5. Classification for Prediction Outcome

Among the different machine learning techniques, decision trees and decision rules are generally used for biomedical applications because of their interpretability. However, many machine learning techniques suffer from over fitting of data. In addition, many machine learning techniques employed for biomedical applications have higher sensitivity which is not always good. This study uses a Boosted Logistic Model Tree for the outcome prediction and to improve the specificity. Boosting is a method to improve model accuracy. In boosting, the models are fitted iteratively to the training data, using appropriate methods gradually to increase emphasis on observations modeled poorly by the existing collection of trees. This study uses Adaboost algorithm for boosting [88]. The main premise of this boosting is to maintain a distribution of weights over the training set. Logistic Model Tree (LMT) is used as the base classifier [89].

A logistic model tree consists of a standard decision tree structure with logistic regression functions at the leaves. The leaf node has two child nodes that are branched left and right based on a certain threshold. The threshold is usually fixed by LogitBoost method. LogitBoost uses an ensemble of functions F_K to predict classes $1, \dots, K$ using M weak learners.

$$F_k(x) = \sum_{m=1}^K f_{mk}(x) \quad (5.5)$$

The LMT classifier is built in the following manner. First, LogitBoost is run on all data to build a logistic regression model for the root node. The number of iterations is determined by tenfold cross validation. Secondly, the data is split at the root node using C4.5 splitting criteria. The logistic regression models are then built at the child nodes using LogitBoost. As long as there are at least 15 instances present at a node and a useful split is found, the splitting and model building is continued. Finally, the Classification and Regression Tree (CART) cross validation based pruning algorithm is applied to the tree. These trees are used as they are considered robust and are not prone to over fitting. In addition, these trees provide explicit class probability estimates rather than just a classification.

CHAPTER 6 Abdominal Organ Segmentation

6.1. Introduction

Abdominal trauma is the third leading cause of traumatic deaths resulting in a mortality rate of approximately 7-15% [90] – [92]. Abdominal trauma is classified either as blunt abdominal trauma or penetrating abdominal trauma. Blunt trauma usually results from motor vehicle collisions, assaults, falls, etc. The most commonly injured organs in blunt trauma are spleen, liver, retroperitoneum, small bowel, kidneys, bladder, colorectum, diaphragm, and pancreas [90], [92]. Penetrating trauma typically involves the infringement of the abdominal cavity by a gunshot wound or stab wound [91], [94].

Of all the organs in the abdomen region, spleen is one of the most commonly injured organ in blunt abdominal trauma. Splenic injury most commonly occurs due to motor vehicle collisions. However, it can also result from falls, sport-related activities, assault, etc. Penetrating splenic trauma is less common than blunt injury. This chapter describes the methodology used to segment the spleen.

The spleen is the largest of the ductless glands situated in the left hypochondriac region with its superior extremity extending into the epigastric region. It lies between the fundus of the stomach and the diaphragm. Figure 6.1 shows the spleen in the abdomen region.

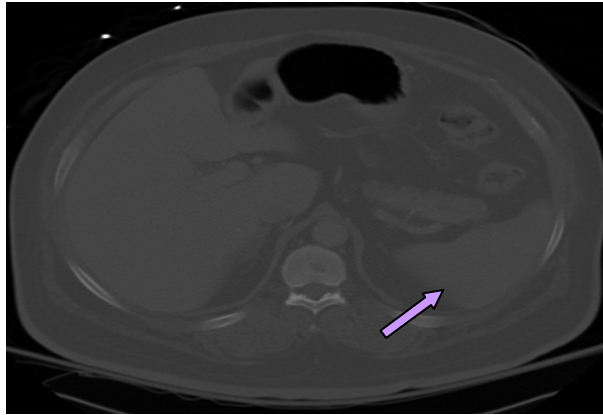


Figure 6. 1. Spleen (arrow points to the spleen) in Abdominal CT Image

6.2. Spleen Segmentation

The process of spleen segmentation involves series of steps: preprocessing of abdominal CT images, contrast enhancement, bright objects mask formation, bright objects segmentation and masking, spleen detection and segmentation. Figure 6.2 shows the overall process of spleen segmentation.

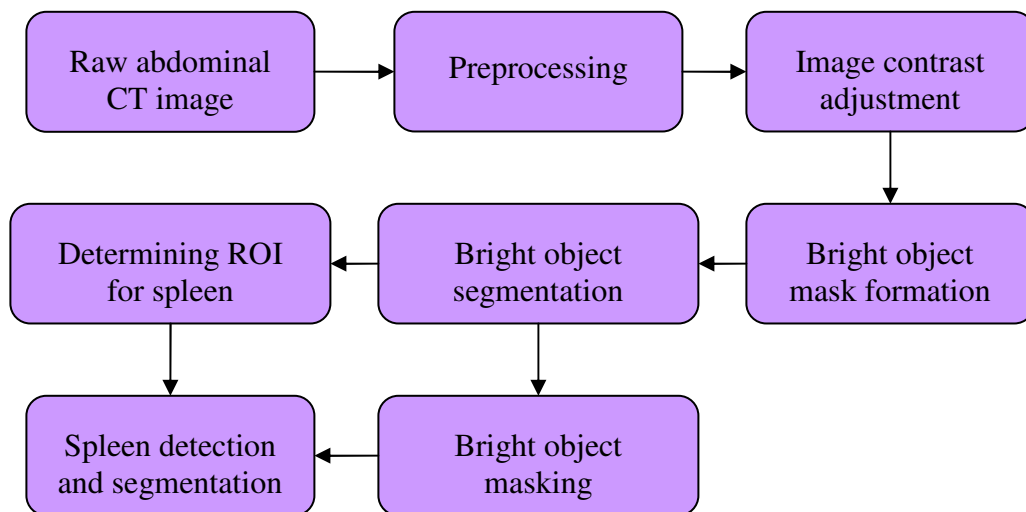


Figure 6. 2. Overall process of spleen segmentation

6.2.1 Preprocessing

The first step of spleen segmentation is preprocessing. Abdominal CT images consist of several artifacts such as cables, hands, CT table, etc. These artifacts must be removed from the images in order to minimize the influence of these artifacts on the gray level statistics and reduce the complications that might develop in the future stages of the algorithm. The spleen preprocessing in the abdominal CT image is carried out in the same manner as that of pelvic CT preprocessing described in section 2.3 of chapter 2.

6.2.2 Histogram based Image Contrast Enhancement

The abdominal CT image consists of tissues with different gray levels. Some of the soft tissues lie partly within the same gray level range. It is sometimes challenging to differentiate these tissues from one another. Contrast enhancement will ease the task of abdominal organ detection. In general, the gray levels of blood vessels and bones are greater than the other tissues such as liver, spleen, etc. In this step, this study focuses on the contrast enhancement of the spleen. This contrast enhancement is achieved by mapping the gray levels in the image to new gray levels through gray level transform. The mapping function reassigns the current gray level to a new gray level. This is achieved in the following manner.

First, the histogram of a given image is determined. Then the gray level g_{min} that occurs maximum number of times among the non background pixels in the image is determined. Then the gray level g_{max} greater than the g_{min} that occurs maximum number of times is

determined. Since this part of the study is focused on the solid organs, considering these values will enhance the visibility of these organs through stretching.

Second, a new gray level range $[g'_{min}, g'_{max}]$ is defined to map the gray levels of the image. This mapping is achieved using linear transform given in equation 6.1.

$$f'(x, y) = \begin{cases} 0 & f(x, y) < g_{min} \\ \frac{g'_{max} - g'_{min}}{g_{max} - g_{min}} [f(x, y) - g_{min}] + g'_{min} & g_{min} \leq f(x, y) \leq g_{max} \\ g'_{max} & f(x, y) > g_{max} \end{cases} \quad (6.1)$$

where, $f'(x, y)$ is the new gray level of a pixel and $f(x, y)$ is the old gray level of a pixel in the image.

The pixels with gray levels that lie below g_{min} are of no interest as these pixels are typically peritoneal cavity, muscles etc. The pixels with and above g_{max} are mapped to new gray level g'_{max} as these pixels are typically blood vessels, bones, etc. Mapping these regions to new maximum gray level will facilitate the bright objects and spleen segmentation process. This linear transform for contrast enhancement spreads the gray level values evenly over the full contrast range. The obtained image is the contrast enhanced image.

6.2.3 Bright Objects Mask Formation and Edge Detection

The next step in the spleen segmentation process is to form bright objects mask. The term “bright objects” refer to bone, blood vessels, contrast enhanced stomach, etc. Presence of all these objects in the image will influence the gray level statistics in the

segmentation process. Hence a mask is formed on all the bright objects in the contrast enhanced image in the same manner as the method described in section 2.4 of chapter 2. Morphological operations are then performed on the obtained mask to eliminate unwanted objects from the mask that might affect locating the spleen in the later stages. The obtained mask with unwanted objects removed is the bright objects mask. The edges of the objects in the mask are then determined using Canny edge detection technique. This technique is used because of its capability to detect true strong and weak edges. These edges are later used to grow seeds in order to determine any missed bright object pixels. This is described in the following sections.

6.2.4 Seed Growing and Bright Objects Segmentation

The neighborhood of the detected edges of these bright objects may also be part of the bright objects such as spinal bone, ribs, etc. Hence, there is a need to identify these regions for proper segmentation. The detected edges are now used as seeds to determine the bright object pixels. These pixels are determined using a region growing technique. The region growing technique is accomplished in the same manner as described in section 2.5.1 of chapter 2. The obtained image after region growing is the bright object segmented image. The segmented bright objects are later masked in the contrast enhanced image by setting their pixel gray levels to zero.

6.2.5. Knowledge based Spleen ROI Detection

The spleen is located in the left upper quadrant of the abdomen. Its upper pole is near the lower ribs. Based on this knowledge and the knowledge of bones (vertebrae) location, the ROI is determined in the following manner: First, the width and height of the abdomen region is determined. Based on these measurements, the abdomen region is divided into six sections, three rows and two columns. The first and the last row height are the same. This height is the distance between the lower most tip of the vertebrae and the lower most tip of the abdomen. Rest of the region is the second row. The two columns are obtained based on the centroid of the vertebrae. The abdomen region that lies in the second row and second column is considered as ROI.

6.2.6. Spleen Detection

Once the ROI is determined, the next step is to detect the spleen. The contrast enhanced image in which the bright objects have been masked is used in this stage. This spleen detection process in all the images of a patient is carried in 2 stages: detecting spleen in the first image, and then detecting the spleen in the following images.

6.2.6.1. Spleen Detection in the First Image

In this study, the spleen location in the first image is determined based on the location of the ribs and vertebrae located in the ROI. The proposed spleen detection process consists of the following steps and are performed on the preprocessed image in which the bright objects have been masked and the contrast enhanced:

Step 1: The threshold th_1 is determined. This is calculated using equation 6.2.

$$th_1 = m_1 + s_1 \quad (6.2)$$

where m_1 and s_1 are the mean and standard deviation of the gray levels of all the non background pixels.

Step 2: The objects in the ROI whose gray levels are greater than the above mentioned threshold are determined.

Step 3: Morphologic operations are then applied to eliminate any isolated pixels that met the threshold criteria.

Step 4: The ribs that lie within ROI are identified and their statistical properties are determined.

Step 5: The statistical properties of the objects obtained in step 3 are determined. The total distance D_i between the centroid of each object to all the ribs located in ROI is calculated using equation 6.3.

$$D_i = \sum_{k=1}^m \left(\sqrt{(rx_{ck} - x_{ci})^2 + (ry_{ck} - y_{ci})^2} \right), \quad i = 1, 2, \dots, n \quad (6.3)$$

where, (rx_{ck}, ry_{ck}) is the centroid of rib k , and (x_{ci}, y_{ci}) is the centroid of object i .

Step 6: The object whose centroid is at a minimum distance to the ribs is determined. This object is considered as the spleen and its pixel coordinates are determined.

6.2.6.2. Spleen Detection in the Subsequent Images

The spleen centroid from the first image is considered as the initial spleen centroid location for the second image. This process consists of the following steps:

Step 1: Steps 1 through 3 are repeated in the same manner as given in section 6.2.6.1.

Step 2: The statistical properties of all the objects that satisfy the threshold are determined. Each of the object's pixel coordinates are compared to the pixel coordinates of the detected spleen in the previous image.

Step 3: The object in the current ROI with maximum number of matched coordinates is considered to be the spleen in the current image. This spleen pixel coordinates are used for comparison with the following image's objects' pixel coordinates.

This process is repeated in the same manner for the following images to detect the spleen.

6.2.7. Spleen Segmentation

The ultimate goal of spleen segmentation is to detect laceration and active hemorrhage. The spleen detected using the previous approach may sometimes detect spleen partially. This might be because of the presence of severe laceration or active hemorrhage whose gray levels are lower than the threshold set for detecting the spleen in the previous section.

In order to accomplish proper spleen and hemorrhage detection, it is important to segment the entire spleen region. This study utilizes edge merging technique. As hemorrhage or laceration may not be present in all the images in a patient, edge merging will facilitate the process of segmenting in the entire hemorrhage area of the spleen. The edge of the spleen in the current image is determined using Canny edge detection. Since

each CT slice is a few millimeters thick, incorporation of spleen information from the previous and the subsequent slices will help connect the missing edges and the disconnected edges of the spleen in the current image. Therefore to ensure, better segmentation of the spleen, the edges in the spleen of the current image are merged with the respective edges of the spleen in the previous and the subsequent image.

Once the edges are merged, the maximum gray level of the detected spleen in each image is determined. The mean of these maximum values GL_{\max} is calculated. This is calculated in order to restrict the spleen region during segmentation process.

Once the edges are merged, the entire merged region is considered as the new ROI S . It is called as new ROI because all the pixels in the entire merged region may not be the spleen pixels. Hence, the pixels in the new ROI are considered as spleen pixels if they satisfy the below condition.

$$Spleen = \{(x, y) \mid S_{mean} \leq S(x, y) \leq GL_{\max}\} \quad (6.4)$$

where, S_{mean} is the mean gray level of non background pixels in S . The mean and the maximum value are chosen in the above condition because, including the mean will include the hemorrhage pixels as well. The maximum value chosen will restrict the non spleen pixels being considered as spleen pixels.

6.3. Evaluation measure for spleen segmentation

The accuracy of segmentation must be determined in order to determine the performance of the proposed method. The accuracy of segmentation is measured by

determining the mis-segmented area. The mis-segmented area represents the uncommon area of segmented region (i.e. the pixels of segmented region that are not a true hemorrhage) compared to the gold standard area of segmented hemorrhage. This process is carried out in the same manner as that used to evaluate the pelvic hemorrhage segmentation accuracy described in section 4.5 of chapter 4.

CHAPTER 7 RESULTS AND DISCUSSION – PELVIC TRAUMA

7.1. Introduction

Chapters 2-4 described the methodologies used for hemorrhage detection and segmentation in traumatic pelvic injuries. Chapter 5 presented the methodology used to predict the outcome from the features extracted from the medical images and patient medical records and demographics. The results obtained using all these methodologies are given in this chapter starting from preprocessing to outcome prediction. The results presented in this chapter are the results obtained from CT images of different patients. The collection of data from different patients allow for the better assessment and evaluation of the methods' performance when dealing with bone variations among different patients.

7.2. Dataset

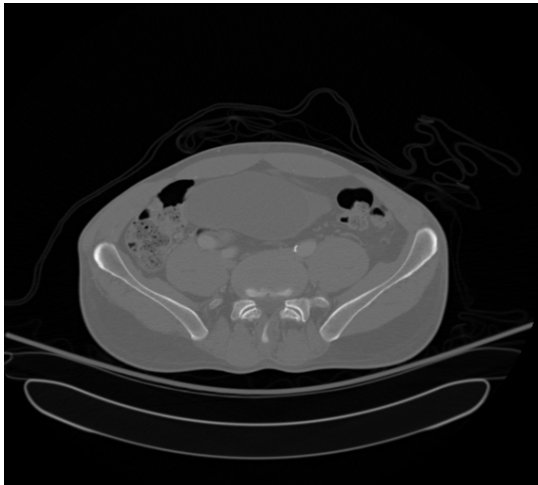
The data is obtained from North Carolinas Health System and Virginia Commonwealth University Medical Center. The data is collected from 11 pelvic trauma patients. Thirty eight to 221 images are used from each patient. The images used in this project are axial dicom CT images with various slice thicknesses of 1 mm, 2 mm, and 5 mm. A total of 943 images are used for this study.

7.3. Preprocessing and Initial Bone Segmentation Results

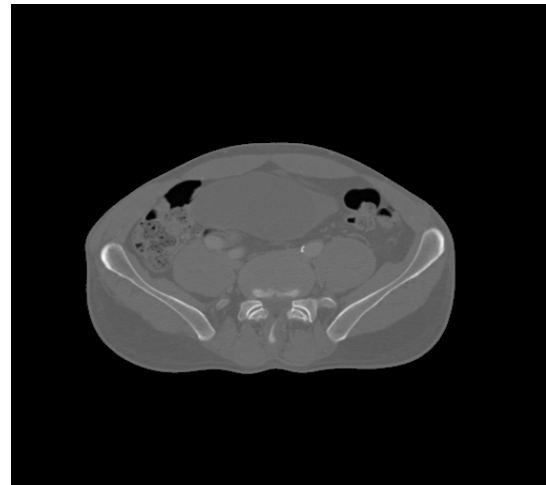
This section provides the sample results for artifact removal, initial bone mask formation, edge detection, initial bone segmentation and best template detection.

7.3.1. Artifact Removal

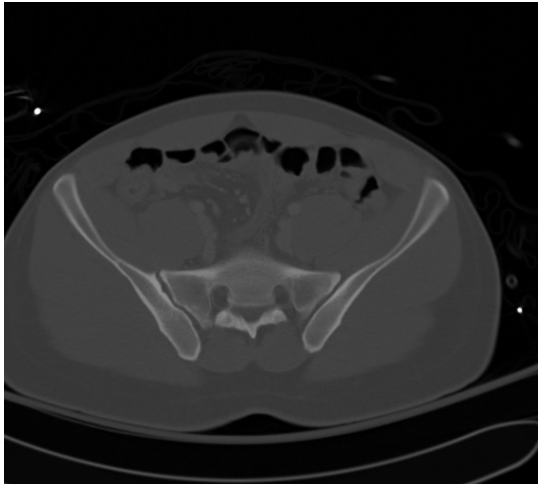
Figure 7.1 show the results from the removal of artifacts and the extracted pelvic region. This step is very important because, if present, artifact gray levels can influence the gray level statistics and create complications in the later stages. Figure 7.1 (a) shows a raw CT image. This image includes CT table. Figure 7.1 (b) shows the pelvic region extracted including the removal of the CT table. In some cases, upper part of the CT table is extracted along with the pelvic region. This is because the upper part of the CT table is attached to the pelvic region. This can be seen in figure 7.1 (c) and (d).



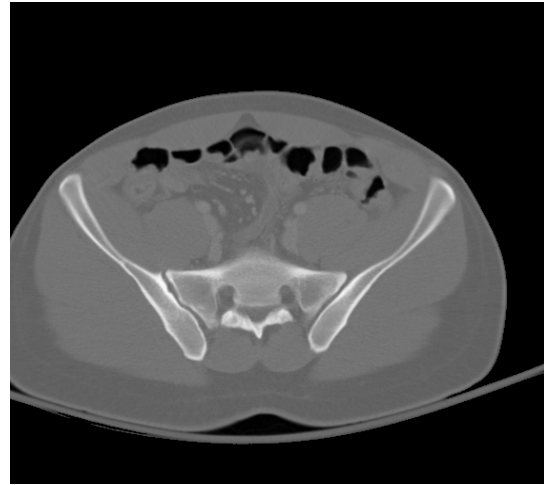
(a) Raw CT image example A



(b) Artifact removal example A



(c) Raw CT image example B

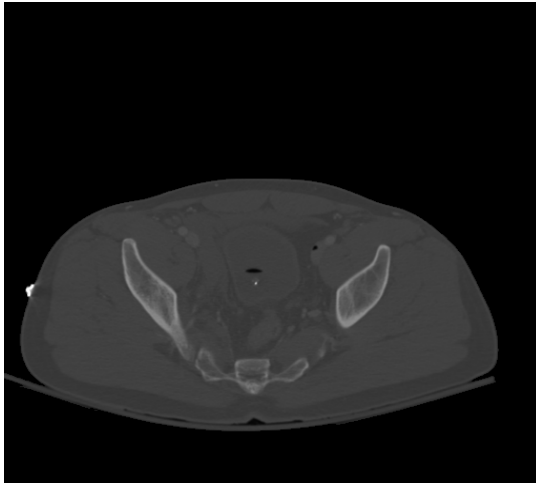


(d) Artifact removal example B

Figure 7. 1. Sample results for artifacts removal

7.3.2. Initial Bone Mask Formation

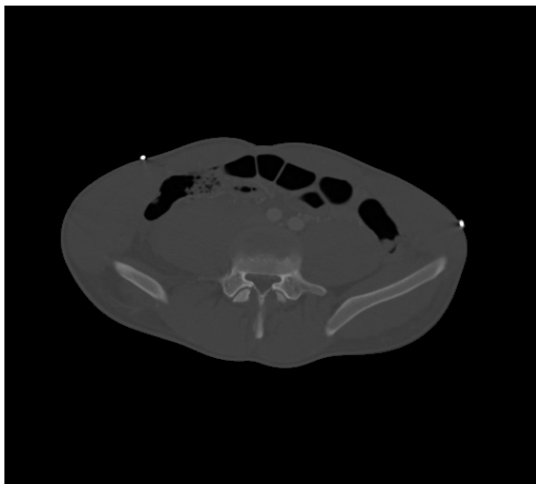
Figure 7.2 shows the results for initial bone mask formation. These results are obtained using a threshold based method combined with image filtering. Threshold method was preferred here due to the ease in implementation, low computational complexity and quality of the results. However, the connectivity of bone regions need improvement and some of the edges are weak. It can also be observed in the figure 7.2 (b) that other object is also included in the image. This is because the range of gray level for bone overlaps with that of the artifact in the image. Figure 7.2 (d) does not contain any non bone objects in the obtained initial mask. However, complete bone region is not obtained. This is because of the faded bone edges. The next steps of the algorithm address these issues.



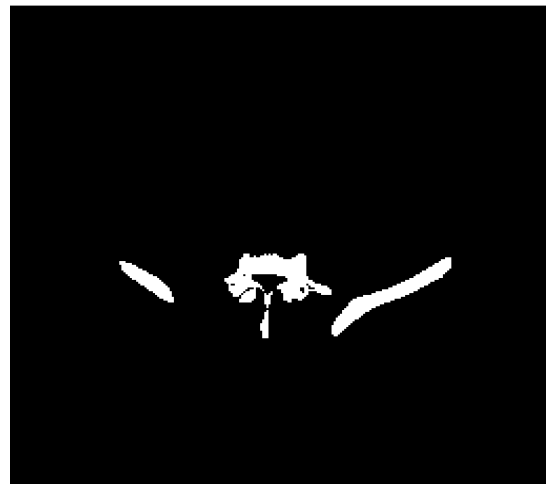
(a) Extracted pelvic region example A



(b) Initial bone mask example A



(c) Extracted pelvic region example B



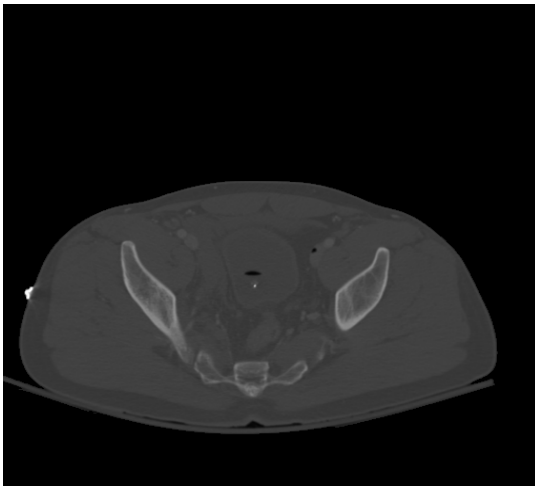
(d) Initial bone mask example B

Figure 7. 2. Sample results for initial bone mask formation

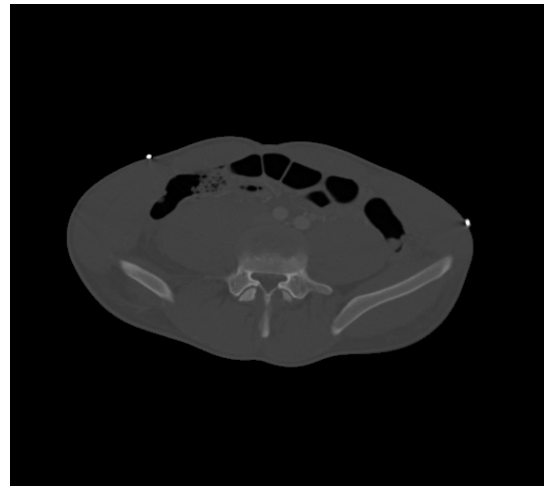
7.3.3. Edge Detection and Seed Growing

In this part of the algorithm, noise in the images is removed using 2D Gaussian filter. The result of image filtering is shown in figure 7.3 (c) and (d). The Gaussian filtering removes the speckle noise present in the image and the image appears smooth. The edges

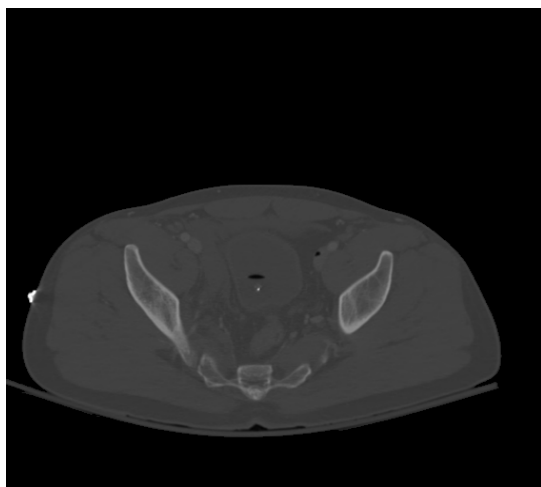
detected from the intermediary bone mask can be seen in figure 7.3(e) and (f). In figure 7.3 (e), it can be observed that edges of the non bone object is also detected along with the bone. The seed growing can be observed in figures 7.3 (g) and (h). This seed growing process improves the connectivity of bone edges. The region growing process only allows for adding seeds located inside the region delineated by the edge seeds. This prevents the process from spreading to the non bone regions. In figure 7.3 (g), it can be observed that the edge detected image still contains non bone object as part of the bone image. However, in figure 7.3 (h), the edge image does not contain any non bone regions. This is because of the variation in gray levels.



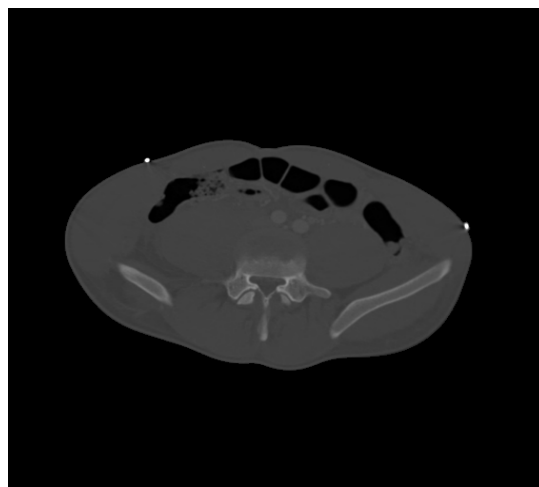
(a) Extracted pelvic image example A



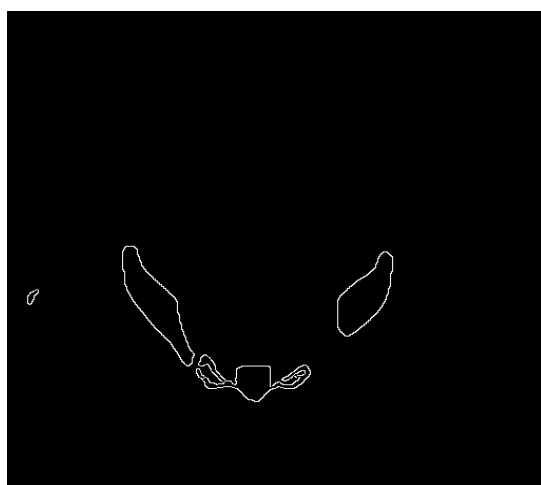
(b) Extracted pelvic image example B



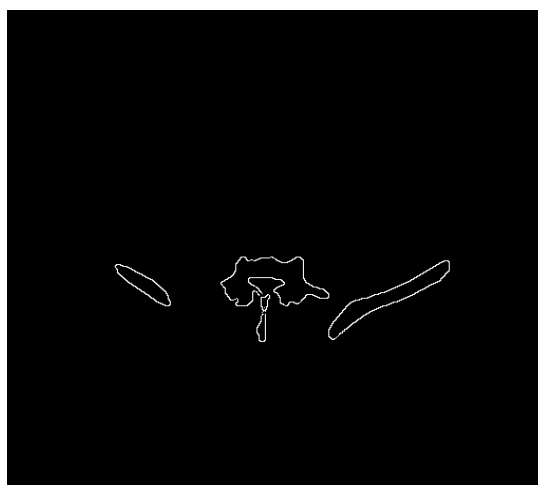
(c) Gaussian filtered image example A



(d) Gaussian filtered image example B



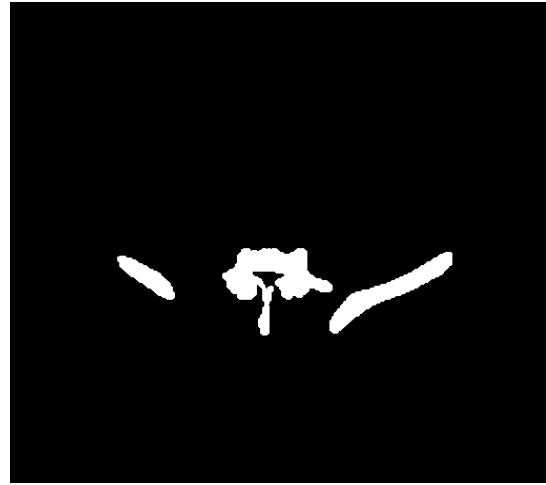
(e) Detected edge image example A



(f) Detected edge image example B



(g) Initial segmented image example A

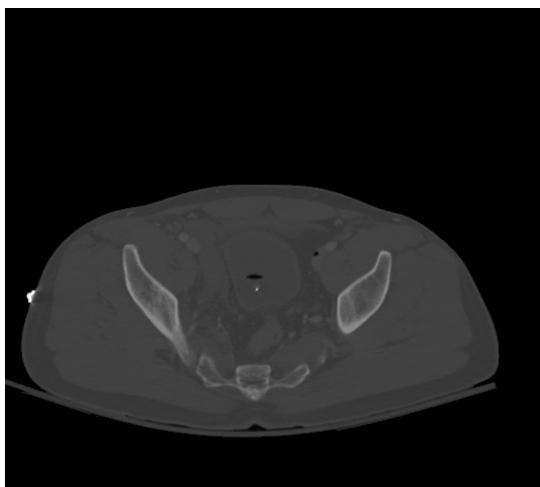


(h) Initial segmented image example B

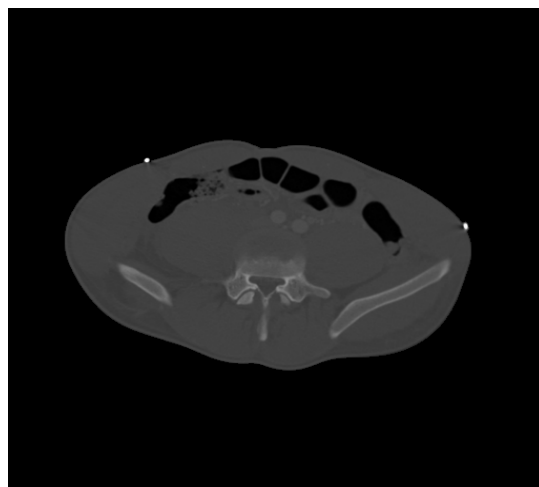
Figure 7. 3. Sample results for edge detection and initial bone segmentation

7.4. Best Template Detection and Object Recognition

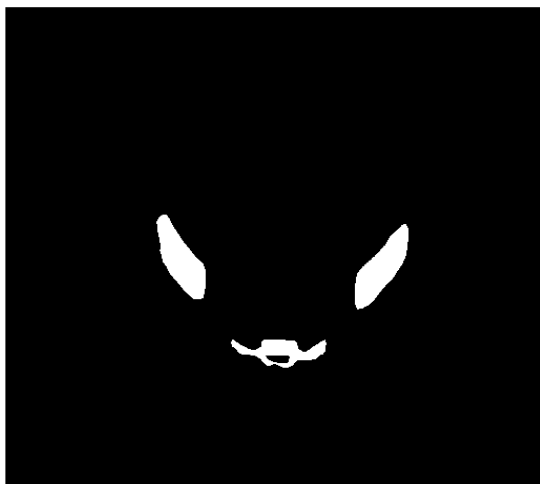
From the above results in figure 7.3, it can be observed that the initial segmented bone image contain non bone object such as artifact along with the bones. To ensure proper bone segmentation, this non bone object must be removed. Therefore, shape matching technique is used here to eliminate this non bone object. Figures 7.4 (c) and (d) show the best matched template obtained for a given extracted pelvic image. Selection of a template with minimum matching cost proves to be a simple and efficient technique. The non bone object is removed from the image through sequential elimination based on the shape matching method. This method is able to successfully identify the regions that do not match the template and successfully eliminates the majority of objects that do not match the template.



(a) Original image example A



(b) Original image example B



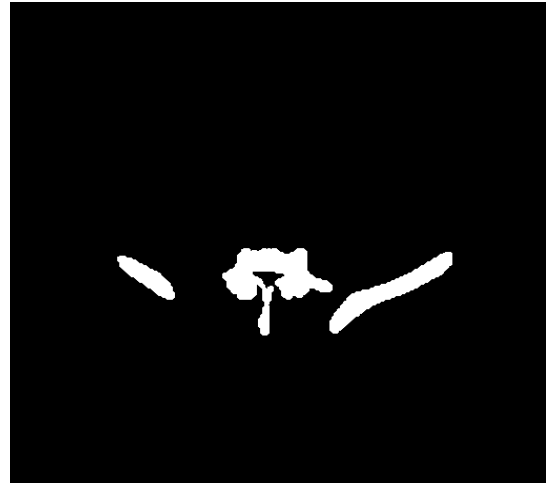
(c) Best matched template example A



(d) Best matched template example B



(e) Desired initial segmentation example A



(f) Desired initial segmentation example B

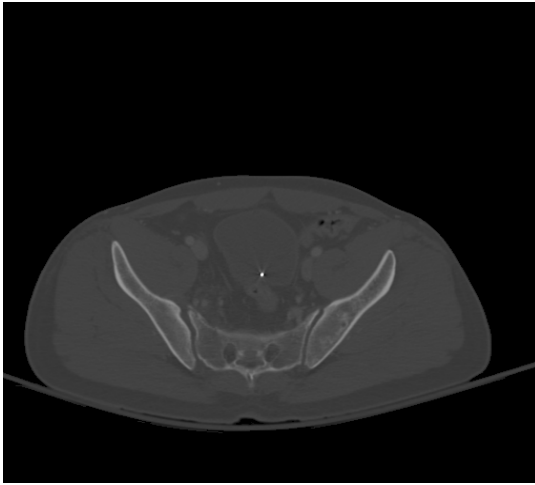
Figure 7. 4. Sample results for best template matching and elimination of non bone objects

7.5. Final Bone Segmentation and Artery Detection Results

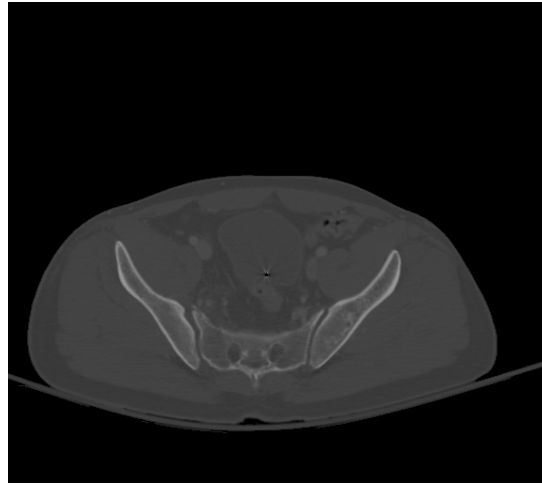
This section presents the results for methods described in chapter 3. These results include catheter masking, edge merging, final bone segmentation, and artery detection.

7.5.1. Catheter Masking

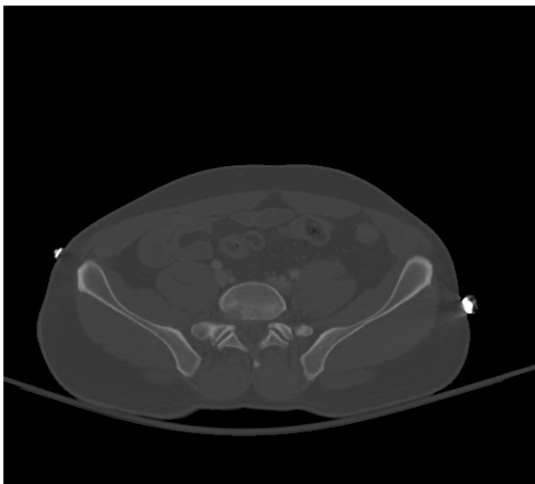
Catheter is a tube inserted into the body cavity for instillation of contrast during CT scan. This object in the CT image usually has a gray level similar or higher than bone gray levels. Catheter masking is required in order to minimize the effect of gray level values on the overall gray level values of the objects in the image. Figure 7.5 shows the masking of catheter and other objects whose gray levels are brighter than bone.



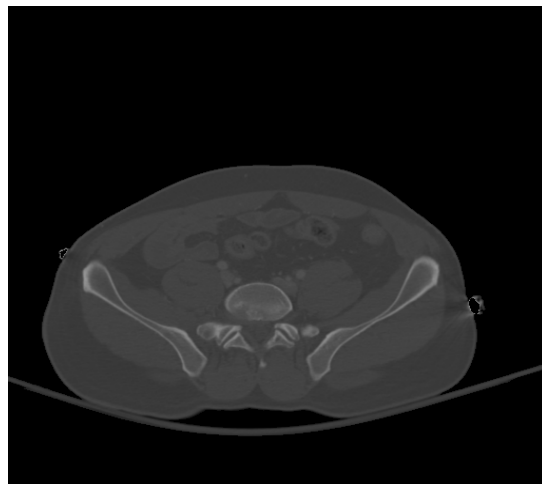
(a) Original image example A



(b) Catheter masked image example A



(c) Original image example B



(d) Artifacts masked image example B

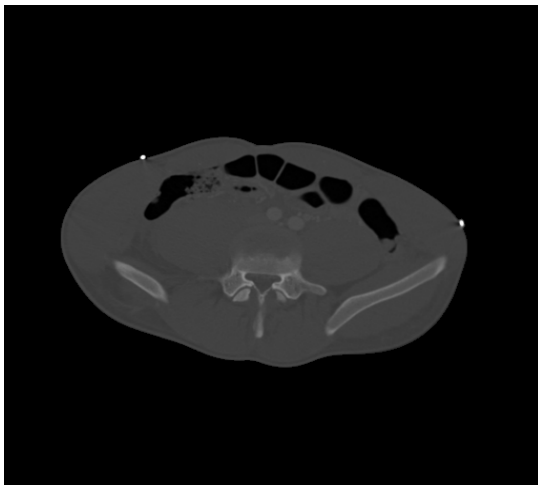
Figure 7. 5. Sample results for catheter and bright objects masking

The method used here not only masks the catheter but also masks other objects whose gray levels are higher than bone such as any leftover artifacts extracted along with the pelvic region. This can be seen in figure 7.5 (d). It is to be observed that catheter is not always visible on the CT images. Even if visible, its gray levels may not always be greater than the gray levels of the bone. In those cases, catheter's gray levels are similar to the

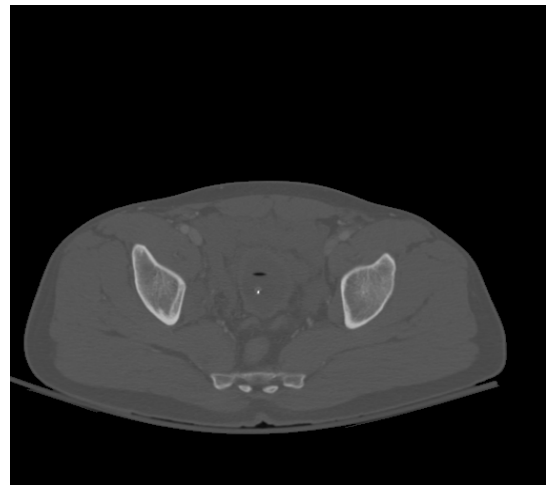
gray levels of the bone. The method for catheter masking only masks the catheters whose gray levels are higher than the bone average gray levels. For the rest of the cases, the catheters are masked during the unwanted objects filtration stage.

7.5.2. Edge Merging and Bone Segmentation

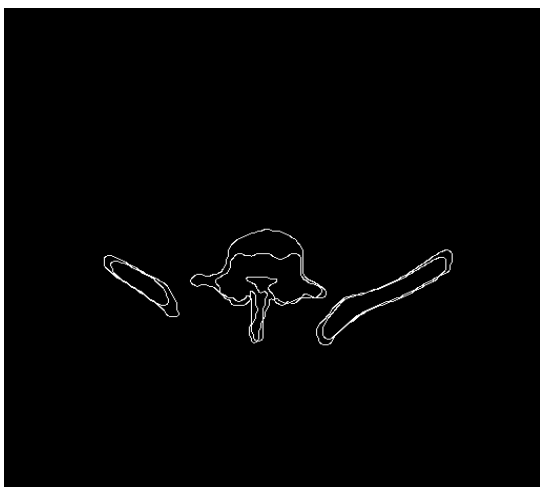
In some images, bone edge gray levels may appear faded. In that scenario, the segmented bone may not include these edges. In order to detect these edges, edge merging is useful. Figure 7.6 shows the merged edges, final bone segmentation and masked images.



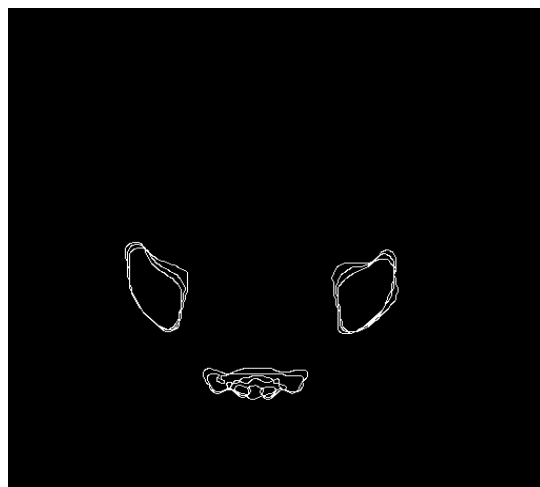
(a) Original image example A



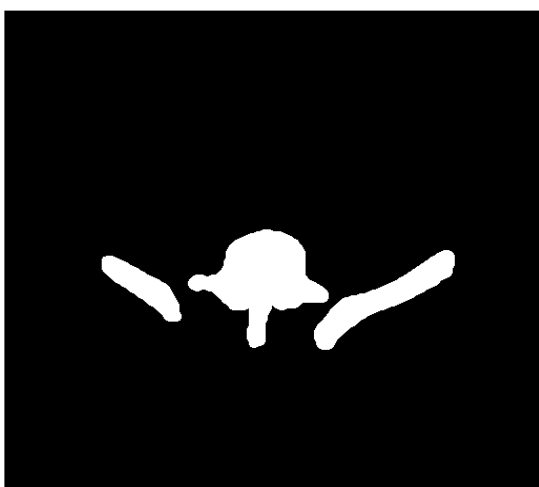
(b) Original image example B



(c) Merged edges example A



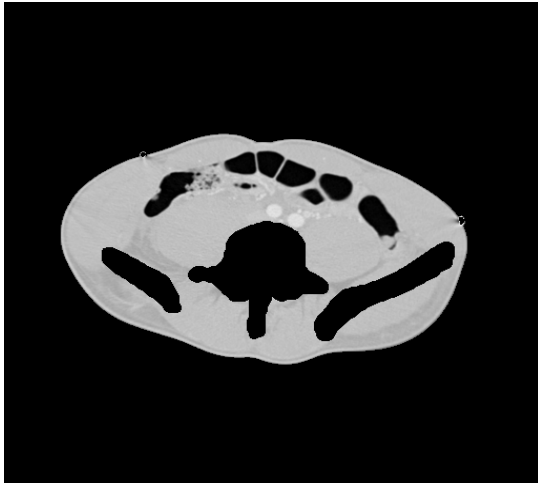
(d) Merged edges example B



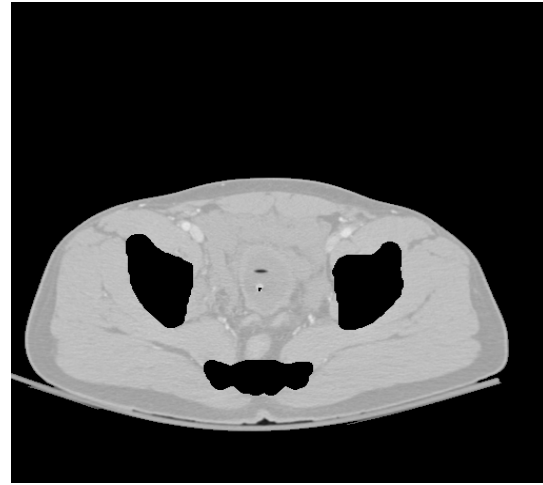
(e) Final bone segmentation example A



(f) Final bone segmentation example B



(g) Segmented bone masking example A



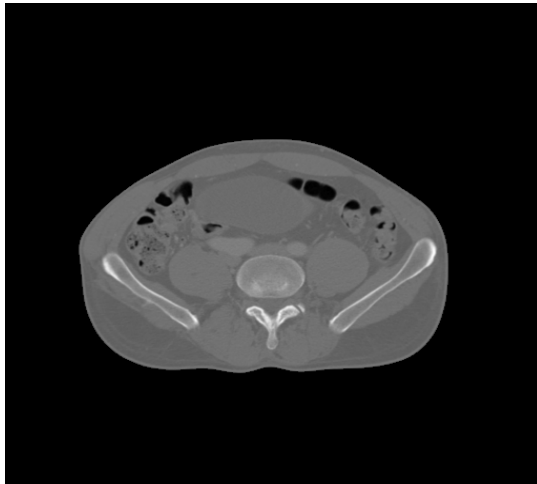
(h) Segmented bone masking example B

Figure 7. 6. Sample results for edge merging, final bone segmentation and masking

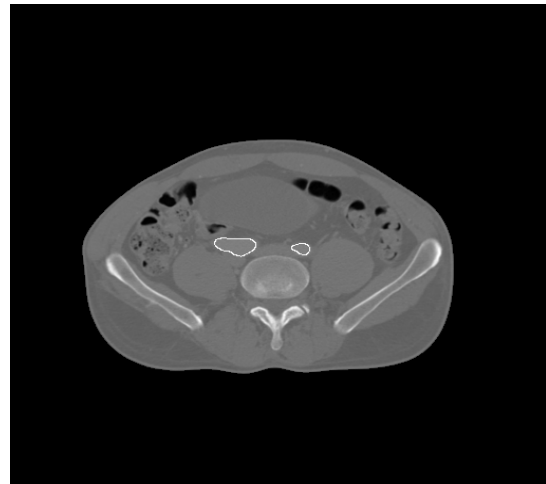
Figures 7.6 (a) and 7.6(b) represent the original CT images from different patients. Few edges of the bones in these figures appear faded. The results in figure 7.6 show that the bone faded edges are successfully segmented and masked. The edge merging technique used in this project is able to successfully segment these faded bone edges. This is because these faded bone edges are visible in either the previous or subsequent image. Due to edge merging, along with the strong edges, the faded edges are also segmented since the edge information from the previous and subsequent image is incorporated into the current image edge detection. Figure 7.6(c) has only two edges merged compared to the figure 7.6(d). This is because the image in figure 7.6(c) is the first image in a particular scan. Figures 7.6(g) and (h) has some regions masked along with the bone regions. These regions are the bright regions such as artifacts and catheter present in the image that are masked during the previous stage of the algorithm.

7.5.3. Artery Detection

This part of the results presents the artery detection in pelvic images. The major arteries in the pelvic region are aorta and its branches. Figures 7.7 through 7.10 show the results of detected arteries.

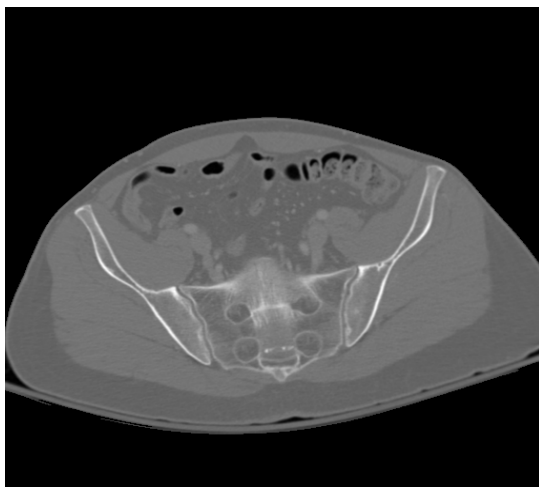


(a) Original image

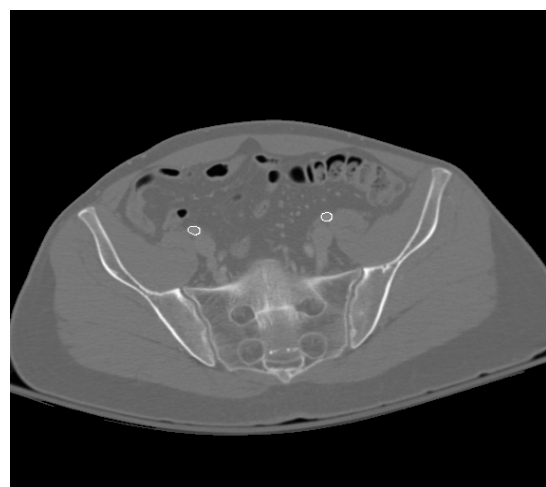


(b) Common iliac arteries detection

Figure 7. 7. Sample result for common iliac arteries detection



(a) Original image



(b) External iliac arteries detection

Figure 7. 8. Sample result for external iliac arteries detection

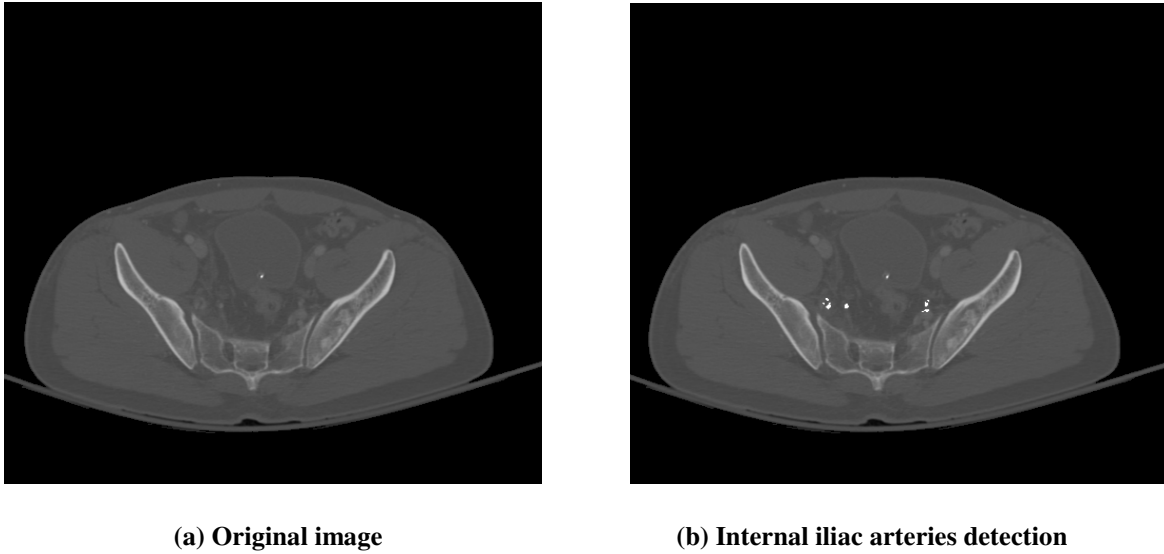


Figure 7. 9. Sample result for internal iliac arteries detection

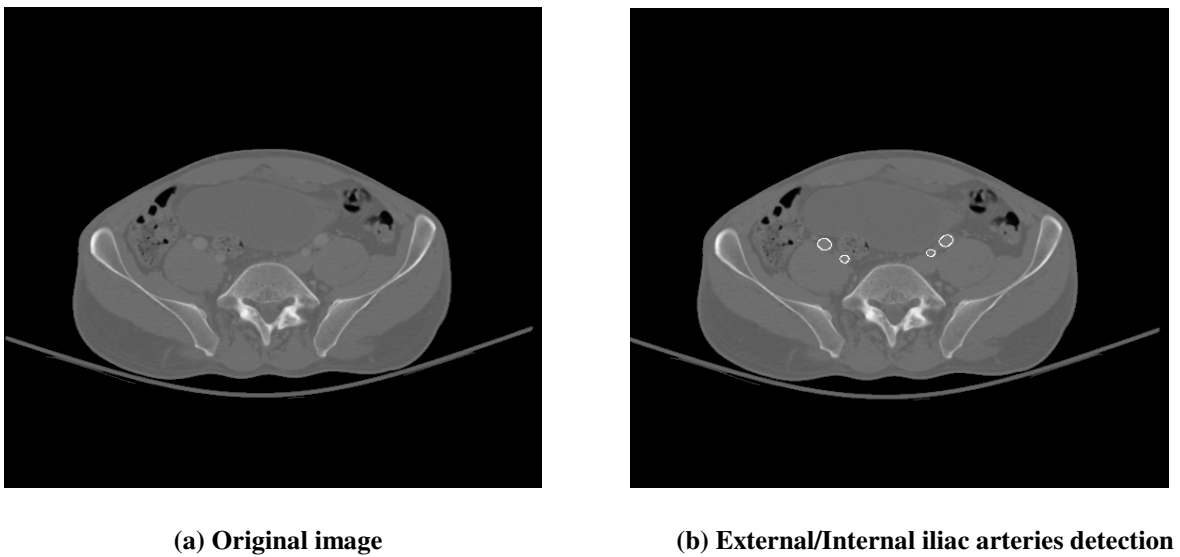


Figure 7. 10. Sample result for external/internal iliac arteries detection

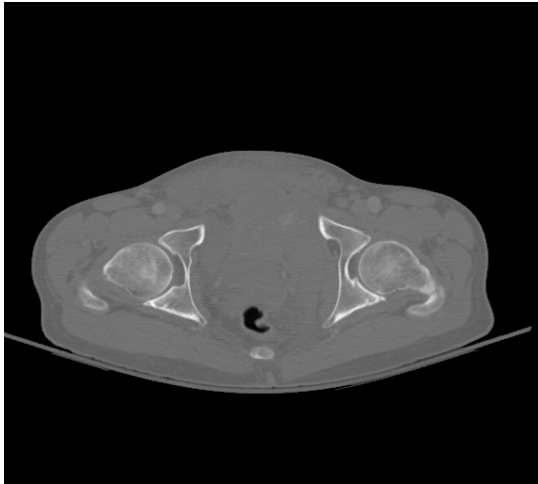
In figure 7.7, sample common iliac arteries results are presented. Aorta branches out to common iliac arteries and these arteries branch out further to external iliac and internal

iliac arteries. The external iliac arteries results are given in figure 7.8. Figure 7.9 show the sample internal iliac arteries detection. From the figure, it can be observed that all of the internal iliac arteries pixels are not detected. The reason for this is the conservative nature of the algorithm. The algorithm proposed in chapter 3 considers the average and maximum gray level values detected from the external iliac arteries as the arteries gray level range. If pixels gray levels are less than the considered range, then they are not considered as internal artery pixels. Internal arteries branch out further and they fade away after some time. During this time, the gray levels of these arteries become closer to the gray levels of the soft tissues. Therefore, since their gray levels are less than the considered gray levels, they are not recognized as the internal artery pixels. Figure 7.10 shows the sample detection results of both external and internal iliac arteries. As soon as common iliac arteries start branching out, the internal iliac arteries gray levels are similar to the external iliac arteries. Therefore, majority of internal iliac arteries pixels' gray levels fall within the same range. This can be observed in the figure.

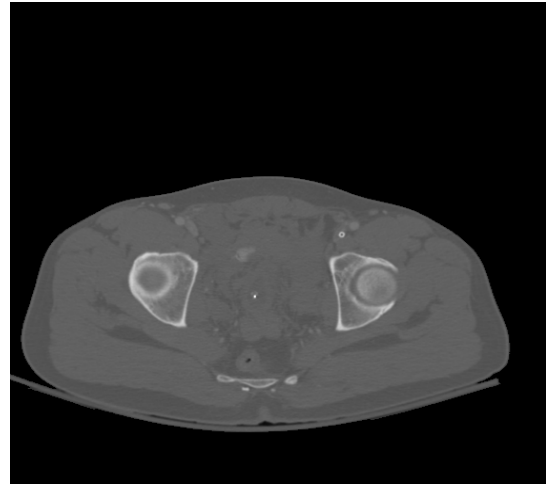
7.6. Hemorrhage Detection, Segmentation and Quantitative Measurement

Once the arteries are detected, any unwanted objects in the image are filtered using the methods described in chapter 4 and the remaining objects are considered as hemorrhage. Figure 7.11 shows the sample results of detected hemorrhage. Figures 7.11 (a) and (b) show the original CT images and figures 7.11 (c) and (d) show the detected binary hemorrhage region. The algorithm is tested on 11 pelvic trauma patients' images out of which 5 patients have hemorrhage. Table 7.1 shows the performance of the proposed

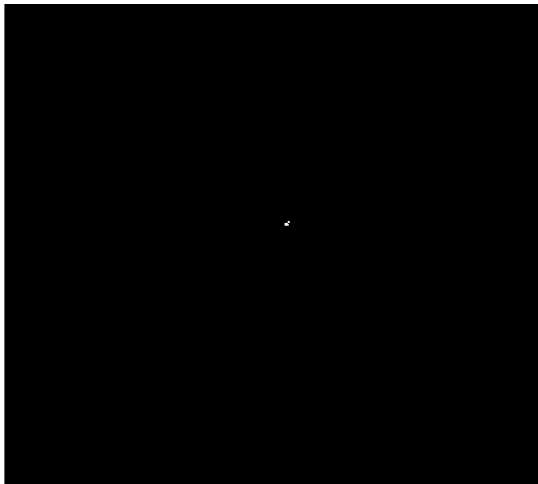
hemorrhage detection technique. The performance is evaluated based on the accuracy, sensitivity and specificity of hemorrhage detection. It can be observed from the table that relatively high accuracy, sensitivity and specificity have been achieved for hemorrhage detection.



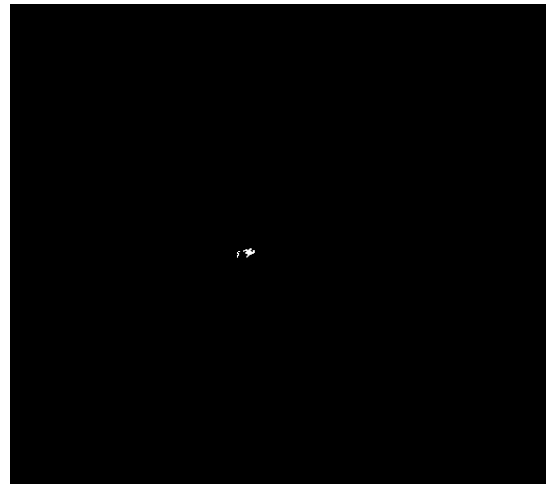
(a) Original image example A



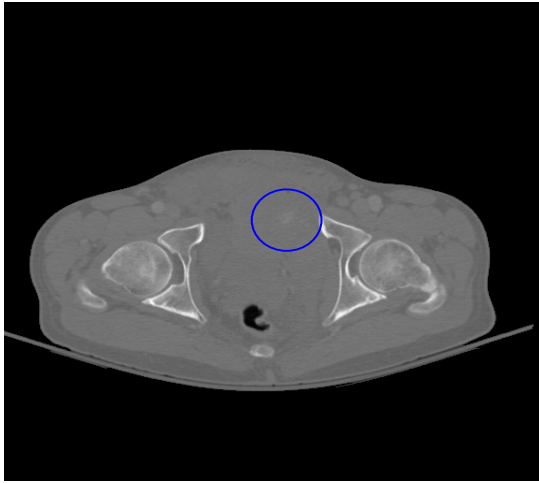
(b) Original image example B



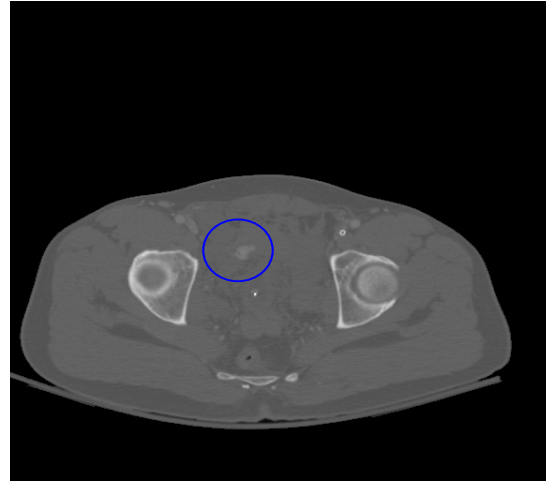
(c) Detected hemorrhage binary image example A



(d) Detected hemorrhage binary image example B



(e) Detected hemorrhage example A



(f) Detected hemorrhage example B

Figure 7. 11. Sample hemorrhage detection results

Statistical Results	Accuracy	Sensitivity	Specificity
Rate %	90.34	91.54	90.25

Table 7. 1. Performance of the proposed hemorrhage detection method

Figure 7.12 shows the sample result of false hemorrhage detection. It can be observed in figure 7.12 (b) that a soft tissue region is identified as hemorrhage. This is because of the gray levels of the soft tissue being within the same gray levels of arteries. There are few cases where the proposed method is not able to detect hemorrhage. This is due to multiple reasons: very small hemorrhage size located next to the bone, and faded hemorrhage with gray levels less than the gray levels of the arteries.

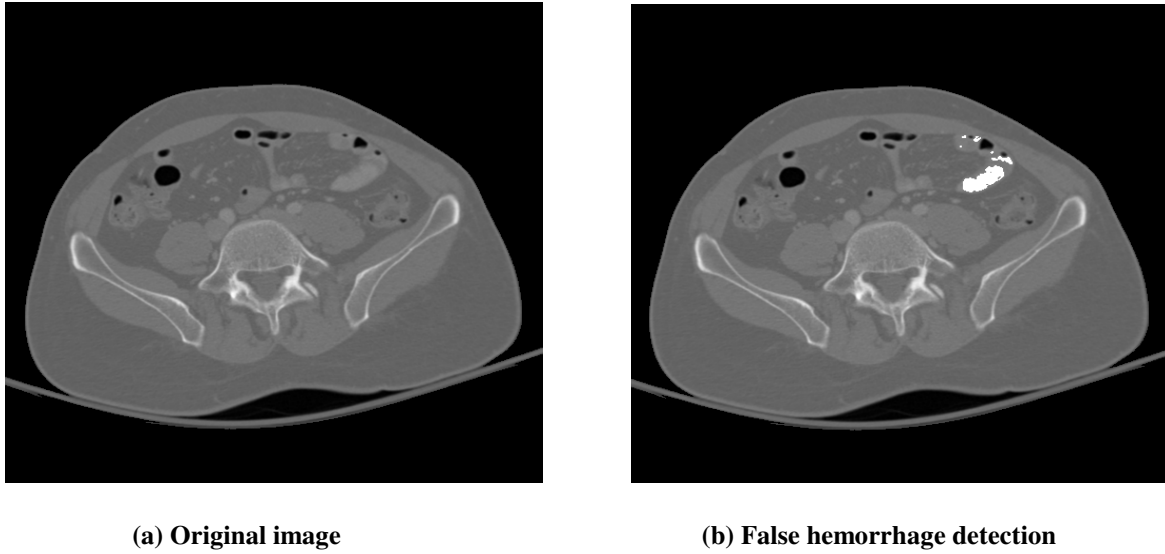


Figure 7. 12. Sample hemorrhage detection results

For hemorrhage segmentation, the ROI size qxq in the hemorrhage matching section is chosen as 100. This value is chosen because a smaller window size may not contain the entire hemorrhage region and if a larger size is chosen, then the non hemorrhage tissues might be present along with the hemorrhage region making hemorrhage segmentation much complicated. During the rule optimization, the values chosen initially for the penalty parameter C are 0.1, 0.01, and 0.001. The optimal C value obtained is different for each image in the patient. It is dependent on the accuracy of classification. The penalty parameter for which the accuracy is maximum is chosen as the optimal penalty parameter. For the region growing process, the window size m is chosen as 3. The pixel factor η is chosen as 50. This value is selected because, in order for the algorithm to be restrictive in region growing, it is required to consider a window that is dominated by the hemorrhage pixels. If the value is chosen lower than this, the probability of over segmentation might

increase and if the value is chosen higher than this value, then the algorithm becomes too restrictive and might leave hemorrhage pixels out affecting the segmentation.

Figure 7.13 show the sample hemorrhage segmentation results. The proposed method is able to segment hemorrhage very well for 93.85% of the cases used in the study. For these cases, the area of segmented hemorrhage is greater than 90% of the original hemorrhage. These cases are considered as good as the mis-segmented area is <10%. The overall average mis-segmented area is 4.8%. For 1.54% of the cases, the area of hemorrhage segmented ranges from 80 to 90% and is considered as acceptable. The average mis-segmented area in these acceptable cases is 15.29%. For the remaining 4.61% of the case, the segmented hemorrhage is unacceptable and the average mis-segmented area is 28.26%. These classifications: good, acceptable, and unacceptable, are made based on the assessment by expert radiologists. These classifications are made to determine how well the algorithm segmented the hemorrhage. However, from radiologists' aspect, if a hemorrhage is detected, then an angiography is conducted irrespective of the classification. Overall, the proposed method is able to segment hemorrhage very well during the arterial phase and the veinal phase.

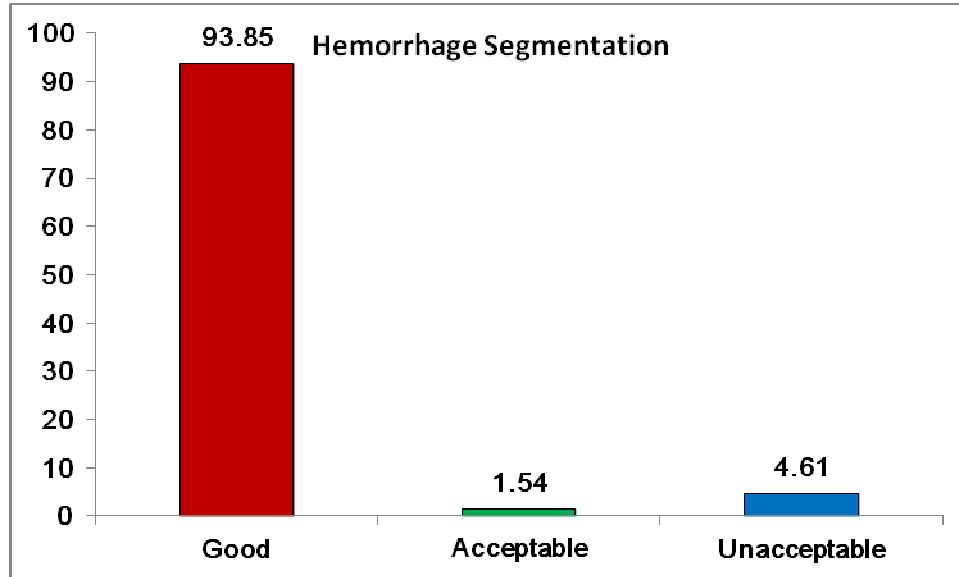
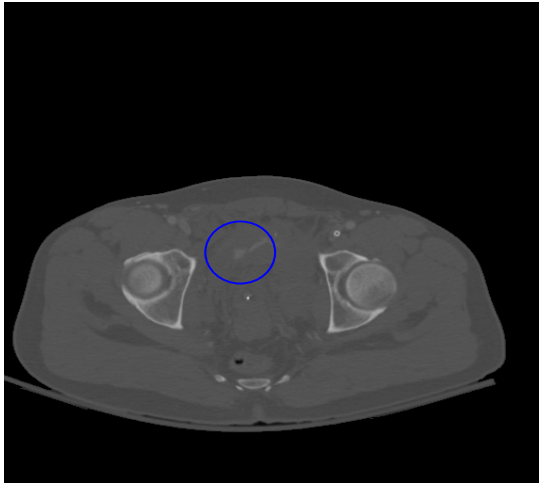
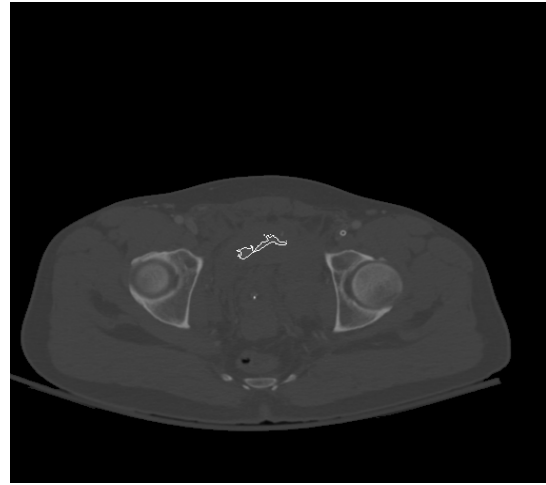


Figure 7. 13.Performance of the proposed segmentation method

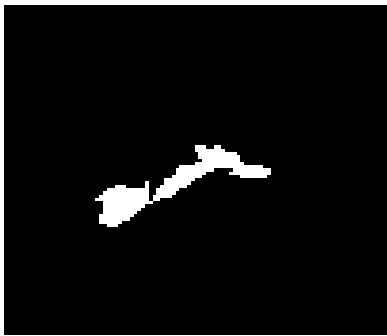
Figure 7.14 shows the sample results of segmented hemorrhage. This is one of the cases where hemorrhage is very well segmented. Figures 7.14 (c) through (e) gives the segmentation results at various stages of segmentation, i.e., segmentation result after hemorrhage matching, rule optimization, and region growing. It can be observed from these figures that the no new pixels have been added to the hemorrhage region after optimization. This is because of an accurate segmentation at the hemorrhage stage and distinguishable hemorrhage region boundaries from the soft tissue regions. However, new pixels are added to the hemorrhage region after region growing. And the percentile of hemorrhage area grown from the optimization to region growing is 7.4%. These results show that the region growing helps determining the missing hemorrhage pixels.



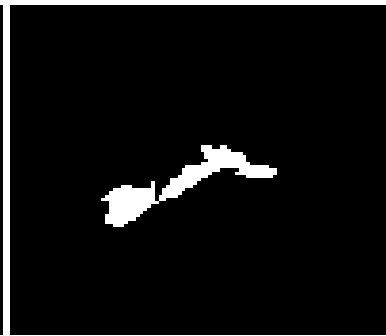
(a) Detected hemorrhage example A



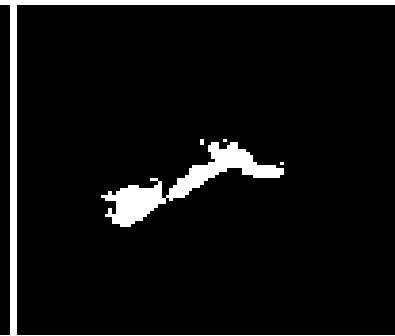
(b) Segmented hemorrhage example A



(c) Hemorrhage matching result



(d) Rule optimization result

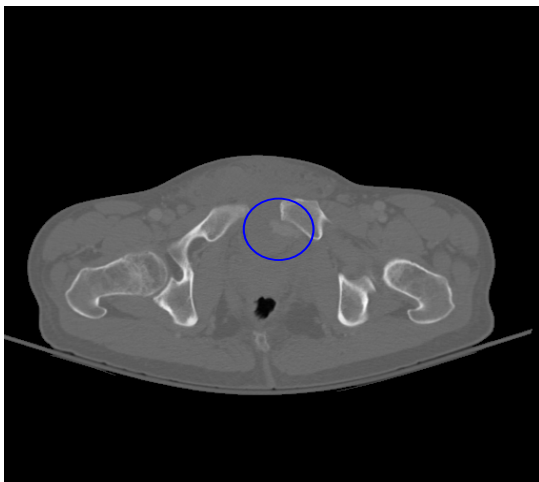


(e) Region growing result

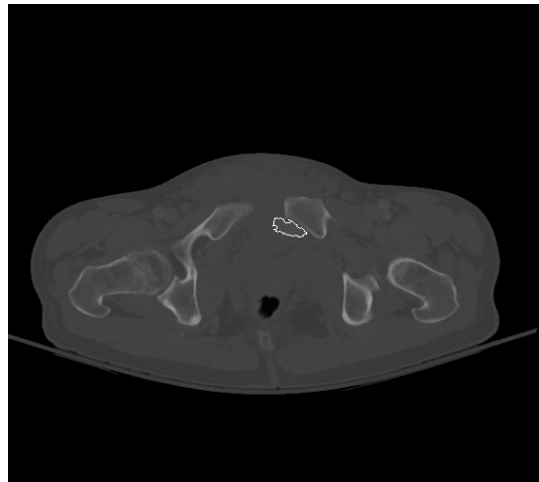
Figure 7. 14. Sample hemorrhage segmentation results

In the case of patient in figure 7.15, the hemorrhage is located next to the bone. This segmentation is considered to be good. As hemorrhage is located next to the bone, the gray levels of the faded bone edges might be similar to hemorrhage gray levels. The use of distance information and gray level variation information helped in differentiating the hemorrhage from the bone regions for majority of the pixels. However for few pixels, the proposed method is unable to differentiate between the hemorrhage and bone pixels. Figures 7.15(c) through (e) shows the performance of proposed method at various stages.

In these figures, the percentile of hemorrhage area grown from the MI technique to optimization is 41.57%. The percentile of hemorrhage area grown from optimization to region growing is 4.49%. The hemorrhage area grown through region growing is minimal when compared to the area grown through rule optimization.



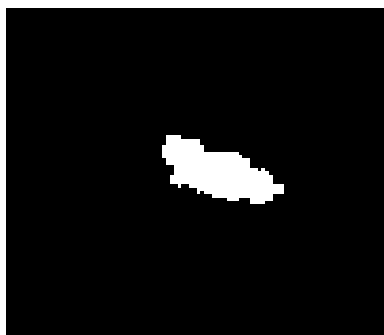
(a) Detected hemorrhage example B



(b) Segmented hemorrhage example B



c) Hemorrhage matching result



(d) Rule optimization result



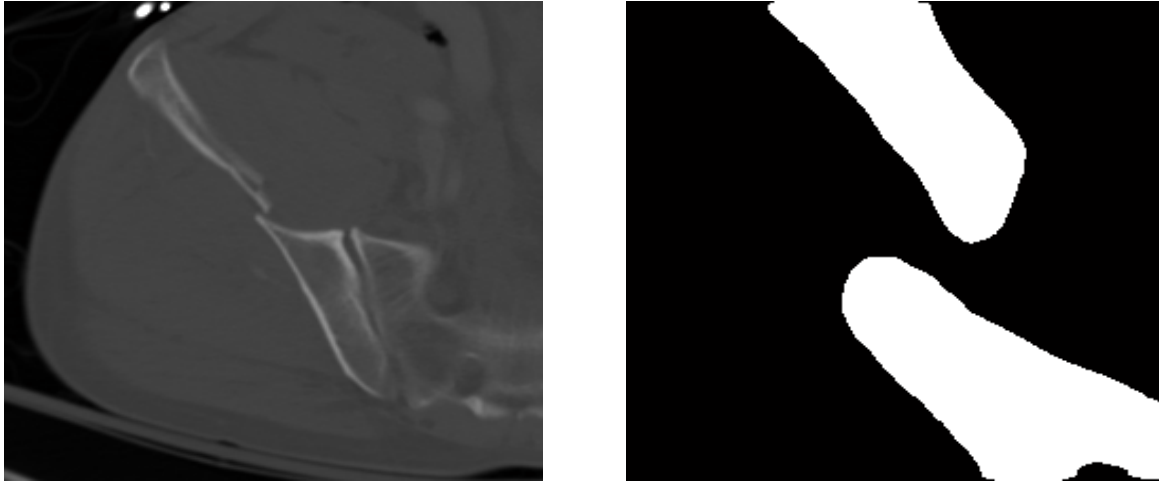
(e) Region growing result

Figure 7. 15. Sample hemorrhage segmentation results

The next step after hemorrhage segmentation is to quantify the hemorrhage. The number of bleeding foci is determined from the detected hemorrhage regions. The volume of hemorrhage is calculated for only the slices that are detected as hemorrhage. The location of hemorrhage is determined if it is located on the left /right side of the body and if it is located in the vicinity of the bone.

7.7. Outcome Prediction

Some of the hemorrhage features extracted in this study are combined with the fracture features extracted from the companion project and patient medical records and demographics are combined in order to automatically classify the outcome. A total of 16 features are used originally for the study. The results of extracted features for bone fracture are given in figure 7.16. The fracture feature reduction using DB index provided a low DB index value for the total bone displacement and the total number of bone fractures compared to the some of the individual fracture features. This shows that these features can provide the complete fracture information. Therefore, the number of fracture features used for the next stage feature selection process is reduced to from eight features to two. As the size of dataset is small, reducing the total number of features will minimize over fitting of data. In addition, feature reduction reduces the overall processing time of decision making system which is very helpful in trauma care.



(a) Pelvic CT image

(b) Fractured bone

Figure 7. 16. Sample results of fracture and hemorrhage detection

A total of 10 features are used for the SU based feature selection process. This approach has removed one feature out leaving 9 features for classification. The data from 49 patients is used for the study. The performance of the BLMT technique is tested using ten fold cross validation in Weka 3.6. Table 7.2 provides the performance of the BLMT technique. This table also provides the comparison of the BLMT method with other techniques C4.5 and Random forest. A total of eight trees and a value of 0 (unlimited) depth are chosen for Random forest. The number of trees are selected in proportion to the number of features for classification. The results from table 7.2 show that the BLMT technique performed well compared to the other two techniques. The data is tested using support vector machine too. However, the classification is not comparable to any of the techniques provided in table 7.2.

		BLMT	C4.5	Random Forest
With Boosting	Accuracy	87.75	79.59	65.31
	Sensitivity	84.61	76.9	62.5
	Specificity	88.88	80.55	75
Without Boosting	Accuracy	81.63	77.55	75.51
	Sensitivity	69.23	53.84	53.84
	Specificity	86.11	86.11	83.33

Table 7. 2. Performance of different classifiers with outcome being home or rehabilitation

Boosting used in the study improved the performance of the techniques. The BLMT technique used in the study has also increased the specificity along with the prediction accuracy. This helps reduce the false alarms which will reduce errors ultimately. The above results are for predicting the outcome on whether a patient is sent to home or for rehabilitation.

Table 7.3 shows the results obtained using the proposed technique with a different outcome prediction- number of days a patient has been in ICU. The outcome has two classes. If a patient is in ICU for ≤ 2 days, then it is classified as class one, else class two.

		BLMT	C4.5	Random Forest
With Boosting	Accuracy	93.88	85.71	87.75
	Sensitivity	97.36	94.73	94.73
	Specificity	81.81	54.54	63.63
Without Boosting	Accuracy	89.79	83.67	87.75
	Sensitivity	97.36	92.10	94.73
	Specificity	63.63	54.54	63.63

Table 7. 3. Performance of different classifiers with outcome being ICU days

The results from the above table show that the BLMT technique accuracy has improved with a different outcome. This might be because of the better mapping of the features with this outcome. It can also be observed from table 7.3 that the sensitivity of the classifier is higher for all the three methods when compared to the specificity. However, the specificity of BLMT technique is comparable to its sensitivity which should be usually better in reducing the false alarms when compared to the other techniques used in the study. On comparing the overall performance of the BLMT technique with the other techniques, the results show that this technique outperformed other techniques and has a better specificity too.

7.8. Discussion

The image preprocessing is successful in eliminating the majority of surrounding artifacts and extracting the pelvic region. The best template detection is vital in the process of identifying the bone objects and for template classification in artery detection. The edge merging and bone segmentation algorithms used are able to successfully segment the bone region in most of the cases. The merging technique facilitated the masking of bones with faded edges. The effect of merging on hemorrhage located close to the bones is minimal. However, in the case of severe fractures where the fractured bone pieces are far apart, the edge merging technique is only able to merge partially. The method of artery detection and incorporation of their gray level information is very helpful in selecting a threshold for initial detection of hemorrhage. The algorithm used for external artery detection is able to locate arteries well in both the arterial phase and venal phase. In general, the artery gray

levels are higher than the vein gray levels. But if there is a delay in scanning the pelvic region after the contrast injection, then the difference between the gray levels of arteries and veins decreases as delay increases. Therefore, at those times, even the external iliac veins are detected along with the arteries and their gray levels are taken into account. This is helpful during the hemorrhage detection in veinal phase.

Setting threshold for internal iliac arteries detection from the external iliac arteries proved to be successful in masking the internal iliac arteries. The implemented sequence of morphological operations to remove the unwanted regions from the image is successful in eliminating the majority of residue bone, artery or other soft tissue pixels. The proposed rule based approach is able to segment hemorrhage very well. This approach utilized various pixel information in order to segment hemorrhage. The segmentation is unacceptable in few cases which may be due to the bridging of hemorrhage pixels through soft tissue pixels. Hence, these few pixels are left out during the segmentation. Increasing the size of selected window might help segment these pixels. However, the tradeoff is, it might lead to over segmentation. Incorporating pixel information into the rule optimization helps differentiate the hemorrhage from soft tissue and bone region. The optimization technique is able to segment hemorrhage edges very well. The region growing process is able to determine the missed hemorrhage pixels. In addition, the proposed method is able to segment hemorrhage edges that may not be measurable through visual inspection. The results are validated on the basis of assessment and evaluation made by the radiologists on the CT images.

The classification technique used in the study performs well. The multi-stage feature selection process helped in selecting only the predominant features. The proposed BLMT technique performed well compared to the other techniques presented in the study. This technique is also able to maintain relatively high specificity which is good for reducing false alarms.

CHAPTER 8 RESULTS AND DISCUSSION – SPLEEN SEGMENTATION

8.1. Introduction

Solid organ segmentation in abdominal trauma is very crucial in order to detect any abdominal injuries. This chapter presents and discusses the obtained results. In each stage, the multiple examples of the results obtained will be provided. The images for each patient were selected to represent a variety of anatomical structures. These variations allow better assessment of the proposed techniques when dealing with different variations in shape of the spleen.

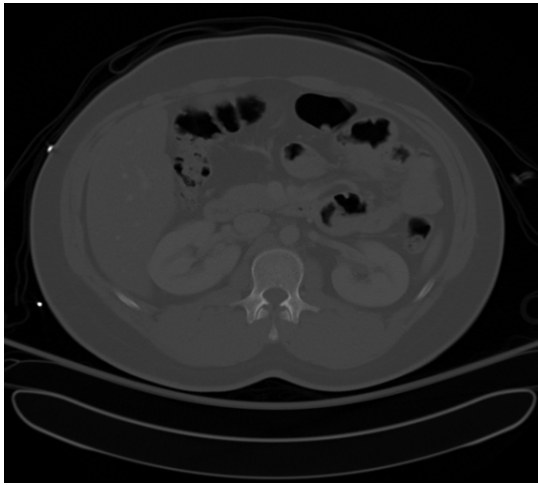
8.2. Dataset

The data for the study is obtained from Virginia Commonwealth University Medical Center. The data is collected from the patients that exhibit mild to severe abdominal injury such as solid organ injury and hemorrhage etc. The data is collected from eight patients with each patient containing 20 to 67 images. Axial CT dicom images of 5 mm slice thickness are used in the study. The entire dataset contains 276 images in total.

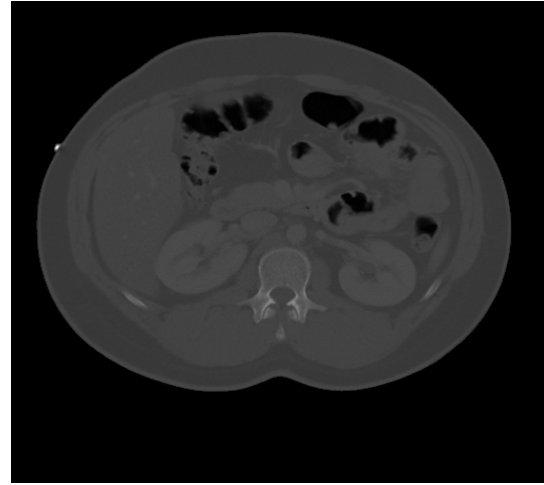
8.3. Artifacts Removal and Contrast Enhancement

Figure 8.1 presents the results obtained from the first proposed preprocessing step for artifact removal such as cables, CT table, hands, etc. This step is very crucial because inclusions of artifacts can influence the gray level statistics of the image. The result from

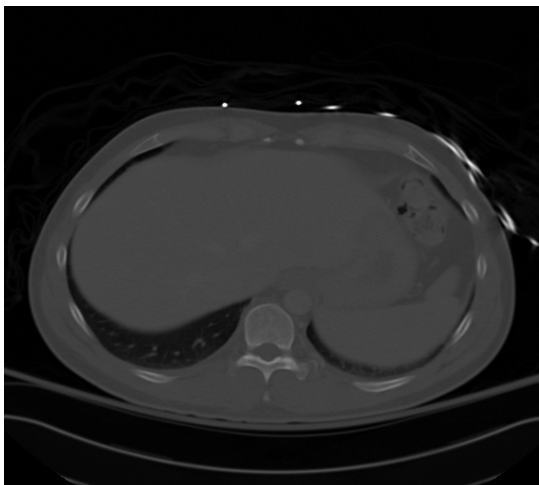
figure 8.1 (b) shows that the proposed technique is able to successfully remove artifacts surrounding the abdomen region. However, in figure 8.1(d), the CT table and the other surrounding bright regions are not eliminated. This is because these regions are attached to the abdomen itself and are considered as part of the abdomen.



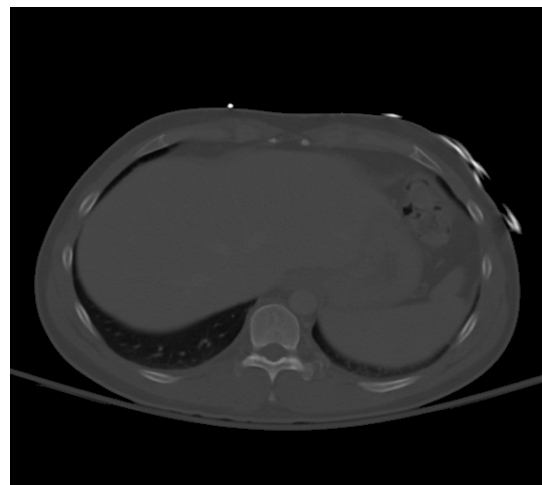
(a) Raw abdomen CT image example A



(b) Preprocessed image example A



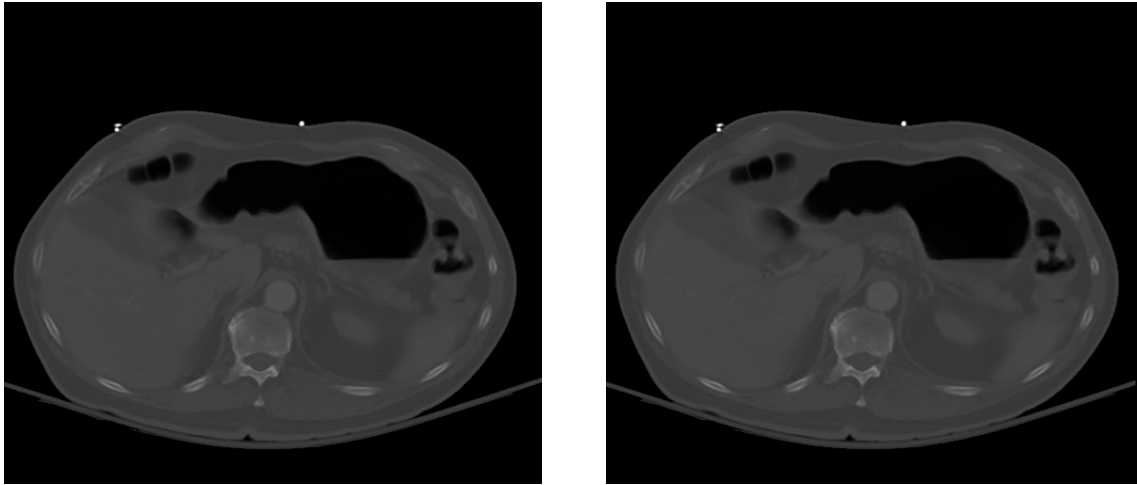
(c) Raw abdomen CT image example B



(d) Preprocessed image example B

Figure 8. 1. Sample preprocessing results

Once the artifacts are removed, the extracted region is filtered to remove any speckle noise present in the image. Figure 8.2 presents the results obtained with Gaussian filtering.

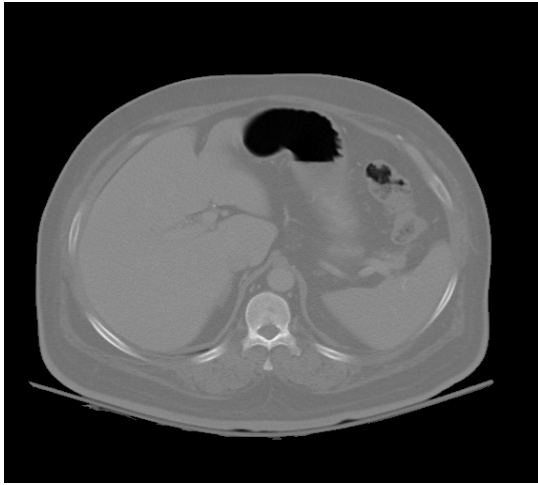


(a) Preprocessed image example A

(b) Gaussian filtered image example A

Figure 8. 2. Sample Gaussian filtering results

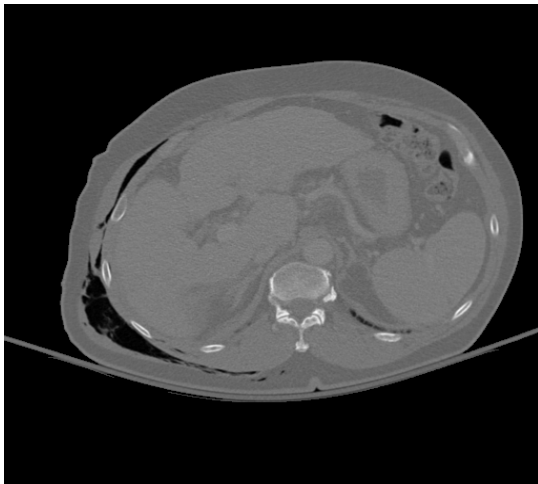
The next step in the spleen segmentation is contrast enhancement. Spleen segmentation is a challenging task as the majority of solid organs in the abdomen region have a similar gray level range. This similarity makes it difficult to differentiate organs especially when located next to each other. Figure 8.3 shows the results of contrast enhancement.



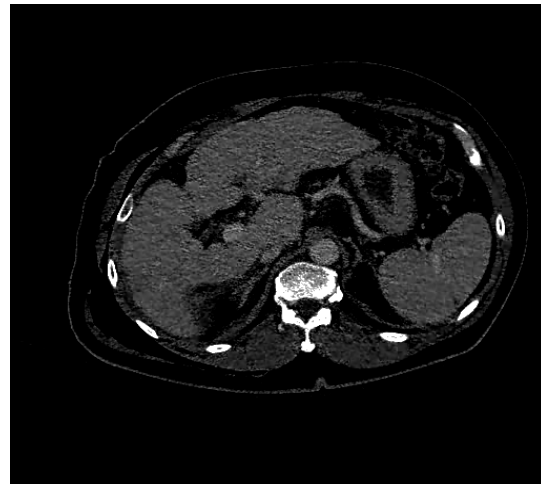
(a) Preprocessed image example A



(b) Contrast enhanced image example A



(c) Preprocessed image example B



(d) Contrast enhanced image example B

Figure 8. 3. Sample contrast enhancement results

It can be observed from figure 8.3 that the solid organs are differentiable from the other soft tissues. In addition, it can be observed that the gray levels of vertebrae and ribs are significantly higher than the solid organs and the gray levels of some of the other regions are much lower than the solid organs gray level range. This contrast enhancement

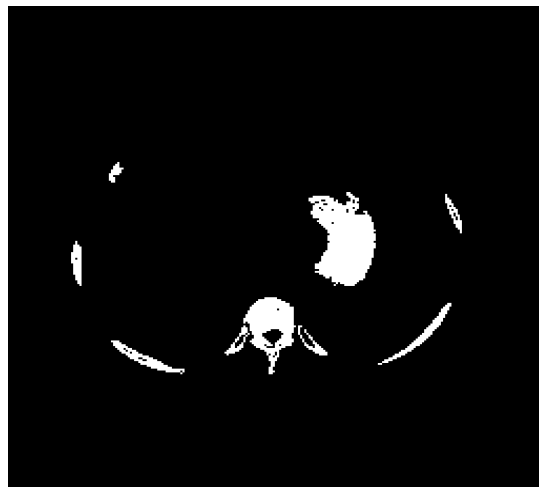
facilitates the bright region masking which further helps in minimizing the influence of the gray levels of these regions on the organs such as spleen, liver, and etc.

8.4. Bright Objects Mask Formation and Edge Detection

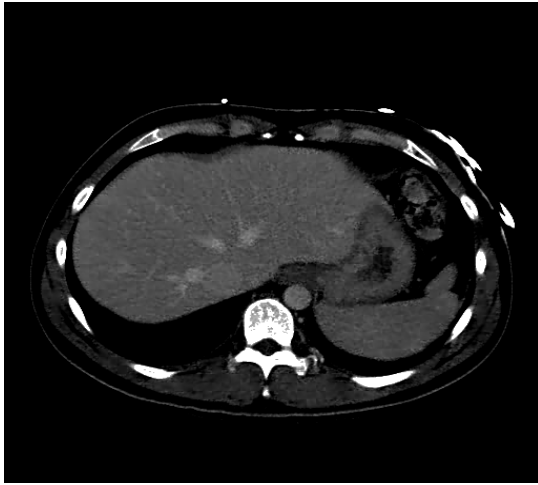
In order to automatically detect the location of spleen in each image, this study utilized the vertebrae and rib information. This is obtained by forming a mask on all bright regions in the contrast enhanced image. Figure 8.4 shows the bright objects mask obtained from the contrast enhanced abdomen image.



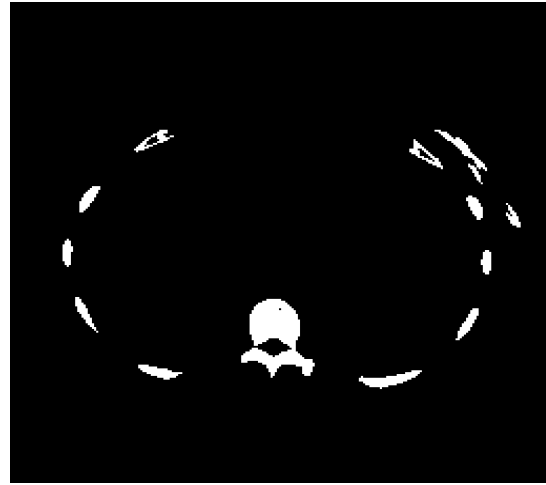
(a) Contrast enhanced image example A



(b) Bright objects mask image example A



(c) Contrast enhanced image example B



(d) Bright objects mask image example B

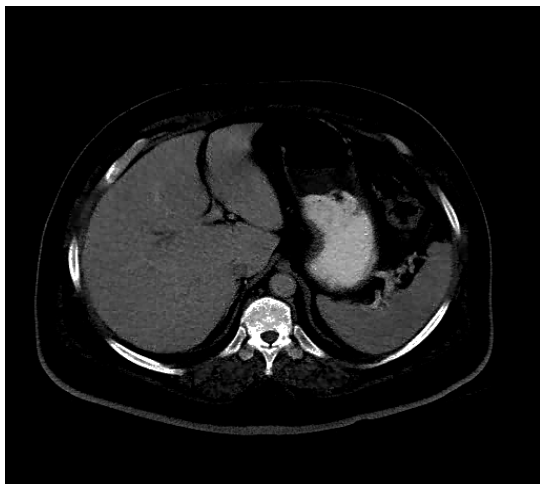
Figure 8. 4. Sample bright objects mask results

From figure 8.4 (b), it can be observed that the mask of the vertebrae, ribs and contrast enhanced stomach is obtained, whereas in figure 8.4 (d), mask of bone, ribs and other bright regions are obtained. These results show that the proposed mask formation technique is able to successfully obtain the mask of contrast enhanced tissues, bones, and other bright objects from the image. Once the mask is formed, the edges of these objects are determined which are later used for segmentation.

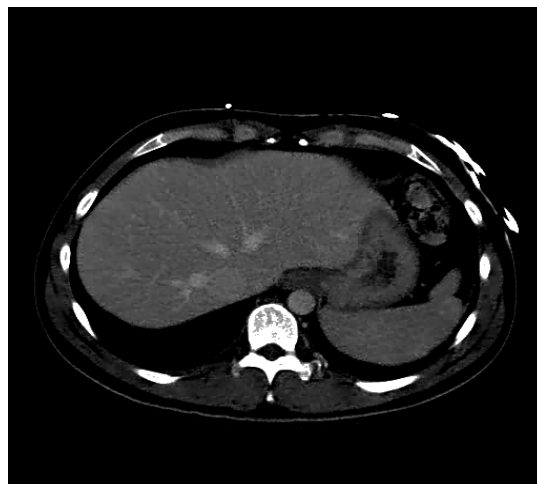
8.5. Bright Objects Segmentation and Masking

Figure 8.5 shows the results of segmentation and masking. The segmentation is obtained by growing seeds around the detected edges of the initial mask. The segmentation results from figures 8.5(c) and (d) show that the bright region pixels in the neighborhood of the regions in the initial mask are grown. The proposed method of bright objects segmentation is able to segment not only bone but also ribs and contrast enhanced tissues.

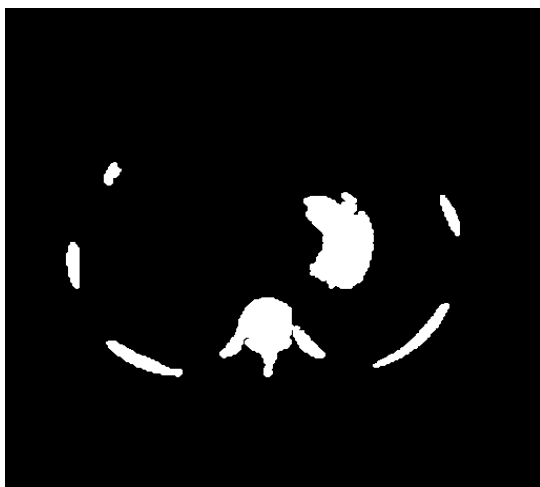
It can also be observed in figure 8.5 (d) that some of the smaller bright objects are not present in the segmented image. This is due to the morphological operations performed during bright objects mask formation stage. Figures 8.5 (e) and (f) show the masked bright objects images. This masking facilitates the spleen segmentation in the latter stages.



(a) Contrast enhanced image example A



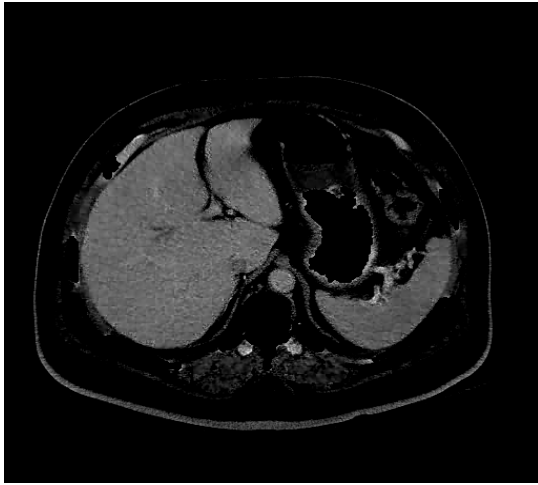
(b) Contrast enhanced image example B



(c) Bright objects segmented image example A



(d) Bright objects segmented image example B



(e) Bright objects masked image example A

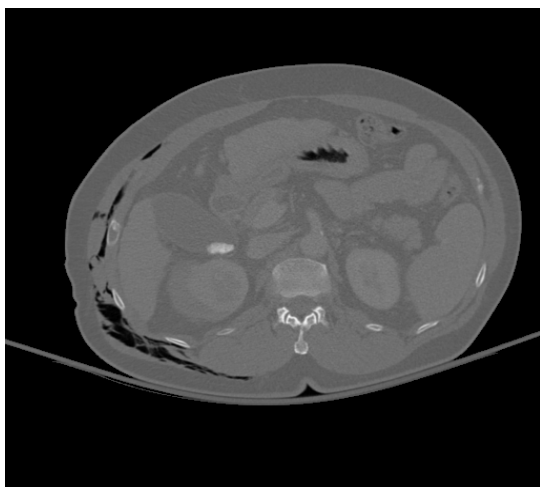


(f) Bright objects masked image example B

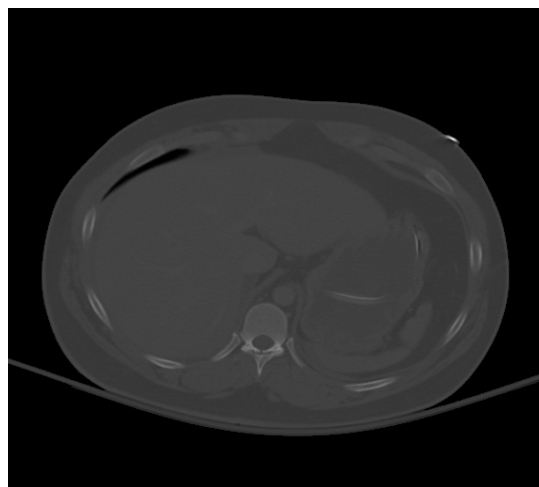
Figure 8. 5. Sample bright objects segmentation and masking results

8.6. Spleen Segmentation

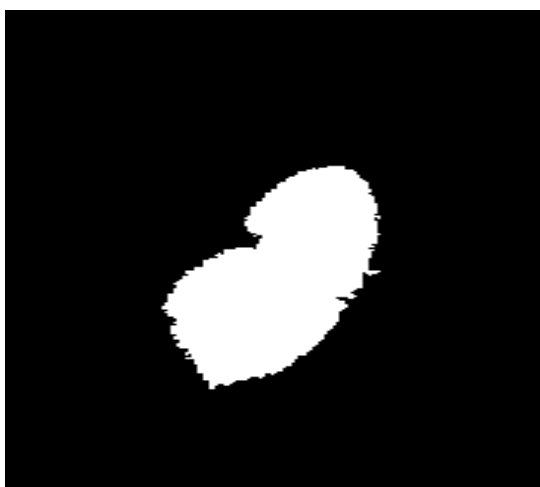
The spleen segmentation involves multiple stages: identifying the ROI, initial spleen segmentation, edge merging, and final spleen segmentation. Figure 8.6 provides the results of spleen segmentation in different stages. Figures 8.6(c) and (d) show the results of initial segmented spleen. The result in figure 8.6 (c) show that majority of the spleen is segmented from the image. However, in figure 8.6(d) the spleen is segmented partially. This is because of the threshold used to segment spleen pixels. The spleen in this image has laceration. Due to this, the area of spleen with laceration has lower gray levels resulting in partial segmented spleen. Merging spleen edges help segmenting the entire spleen region when the laceration or hemorrhage is present. Figures 8.6(e) and (f) show the merged spleen. Merging the spleen in multiple images will cover the entire spleen region which helps in a better segmentation of the spleen.



(a) Preprocessed image example A



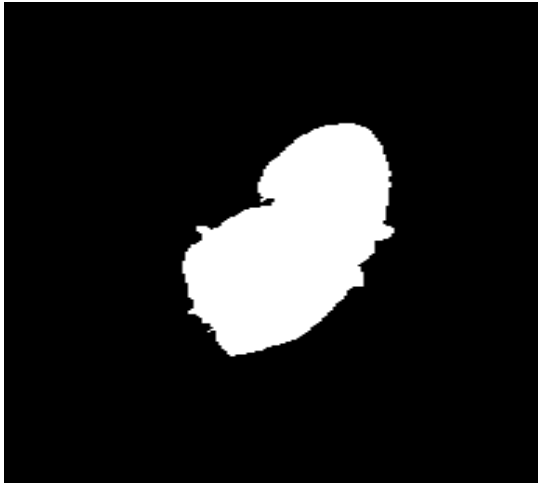
(b) Preprocessed image example B



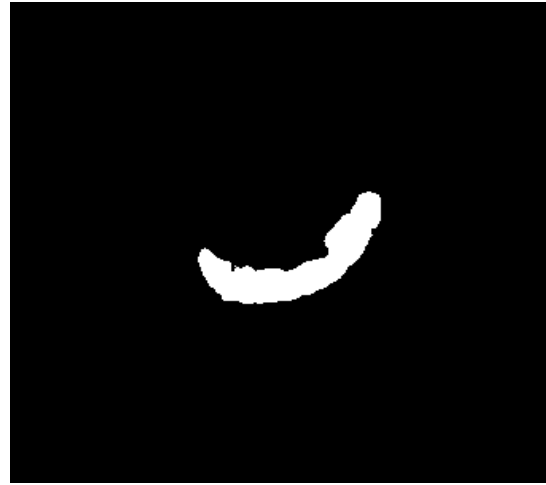
(c) Initial spleen segmentation example A



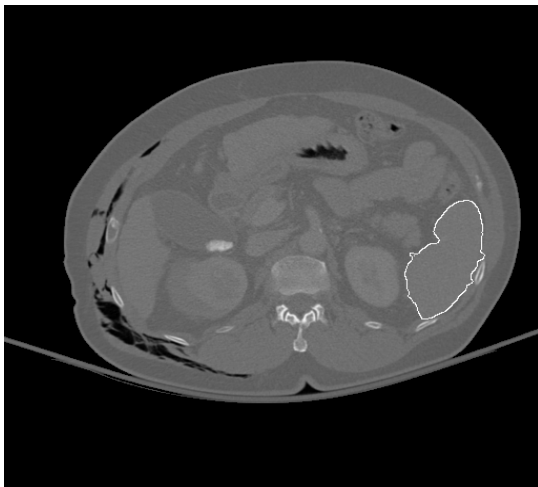
(d) Initial spleen segmentation example B



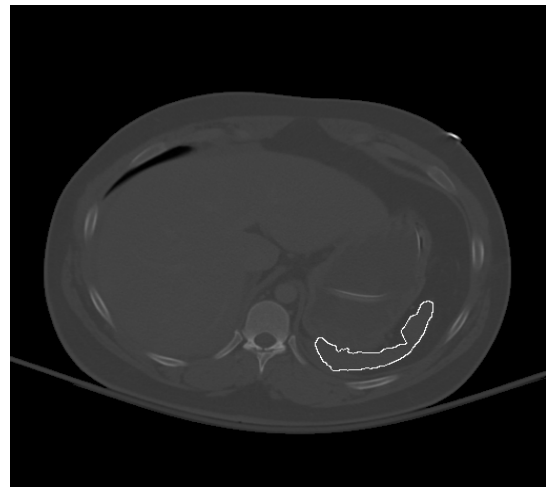
(e) Merged spleen image example A



(f) Merged spleen image example B



(g) Final spleen image example A



(h) Final spleen image example B

Figure 8. 6. Sample spleen segmentation results

Once the merged spleen is determined, it is important to identify the actual spleen region in order to determine the laceration and hemorrhage. Figures 8.6(g) and (h) show the final spleen segmentation results. It can be observed from these figures that the threshold method used is able to restrict spleen region growing to other soft tissues whose gray levels are lower than the gray levels of the spleen.

The performance of the proposed techniques is evaluated in two phases: measuring the accuracy of spleen detection, and measuring the area of the segmented spleen. Table 8.1 provides the spleen detection accuracy. The results show that the proposed method is able to detect spleen very well. In addition, the proposed method is also highly sensitive in detecting spleen in the images.

Statistical Results	Accuracy	Sensitivity	Specificity
Rate %	95.28	95.55	93.10

Table 8. 1. Performance of the proposed method in detecting spleen

Figure 8.7 presents the performance of the spleen segmentation technique among all the images. The proposed segmentation technique is able to segment spleen very well in 83.47 percent of the images. For 6.36 percent of the images, the segmentation is acceptable. However, for the rest of the 10.17 of the images the segmentation is unacceptable. Good, acceptable and unacceptable terms are used based on the discussion with expert radiologists. If the segmented area of spleen is greater than 90 percent of the actual spleen region, then that segmentation is considered good. If the segmented area lies between 80 to 90 percent of the actual spleen region, then the segmentation is considered as acceptable. Otherwise, the segmentation is unacceptable. All the spleen detection and segmentation results are evaluated by the radiologists as a ground truth for assessment.

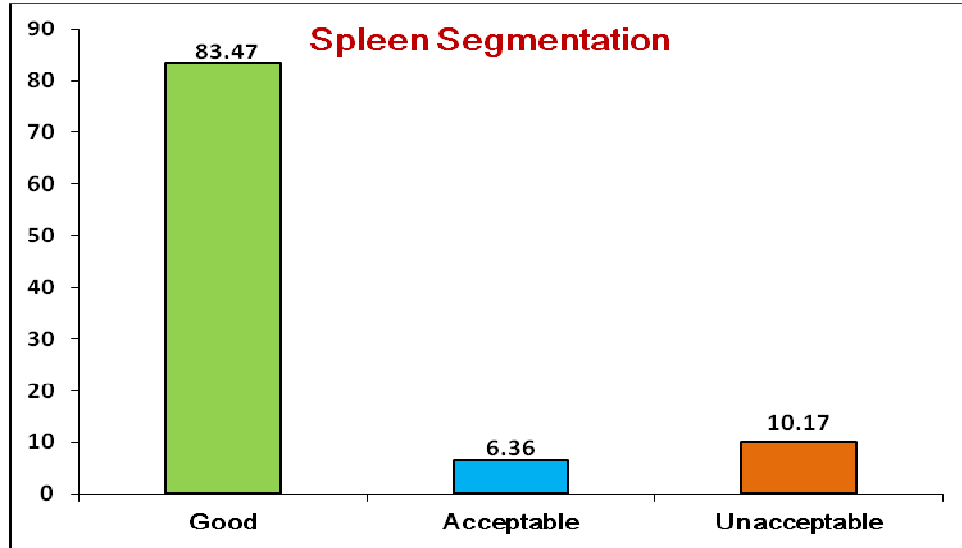


Figure 8. 7. Performance of the proposed method in segmenting spleen

8.7. Discussion

The proposed method is able to segment spleen in majority of the cases. The preprocessing is able to successful remove any artifacts present in the image except for those attached to the pelvic region. Contrast enhancement technique used in the study has enhanced the contrast of solid organs and other bright regions successfully in all the images. The bright objects mask formation technique has detected all of the bright objects present in the image. This helped in minimizing the influence of the gray levels of these objects in the image. The bright objects segmentation technique is able to detect bright object pixels present around the detected edges. These bright object are later masked to minimize the false detection of these objects as spleen. The proposed method is able to detect spleen in most of the cases. For few cases, the spleen is missed because of the

presence of kidney next to the spleen which is falsely detected as the spleen, and for the rest of the cases, the size of the spleen is very small.

The initial spleen segmentation process is able to segment a major part of the spleen in most of the images. However, in few images that have a laceration or hematoma, the proposed method of initial segmentation is only able to segment spleen partially. Merging spleen edges really helped determining the entire area of the spleen. The threshold technique used is able to restrict the spleen region growing to other soft tissue regions in majority of the cases. 10.17 percent of the cases are classified as unacceptable. This is because along with the spleen region, the arteries and other tissues located very next to the spleen are also segmented additionally effecting the segmentation of the spleen region. Over all, the spleen detection and segmentation results are promising.

CHAPTER 9 CONCLUSION AND FUTURE WORK

9.1. Introduction

Hemorrhage is the main cause of mortality in patients with traumatic pelvic fractures. The deaths due to hemorrhage occur within the first 24 hours after a traumatic injury. Therefore, it is vital to quickly and accurately determine the source of bleeding. CT images have been widely used to determine the bleeding. However, it is very time consuming for the radiologists to examine all the images within a short period. This calls for a computer-assisted decision making system that can provide reliable recommendations to physicians and help improve the accuracy of the decision, reduce the decision making time and positively impact the cost of the health care.

The proposed decision making system combines features extracted from images such as hemorrhage detection, fracture detection with patient medical data and demographics to provide the best possible patient outcome predictions and recommendations to physicians.

The dissertation introduced the methods that can help resolve some of the challenges that come from automatically examining CT images. This chapter provides a brief review of the main conclusions drawn from the methodologies and results described in this dissertation. This chapter also explains the future work, and steps to be pursued in order to further explore the formation of computer-assisted decision making system for traumatic pelvic injuries.

9.2. Conclusions

This dissertation presented methods to detect, segment, and quantify hemorrhage. This involved analyzing anatomical information from bone and arteries. The work done previously on bone segmentation laid foundation to this proposed work. Due to the complex nature of pelvis region, it is important to search the entire image for hemorrhage.

The edge merging and bone segmentation methods along with masking described in this dissertation minimizes the chance of false detection of bones as hemorrhage. The proposed catheter masking method eliminates all image artifacts whose gray levels are greater than bone average gray levels. As arteries and hemorrhage have similar gray levels, detection of arteries and incorporation of their gray level information is very helpful in hemorrhage detection. Based on the anatomical knowledge, bone position and templates information, arteries are detected in the images. The gray level information is used to eliminate the soft tissue regions. Morphological operations are later applied to eliminate any residual pixels in the image. After removing the unwanted regions from the image, the remaining objects are identified as hemorrhage. Later, a multi-stage rule based approach is used to segment hemorrhage that utilizes hemorrhage matching, rule optimization and region growing techniques. The segmented hemorrhage is then quantified to assess the bleeding severity. Finally, an automated classification is provided using a multi-stage feature selection process followed by outcome prediction via Boosted Logistic Model Tree.

The project has been expanded to abdominal organ segmentation in order to detect any abdominal injuries in trauma patients. As part of this, the dissertation presented spleen

segmentation. This involved preprocessing, contrast stretching, bright object segmentation and masking, and finally spleen segmentation using spleen edge merging and threshold based technique.

The results presented show that the edge merging and the bone segmentation techniques used are able to mask the bone region very well. The artery detection results show that the external iliac arteries are detected very well by the proposed method. However, only the internal iliac arteries whose pixel gray levels are similar to external iliac arteries gray levels are detected. From the sequential elimination of regions from the image, the hemorrhage present at various locations in the image is detected easily. The rule based approach is able to segment hemorrhage well. The classification method is able to predict outcome which is helpful to provide recommendations to physicians. The methods proposed are all automated and reduces the processing time by eliminating the need for manual intervention.

9.3. Future Work

The future work includes the following items:

- Test the algorithms with high resolution CT images from a larger database in order to segment hemorrhage and perform classification.
- Expand the analysis of spleen segmentation to detect hemorrhage and laceration in abdominal trauma. This involves several steps:
 - Test the proposed spleen segmentation technique on a larger dataset.

- Detection of other solid organs (such as liver and kidneys) i.e. those which are commonly injured during the abdominal trauma.
- Detect the lacerations, active bleeding and passive bleeding of the organs in the region.

Bibliography

Bibliography

- [1] G. Bergen, L. H. Chen, M. Warner, and L. A. Fingerhut. Injury in the United States: 2007 Chartbook. *Hyattsville, MD:National Center for Health Statistics*. 2008.
- [2] M. R. hemmila, *et.al*. Real money: complications and hospital costs in trauma patients. *Surgery*, 144(2):307-16, 2008.
- [3] K. D. Kochanek, J. Xu, S. L. Murphy, A. M. Miniño, and H. Kung. Deaths: Preliminary data for 2009. *National Vital Statistics Reports*, 59(4), 2011.
- [4] R. P. Dutton, L. G. Stansbury, S. Leone, E. Kramer, J. R. Hess, and T. M. Scalea. Trauma mortality in mature trauma systems: are we doing better? An analysis of trauma mortality patterns, 1997-2008. *The Journal of Trauma*, 69(3):620-6, 2010.
- [5] K. Kendall-Tackett. Psychological trauma and physical health: a psychoneuroimmunology approach to etiology of negative health effects and possible interventions. *Psychological Trauma: Theory, Research, Practice and Policy*, 1(1):35-48, 2009.
- [6] J. A. Depalma, P. Fedorka, and L. C. Simko. Quality of life experienced by severely injured trauma survivors. *AACN Clinical Issues*, 14(1):54-63, 2003.
- [7] H. T. Stelfox, B. Bobranska-Artiuch, A. nathens, S. E. Straus. Quality indicators for evaluating trauma care. *Arch. Surg.*, 145(3):286-295, 2010.

- [8] C. G. Macias, and J. J. Sahouria. The appropriate use of CT: quality improvement and clinical decision-making in pediatric emergency medicine. *Pediatric Radiology*, 41(2):498-504, 2011.
- [9] M. Bardenheuer, C. Waydhas, and D. Nast-Kolb. Epidemiology of the severely injured patient: a prospective assessment of preclinical and clinical management. *Unfallchirurg*, 103(5):355-63, 2000.
- [10] T. Geeraerts, *et.al.* Clinical review: initial management of blunt pelvic trauma patients with haemodynamic instability. *Critical Care*, 11(1), 2007.
- [11] R. R. Ivatury, *et.al.* Patient Safety in Trauma: Maximal impact management errors at a level I trauma center. *The journal of Trauma*, 64: 265-272, 2008.
- [12] R. L. Gruen, G. J. Jurkovich, L. K. McIntyre, H. M. Foy, and R. V. Maier. Patterns of errors contributing to trauma mortality: lessons learned from 2594 deaths. *Ann. Surg.*, 244(3): 371-380, 2006.
- [13] K. Kahol, M. Vanikpuram, V. L. Patel, and M. L. Smith. Deviations from protocol in a complex trauma environment: errors or innovations?. *Journal of Biomedical Informatics*, 44: 425-431, 2011.
- [14] M. Fitzgerald, *et. al.* Trauma Resuscitation errors and computer-assisted decision support. *Arch. Of Surgery*, 146(2): 218-225, 2011.
- [15] Laxmisan, F. hakimzada, O. R. Sayan, R. A. Green, J. Zhang, V. L. Patel. The multitasking clinician: decision-making and cognitive demand during and after team handoffs in emergency care. *International journal of Medical Informatics*, 76: 801-811, 2007.

- [16] K. D. stahl, S. E. Brien. Reducing patient errors in trauma care. In: *Cohn S, ed. Acute care Surgery: Evidenced-based practice*. New York, NY: Informa Healthcare USA Inc., 268-77, 2009.
- [17] K. D. Stahl, et.al. Enhancing patient safety in trauma/surgical intensive care unit. *The Journal of Trauma*, 67(3): 430-435, 2009.
- [18] S.Y. Ji, R. Smith, T. Huynh, and K. Najarian. A comparative analysis of multilevel computer-assisted decision making systems for traumatic injuries. *BMC Medical Informatics and Decision Making*, 9(2), 2009.
- [19] W. Yoon, J. K. Kim, Y. Y. jeong, J. J. Seo, J. G. Park, and H. K. Kang. Pelvic arterial hemorrhage in patients with pelvic fractures:detection with contrast-enhanced CT. *RadioGraphics*, 24: 1591-1605, 2004.
- [20] B. M. Evers, H. M. Cryer, F. B. Miller. Pelvic fracture hemorrhage. Priorities in management. *Arch. Surg.* 124(4):422-4, 1989.
- [21] D. J. hak, W. R. Smith, and T. Suzuki. Management of Hemorrhage in life-threatening pelvic fracture. *J Am Acad Orthop Surg*, 17(7):447-457, 2009.
- [22] J. G. Crompton et. al. Racial disparities in motorcycle-related mortality: an analysis of the national trauma data bank. *The American Journal of Surgery*, 200: 191-196, 2010.
- [23] S. Banerjee, M. J. Barry, and J. M. H. Paterson. Paediatric pelvic fractures: 10 years experience in a trauma centre. *Injury*, 40(4): 410-413, 2009.

- [24] D. Verbeek, et. al. Acute management of hemodynamically unstable pelvic trauma patients: time for a change? Multicenter review of recent practice. *World J Surg*, 32: 1874-1882, 2008.
- [25] B. Durkin, H. C. Sagi, R. Durham, and L. Flint. Contemporary management of pelvic fractures. *The American journal of Surgery*, 192(2):211-223, 2006.
- [26] K. Eckroth-Bernard, and J. W. davis. Management of pelvic fractures. *Current opinion in Critical Care*, 16(6): 582-586, 2010.
- [27] J. A. requarth, and P. R. Miller. Aberrant Obturator Artery is a common arterial variant that may be a source of unidentified hemorrhage in pelvic fracture patients. *The Journal of Trauma*, 70(2): 366-372, 2011.
- [28] S. Asadollahi, et. al. Management guideline in haemodynamically unstable patients with pelvic fractures: outcomes and challenges. *Emergency Medicine Australasia*, 22:556-564, 201.
- [29] P. A. O'Neill, J. Riina, S. Sclafani, and P. Tornetta. Angiographic findings in pelvic fractures. *Clinical Orthopaedics & Related Research*, 329: 60-67, 1996.
- [30] J. Uyeda, S. W. Anderson, J. Kertesz, and J. A. Soto. Pelvic CT angiography: application to blunt trauma. *Emerg Radiol*, 17: 131-137, 2010.
- [31] Furlan, S. Fakhran, and M. P. Federle. Spontaneous abdominal hemorrhage: causes, CT findings, and clinical implications. *American Journal of Roentgenology*, 193(4): 1077-1087, 2009.
- [32] S. Vasilache. Image segmentation and analysis for automated classification of traumatic pelvic injuries. *Ph.DThesis*, 2010.

- [33] D. L. Pham, C. Xu, and J. L. Prince. Current Methods in Medical Image Segmentation. *Annu. Rev. Biomed. Eng.*,315-337, 2000.
- [34] N. Pérez, J. Valdés, M. Guevara, and A. Silva. *Advances in Computational Vision and Medical ImageProcessing*, Springer, Netherlands, 2009.
- [35] Z. Ma, J. M. Tavares, R. N. Jorge, and T. Mascarenhas. A review of algorithms for medical image segmentation and their applications to the female pelvic cavity. *Comput Methods Biomech Biomed Engin.*,235-46, 2010.
- [36] N. Otsu. A Threshold selection method from gray-level histograms. *IEEE Trans. On Systems, Man, and Cybernetics*, 9(1): 62-66, 1979.
- [37] M. Sezgin. Survey over image thresholding techniques and quantitative performance evaluation. *Journal of Electronic Imaging*, 2004.
- [38] S. Wang, F. Chung, and F. Xiong. A novel image thresholding method based on parzen window estimate. *Pattern Recognition*, 41: 117-129, 2008.
- [39] M. Maitra, and A. Chatterjee. A hybrid cooperative comprehensive learning based PSO algorithm for image segmentation using multilevel thresholding. *Expert Systems with Applications*, 34(2): 1341-1350, 2008.
- [40] K. Hammouche, M. Diaf, and P. Siarry. A multilevel automatic thresholding method based on genetic algorithm for fast image segmentation. *Computer Vision and Image Understanding*, 109: 163-175, 2008.
- [41] D. Y. Kim, and J. W. Park. Connectivity-based local adaptive thresholding for carotid artery segmentation using MRA images. *Image and Vision Computing*, 23(14):1277-1287, 2005.

- [42] T. Heimann, et al. Comparison and evaluation of methods for liver segmentation from CT datasets. *IEEE Trans. On Medical Imaging*, 28(8): 1251-1265, 2009.
- [43] R. Adams, and L. Bischof. Seeded region growing. *IEEE Trans. On Pattern Analysis and Machine Intelligence*, 16(6): 641-647, 1994.
- [44] S. A. Hojjatoleslami, and J. Kittler. Region growing: A new approach. *IEEE Trans. On Image Processing*, 7(7):1079-1084, 1998.
- [45] J. Dehmeshki, H. Amin, M. Valdivieso, and X. Ye. Segmentation of pulmonary nodules in thoracic CT scans: A region growing approach. *IEEE Trans. Medical Imaging*, 27(4):467-480, 2008.
- [46] R. B. Dubey, M. Hanmandlu, S. K. Gupta, and S. K. Gupta. Region growing for MRI brain tumor volume analysis. *Indian J Sci. Technol.*, 2(9): 26-31, 2009.
- [47] Z. Peter, V. Bousson, C. Bergot, and F. Peyrin. A constrained region growing approach based on watershed for the segmentation of low contrast structures in bone micro-CT images. *Pattern Recognition*, 41(7), 2008.
- [48] N. A. M. Isa, S. A. Salamah, and U. K. Ngah. Adaptive fuzzy moving K-Means clustering algorithm for image segmentation. *IEEE Trans. Consumer Electronics*, 55(4): 2145-53, 2009.
- [49] M. Filippone, F. Camastra, F. Masulli, and S. Rovetta. A survey of kernel and spectral methods for clustering. *J Pattern Recognition*, 41: 176-190, 2008.
- [50] T.H. Lee, R. Komiya, and M.F.A. Fauzi. Segmentation of CT brain images using k-means and EM clustering. In *Conference on computer Graphics, Imaging and Visualization*, 2008.

- [51] S. Z. Li. Markov random field modeling in computer vision. Springer-Verlag, 264, 1995.
- [52] Y. Zhang, M. Brady, and S. Smith. Segmentation of brain MR images through a hidden Markov random field model and the expectation-maximization algorithm. *IEEE Trans. Medical Imaging*, 20(1):45-57, 2002.
- [53] Sarkar, M.K. Biswas, and K. M. S. Sharma. A simple unsupervised MRF model based image segmentation approach. *IEEE Transactions on Image Processing*, 9, 2000.
- [54] I.Y. Kim and H.S. Yang. A systematic way for region based image segmentation based on Markov random field model. *Pattern Recognition Letters*, 15, 1994.
- [55] L. Lin, L. Zhu, F. Yang, and T. Jiang. A novel pixon-representation for image segmentation based on Markov random field. *Image and Vision Computing*, 26(11):1507-1514, 2008.
- [56] Z. Dokur. A unified framework for image compression and segmentation by using an incremental neural network. *Expert Systems with Applications*, 34: 611-619, 2008.
- [57] G. Ertas, H. Ö. Gülçür, O. Osman, O. N. Uçan, M. Tunaci, and M. Dursun. Breast MR segmentation and lesion detection with cellular neural networks and 3D template matching. *Computers in Biology and Medicine*, 38(1): 116-126, 2008.
- [58] D. Kainmueller, H. Lamecker, S. Zachow, and H. Hege. Coupling deformable models for multi-object segmentation. *Lecture Notes in Computer Science*, 5104: 69-78, 2008.

- [59] T. McInerney, and D. Terzopoulos. Deformable models in medical image analysis: a survey. *Medical Image Analysis*, 1(2): 91-108, 1996.
- [60] S.S.C. Burnett, G. Strakschall, C.W. Stevens, and Z. Liao. A deformable-model approach to semi-automatic segmentation of CT images demonstrated by application to the spinal canal. *Medical Physics*, 31(2), 2004.
- [61] M. Kass, A. Witkin, and D. Terzopoulos. Snakes: Active contour models. *International Journal of Computer Vision*, 1988.
- [62] J.V. Stough, R.E. Broadhurst, S.M. Pizer, and E.L. Chaney. Clustering on local appearance for deformable model segmentation. In *Symposium on Biomedical Imaging: From Nano to Macro*, 2007.
- [63] J.V. Stough, R.E. Broadhurst, S.M. Pizer, and E.L. Chaney. Regional appearance in deformable model segmentation. In *Information Processing in Medical Imaging*. Springer Berlin / Heidelberg, 2007.
- [64] L. He et. al. A comparative study of deformable contour methods on medical image segmentation. *Image and Vision Computing*, 26(2): 141-163, 2008.
- [65] G. Chung, and L. A. Vese. Image segmentation using a multilayer level-set approach. *Comput Visual Sci*, 12: 267-285, 2009.
- [66] C. li, R. Huang, Z. Ding, J. Gatenby, D. Metaxas, and J. Gore. A variational level set approach to segmentation and bias correction of images with intensity inhomogeneity, Springer-Verlag Berlin Heidelberg, 1083-1091, 2008.
- [67] H. Zhou, Y. Yuan, F. Lin, and T. Liu. Level set image segmentation with Bayesian analysis. *Neurocomputing*, 71: 1994-2000, 2008.

- [68] C. Li, R. Huang, Z. Ding, J. C. Gatenby, D. N. Metaxas, and J. C. Gore. A level set method for image segmentation in the presence of intensity inhomogeneities with application to MRI. *IEEE Trans. Image Processing*, 20(7): 2007-2016, 2011.
- [69] X. Han et al. Atlas-based auto-segmentation of head and neck CT images. *Lecture Notes in Computer Science*, 5242: 434-441, 2008.
- [70] P. Y. Bondiau et al. Atlas-based automatic segmentation of MR images: validation study on the brainstem in radiotherapy context. *Int J Radiat Oncol Biol Phys*, 61(1): 289-298, 2005.
- [71] L. Zhang, E. A. Hoffman, and J. M. Reinhardt. Atlas-driven lung lobe segmentation in volumetric X-ray CT images. *IEEE Trans. Medical Imaging*, 25(1):1-16, 2005.
- [72] I. Isgum, A. Rutten, M. Prokop, M. A. Viergever, and B. V. Ginneken. Multi-atlas-based segmentation with local decision fusion – application to cardiac and aortic segmentation in CT scans. *IEEE Trans. Medical Imaging*, 28(7):1000-1010, 2009.
- [73] M. Mancas, and B. Gosselin. Towards an automatic tumor segmentation using iterative watersheds. In *Society of Photo-Optical Instrumentation Engineers Conference Series, SPIE*, 2004.
- [74] R. Shojaii, J. Alirezaie, and P. Babyn. Automatic lung segmentation in CT images using watershed transform. In *IEEE International Conference on Image Processing*, 2005.
- [75] M. Straka, A. LaCruz, A. Kochl, M. Sramek, D. Fleischmann, and E. Groller. 3d watershed transform combined with a probabilistic atlas for medical image segmentation. In *Proceedings of MIT 2003*, 2003.

- [76] H. Tek and H.C. Aras. Local watershed operators for image segmentation. In *Medical Image Computing and Computer-Assisted Intervention MICCAI 2004*. Springer Berlin / Heidelberg, 2004.
- [77] M. Frucci and G. Sanniti di Baja. Oversegmentation reduction in watershed-based grey-level image segmentation. *International Journal of Signal and Imaging Systems Engineering*, 1, 2008.
- [78] X. Xie, X. Ma, X. Yu, and R. Du. Liver image segmentation using improved watershed method. *Applied Mechanics and Materials*, 58-60: 1311-1316, 2011.
- [79] S. Vasilache, W. Chen, K. Ward, and K. Najarian. Heirarchical object recognition in pelvic CT images. *31st Annu. Conf. IEEE EMBS*, 3533 – 3536, 2009.
- [80] S. Vasilache, K. Ward, C. Cockrell, J. Ha, and K. Najarian. Unified wavelet and gaussian filtering for segmentation of CT images; application in segmentation of bone in pelvic CT images. *BMC Med. Informatics and Decision Making*, 9(1):S8, 2009.
- [81] H. Gray. Anatomy of the human body. *The American Journal of Medical Sciences*, 157(5), 1919.
- [82] clinicaldepartments.musc.edu/radiology/powerpoint/pelvic.ppt
- [83] P. Davuluri, J. Wu, Y. Tang, C. Cockrell, K. Ward, K. Najarian, and R. Hargraves. Hemorrhage detection and segmentation in traumatic pelvic injuries. *Computational and Mathematical Methods in Medicine*, Article ID 898430, 2012.

- [84] J.P.W. Pluim, J.B.A. Maintz, and M.A. Viergever. Mutual-information-based registration of medical images: a survey. *IEEE Transactions on Medical Imaging*, 22(8): 986-1004, 2003.
- [85] T. Huang, V. Kecman, and I. Kopriva. Kernel based algorithms for mining huge data sets: supervised, semi-supervised, and unsupervised learning (Studies in Computational Intelligence), Springer-Verlag New York, Inc., 2006.
- [86] G. Wang, Z. Wang, W. Chen, and J. Zhuang. Classification of surface EMG signals using optimal wavelet packet method based on Davies–Bouldin criterion. *Med. Biol. Eng. Comput.*, 44: 865–872, 2006.
- [87] L. Yu, and H. Liu. Feature selection for high-dimensional data: a fast correlation-based filter solution. *Proc. 20th Int’l Conf. Machine Learning*, 856-863, 2003.
- [88] T. Hastie, R. Tibshirani, and J. Friedman. Boosting and additive trees. *The Elements of Statistical Learning*, 337-387, 2009.
- [89] N. Landwehr, M. Hall, and E. Frank. Logistic model trees. *Machine Learning*, 59:161-205, 2005.
- [90] G. Costa, S. M. Tierno, F. Tomassini, L. Venturini, B. Frezza, G. Cancrini, and F. Stella. The epidemiology and clinical evaluation of abdominal trauma. An analysis of a multidisciplinary trauma registry. *Ann Ital Chir.*, 81(2): 95-102, 2010.
- [91] A. Brooks, and J. A. D. Simpson. Blunt and penetrating abdominal trauma. *Surgery*, 27(6): 266-271, 2009.

- [92] M. A. Gad, A. Saber, S. Farrag, M. E. Shams, and G. M. Ellabban. Incidence, patterns, and factors predicting mortality of abdominal injuries in trauma patients. *N Am J Med Sci.*, 4(3):129-134, 2012.
- [93] M. Valentino, C. Serra, G. Zironi, C. De Luca, P. Pavlica, and L. Barozzi. Blunt abdominal trauma: emergency contrast-enhanced sonography for detection of solid organ injuries. *AJR Am J Roentgenol.*, 186(5): 1361-7, 2006.
- [94] W. L. Biffl, and E. E. Moore. Management guidelines for penetrating abdominal trauma. *Current Opinion in Critical Care*, 16(6): 609-617, 2010.